DETECTING ANNUAL SPRUCE BUDWORM DEFOLIATION USING DIGITAL HEMISPHERICAL AND EO-1 HYPERION HYPERSPECTRAL IMAGERY

by

Shawn Donovan

Bachelor of Science in Forestry, University of New Brunswick, 2015

A Thesis Submitted in Partial Fulfillment
of the Requirements for the Degree of

Master of Science in Forestry

in the Graduate Academic Unit of Forestry and Environmental Management

Supervisor: David A. MacLean, PhD, Forestry and Environmental Management

Examining Board: Yun Zhang, PhD, Geodesy and Geomatics Engineering
Anthony Taylor, PhD, Canadian Forest Service

This thesis is accepted by the
Dean of Graduate Studies

THE UNIVERSITY OF NEW BRUNSWICK

May, 2020

Abstract

Estimating defoliation damage during spruce budworm (SBW; *Choristoneura fumiferana* Clem.) outbreaks is important for implementing effective forest protection strategies, yet methods can be inconsistent. This thesis evaluates digital hemispherical imagery and Earth Observing-1 Hyperion hyperspectral remote sensing data for quantifying annual SBW defoliation, validated using accurate plot-level defoliation measurements from 75 sample plots in Québec, Canada. Hemispherical canopy gap fraction change from May-October, % balsam fir (*Abies balsamea* (L.) Mill.) basal area, and bioinsecticide spraying were important explanatory variables for modelling percent annual canopy defoliation, with root mean square errors ranging 14–24%. Semi-supervised classification of annual defoliation using the top five hyperspectral vegetation indices resulted in overall accuracies ranging 91–93%. Light (≤30%), moderate (30–70%), and severe (≥70%) defoliation classification accuracy ranged from 86–90%, 93–94%, and 92–96%, respectively. This thesis describes two viable methods that can complement current defoliation surveys in forest protection against SBW.

Acknowledgements

I would like to thank my supervisor, Dr. David A. MacLean for guiding me through the research process. Also, I am appreciative to my committee members Dr. John Kershaw, Dr. Mike Lavigne, and Dr. Yun Zhang for their input and recommendations improving the overall quality of the thesis. Thanks to data providers which include the Québec Ministère des Forêts de la Faune et des Parcs and the Société de Protection des Forêts contre les Insectes et Maladies for providing aerial orthophotos and spruce budworm defoliation survey data. Also, special thanks to the Gretta Goodine (Canadian Forest Service, Atlantic Forestry Centre) who assisted with hemispherical image collection and analysis and to all fellow students Maggie Brewer, Jessica Cormier, Olivia Doran, Matt Hill, Sean Lamb, Rebecca Landry, and Bo Zhang who assisted in collecting sample plot defoliation and inventory data. I greatly appreciate all the support and encouragement received from my parents - Audrey and Kordey and family members and friends. This research was funded by the AWARE (Assessment of Wood Attributes using Remote sEnsing) Natural Sciences and Engineering Research Council of Canada Collaborative Research and Development project led by Dr. Nicholas Coops at the University of British Columbia.

Table of Contents

List of Tables

List of Figures

CHAPTER 1: GENERAL INTRODUCTION

1.1. Problem Statement

Spruce budworm (SBW; *Choristoneura fumiferana* (Clem.), Lepidoptera: Tortricidae) outbreaks are a major natural disturbance occurring throughout northeastern North American forests. Outbreaks date back centuries (Boulanger et al., 2012), and periodically cycle approximately every 35 years (Royama, 1984) when SBW population densities increase several orders of magnitude. SBW severely defoliate hosts balsam fir (*Abies balsamea* (L.) Mill.) and spruce (*Picea spp.*), causing reduced tree growth and increased mortality (MacLean and Ostaff, 1989; Pothier et al., 2012). Mortality of vulnerable mature balsam fir stands has averaged 85% (MacLean, 1980). Major forest defoliation during the 1910s, 1940s, and 1970s outbreaks peaked at 11, 25, and 57 million hectares (ha), respectively (Kettela, 1983). Such large-scale outbreaks can greatly impact forest ecological processes and structure such as carbon cycling and species and age-class distributions (Gray and MacKinnon, 2006). The economic impacts to forest resources for any one jurisdiction during an uncontrolled outbreak can amount to billions of dollars in timber losses. Spruce-fir forests are abundant, representing 59% of the 347,600,000 ha of forests in Canada (Canadian National Forest Inventory, 2013). Therefore, collecting accurate defoliation data is important for monitoring, estimating impacts, and informing forest protection strategies.

Forest protection strategies aimed at minimizing damage by SBW need to be cost-effective, requiring spatial and temporal planning before implementation. The SBW Decision Support System (SBW DSS; MacLean et al. 2001) enables quantitative spatial evaluation of SBW control strategy trade-offs (e.g., bioinsecticide spraying costs versus

timber yields) by forecasting defoliation, SBW populations, and subsequent forest growth and timber yields during an outbreak (MacLean and Porter, 1994; MacLean et al., 2000). The SBW DSS requires accurate, up-to-date spatial inputs of tree inventory information, defoliation-based growth and timber supply models and above all, sampled SBW population and defoliation extent and severity data to determine impacts to spruce-fir forests (MacLean et al., 2000, 2001).

Quantifying the extent and severity of SBW defoliation relies upon provincial governments completing annual aerial surveys and ground sampling, which provide information on defoliation level and evaluation of bioinsecticide spraying for reducing SBW populations (MacLean and MacKinnon, 1998). Currently, aerial surveys of defoliation are operationally the only option for covering large forested areas, and ocular whole-tree or branch sampling rating defoliation on individual shoots (termed shoot-count or Fettes method) are preferred for assessing single trees or stands (Fettes 1950; MacLean and Lidstone 1982; MacLean and MacKinnon 1998). Such defoliation assessment methods can either be accurate yet resource-demanding (e.g., branch sampling) or less precise and expeditious (e.g., ocular and aerial surveys), influencing the selection of SBW control strategies (MacLean and Lidstone, 1982; Zhao et al., 2014).

Satellite remote sensing data can offer additional data and improvements in estimating SBW defoliation, similar to aerial surveys. Remote sensing is defined as the collection and interpretation of electromagnetic energy reflected or emitted from objects (Cielsa, 2000). It can characterize forests across a wide spectral range, allowing the separation of healthy and unhealthy vegetation not possible by human observations (Rullan-Silva et al., 2013). For example, hyperspectral sensors consisting of numerous

narrow wavelength bands can measure subtle spectral changes related to biophysical vegetation characteristics (e.g., chlorophyll content) that are affected by defoliation that would be obscured by broadband multispectral sensors (Hall et al., 2016; Oumar et al., 2013). Also, hemispherical imagery is a potential ground-based alternative to ocular or branch sampling methods as images can accurately quantify canopy structure metrics (e.g., leaf area index (LAI); Chianucci and Cutini 2012), which may be correlated to foliage loss due to defoliation. Such remote sensing data for detecting annual SBW defoliation have not been extensively studied since the start of the most recent SBW outbreak in Québec, Canada and is the focus of this dissertation.

1.2. Background

1.2.1. Spruce budworm overview

SBW populations tend to oscillate in synchrony across large areas influenced by density-dependent (e.g., parasitoid-based mortality) and density-independent (e.g., Moran's theory infers how weather can synchronize the rise of independent SBW populations) factors that increase SBW survival and life cycle completion (Nenzén et al., 2018; Royama, 1984). SBW larval feeding coincides with host-tree phenology, specifically the bud/foliage growth of balsam fir and white spruce and, to a lesser extent, black and red spruce (Nealis and Régnière, 2004; Pureswaran et al., 2015). SBW has one generation per year, and eggs are laid in mid-July to early August on host foliage (Royama et al., 2017). Ten days later, the first-instar larvae (L1) emerge and seek nearby over-wintering sites (e.g., under bark, behind lichen), spin silken hibernacula, and molt into the second instar (L2), where they enter diapause and overwinter (Royama et al.,

2017). In early May, L2 larvae emerge and may disperse again seeking feeding sites near 1–2 year-old foliage, or in seed and pollen cones if present (Royama, 1984). From early June to early July, larvae feed on current-year foliage, molt from L3 to L6, and pupate in mid-July (Royama et al., 2005). Approximately 8–12 days later, adult moths emerge and reproduce, completing their life cycle by laying the next generation of eggs (Royama, 1984).

Understanding SBW host-tree susceptibility and vulnerability can improve the development of effective SBW control strategies and forecasting stand responses. Susceptibility is defined as the probability of defoliation severity among hosts and vulnerability is defined as the probability of relative growth declines and the amount of mortality (MacLean, 1980; MacLean and MacKinnon, 1997). SBW defoliation differs among host species, with balsam fir the most defoliated followed by white spruce (*Picea glauca* [Moench] Voss), red spruce (*Picea rubra* Sarg.), black spruce (*Picea mariana* [Mill.] B.S.P.) having estimates of 72, 41, and 28% as much defoliation as balsam fir, respectively (Hennigar et al., 2008). Furthermore, stands with increasing non-host species compositions have been shown to have less defoliation compared to host-dominated softwood stands (Su et al., 1996; Zhang et al., 2018). During past outbreaks, observed mortality reached 85% and 43% for mature and immature balsam fir stands, whereas mature and immature spruce stands experienced less mortality at 36% and 13%, respectively (MacLean, 1980). Other factors influencing defoliation and subsequent growth declines and mortality relate to stand cohort and age structure (Bergeron et al., 1995; MacLean, 1980) and site richness and drainage (MacLean and MacKinnon, 1997).

SBW-caused tree mortality in Québec was estimated at 238 million m^3 during the 1970s-1980s outbreak with similar additional losses due to reduced tree growth (Coulombe Commission (Commission d'étude sur la gestion de la forêt publique québécoise) 2004), resulting in an estimated $12.5 billion in commercial value losses to the forest economy (Lévesque et al., 2010). New Brunswick, which encompasses a combined 6.0 million (ha) of Crown, industrial, and private forests, also endured timber losses with defoliation peaking at 3.5 and 2.2 million ha in 1975 and 1983, respectively (Chang et al., 2012).

Scenarios of SBW outbreaks for New Brunswick's 2.8 million ha of Crown forest projected cumulative timber supply reductions of 29–43 million m^3 from 2017–2067, which would reduce total economic output by $25–35 billion (Liu et al., 2019). Scenarios testing bioinsecticide spraying on 20% of the area were projected to reduce losses by $0.5–4.0 billion depending on the outbreak scenario (Liu et al., 2019). Hennigar et al. (2013) estimated timber harvest reductions of 18–25% by 2052 during moderate and severe outbreaks and demonstrated that 30–50% of these reductions could be minimized through optimized spraying programs. Chang et al. (2012) also projected that uncontrolled moderate and severe outbreaks from 2012–2041 would reduce the forest economy present-value by $3.3 and $4.7 billion, respectively.

The current SBW outbreak in Québec has increased annually since 2004, and the defoliated area is now estimated at 9.6 million ha as of 2019 provincial aerial surveys (QMFFP 2019). Reliable and accurate spatial defoliation estimates are in high demand for ongoing projects like the Early Intervention Strategy (EIS) in New Brunswick, which

aims to suppress rising SBW populations by spraying bioinsecticides and has shown early signs of success (MacLean et al., 2019).

1.2.2. Spruce budworm management and methods for estimating defoliation

Strategies to manage forests to reduce damage during SBW outbreaks can involve pre-outbreak silviculture treatments (e.g., tree thinning) to reduce balsam fir content, salvage harvesting already defoliated stands within 3–5 years post damage, and aerial application of bioinsecticides to reduce SBW populations and keep trees alive until outbreak conditions subside (MacLean et al., 2000, 2001). Bioinsecticides in current use are *Bacillus thuringiensis* var. Kurstaki (*Btk*) or tebufenozide (MacLean et al., 2019). After detection of at least two years of moderate-severe defoliation, annual applications of Btk every two years for balsam fir and white spruce dominated stands and every three years for black spruce stands provides acceptable protection maintaining residual photosynthetic capacity above 39% (Fuentealba et al., 2019). However, selecting stands to salvage harvest or conduct aerial spraying currently relies on coarse resolution aerial survey methods for delineating defoliation.

Timing for conducting aerial surveys consists of a relatively short 2–3 week period during which 87% of defoliation is caused by the 6^{th} larval-instar (Miller, 1977), resulting in partially damaged and dead foliage that turns reddish-brown in color (MacLean and MacKinnon, 1996; Rahimzadeh-Bajgiran et al., 2018). Fixed-wing aircraft fly at altitudes of 150–300 m and systematically cover the potentially defoliated area by flight lines at 2–5 km spacing and observers categorize groups of stands by the degree of foliage discoloration into broad categories of light (< 30%), moderate (30–70%), and severe (>

70%) defoliation classes (MacLean and MacKinnon, 1996). Aerial surveys from 1984–1993 in New Brunswick showed classification accuracies of 82% based on three defoliation classes; however, accuracy declined to 56% using four classes (including nil as 0-10% defoliation) because discriminating lower levels is visually difficult and severe defoliation is often scattered and underestimated (MacLean and MacKinnon, 1996). Although aerial defoliation surveys can provide reasonable accuracy, they are subject to errors due to variability among observers, incorrect georeferencing, and the influence of poor weather conditions during flights (Taylor and MacLean, 2008; Zhao et al., 2014).

Stand- and tree-level ocular and branch sampling methods for estimating defoliation are often used for research plots or for verifying aerial survey data (MacLean and Lidstone, 1982). Both methods can be used to quantify current defoliation (on the most recent foliage age-class, provides the current status of an outbreak) or cumulative defoliation (assessment of all foliage age-classes; important for estimating tree growth reduction and mortality rates) (MacLean et al., 1996). Ocular defoliation estimates require trained observers with binoculars rating defoliation of single trees by percentage defoliation or class-based systems (MacLean and MacKinnon, 1998). Branch sampling (shoot-count or Fettes method - Fettes 1950) typically involves sampling one mid-crown branch per tree and rating a minimum of 25 random shoots per foliage age-class for defoliation (Fettes 1950; MacLean and MacKinnon 1998 provided sample size-accuracy relationships for estimating defoliation). MacLean and Lidstone (1982) assessed the accuracy of branch versus ocular methods and concluded that branch sampling achieved a relative accuracy of ±7%, whereas the best ocular accuracy was ±12%. Branch sampling

is resource-demanding, and ocular estimates often overestimate at lower defoliation levels (MacLean and Lidstone, 1982).

1.2.3. Quantifying forest canopy changes caused by SBW defoliation using digital hemispherical imagery

Hemispherical images of forests were first studied to describe the light conditions of the understory (Evan and Coombe, 1959). Since the decline in the use of film photography, digital camera technology and image progressing methods have renewed interest in quantifying forest structures (Chianucci and Cutini, 2012). Hemispherical images use the Beer-Lambert law of energy absorbance and transmittance through objects to quantify gap fraction (proportion of sky pixels to total image pixels) at multiple zenith angles, which can be used to estimate effective leaf area index (eLAI), canopy openness, and foliage angle distributions (Chianucci and Cutini, 2012). Such forest structure metrics are important for understanding forest ecosystems and changes in the biological and physical processes of vegetation communities (Chen et al., 1997).

Hemispherical images have been shown to be effective for detecting seasonal LAI changes in deciduous forests located in China, with the key factors woody material, foliage clumping, and incorrect image exposure explaining 72% of the variation between direct and image-derived LAI estimates (Liu et al., 2015). Kubo et al. (2012) demonstrated that Normalized Difference Vegetation Index and sky visibility changes from Near-Infrared and visible spectrum hemispherical images could be used to detect larch sawfly (*Pristiphora erichsonii* Hartig) defoliation. LAI changes from hemispherical images were strongly correlated ($R^2 = 0.93$) with inverse gap fraction values measured by

airborne laser scanning during a pine sawfly (*Neodiprion sertifer* Geoffrey) outbreak (Hanssen and Solberg, 2007). The above studies indicating that hemispherical imagery can track forest canopy changes suggests that detecting SBW defoliation-induced canopy changes with images may be a viable alternative to ocular and branch estimates for monitoring SBW defoliation of trees and plots.

1.2.4. Assessing spruce budworm defoliation using satellite hyperspectral remote sensing data

Since the 1970s-1980s SBW outbreak, several new satellite-based sensors with improved spatial, temporal, and spectral capabilities have become available to assist or replace aerial surveys for estimating forest-level SBW defoliation. The Worldview-3 high spatial resolution of 0.31m pixel size enables within-stand and tree-level detection (Lausch et al., 2016); Sentinel-2 twin satellites allow global coverage and near-continuous temporal images (5-day imaging period) improving monitoring (Claverie et al., 2018); and hyperspectral sensors such as Earth Observing-1 (EO-1) Hyperion have numerous (220) narrow bands with continuous 10 nanometer (nm) bandwidths from 400–2500 nm collecting highly sensitive reflectance data (Deák et al., 2017). Hall et al. (2016) reviewed remote sensing of forest pest damage in Canada and concluded that change detection using multiple images has become more common and performs better than single image analysis. In relation to the limited SBW defoliation detection period, change detection especially using hyperspectral sensors with increased spectral sensitivity can extend the detection period offering more imaging opportunities improving monitoring capabilities. However, images should still be acquired near the peak SBW defoliation

detection period maximizing the possible spectral change before and after defoliation and avoiding non-target spectral influences that lead to Type I classification errors.

Past remote sensing studies of SBW defoliation mainly focused on detecting cumulative defoliation rather than current-year defoliation, which is vital for updating SBW control strategies. Franklin et al. (2008) tested multi-temporal Landsat-5 TM (Thematic Mapper) and single date SPOT-4 HRVIR (High Resolution Visible and Infrared) imagery and found correlations ranging from r = 0.81–0.88 between three cumulative defoliation classes and vegetation indices (VIs). Tree-level cumulative defoliation was detected using aerial MEIS (Multispectral Electro-optical Imaging Scanner) imagery, achieving accuracies of 51, 53, 60, 80, and 92% for 8, 7, 6, 5, and 4 defoliation class designs, respectively (Leckie et al., 1992). Digital aerial photogrammetric data was used to assess percent cumulative defoliation, with spectral metrics explaining 79% of the variation (Goodbody et al., 2018). Rahimzadeh-Bajgiran et al. (2018) used Landsat-5 TM imagery to estimate annual defoliation calibrated with aerial survey data and achieved accuracies of 77, 60, 52, and 77% for nil, light, moderate, and severe defoliation classes, respectively.

Monitoring forest insect infestations using hyperspectral imagery has the benefits of detecting earlier and lower levels of damage using enhanced spectral information (Pontius et al., 2008). Pontius et al. (2005) used chlorophyll and water sensitive VIs from AVIRIS (Airborne Visible/Infrared Imaging Spectrometer) hyperspectral aerial imagery to detect hemlock (*Tsuga canadensis* L. Carr) decline by hemlock woolly adelgid (*Adelges tsugae* Annand) in 10 classes with 85% accuracy. EO-1 Hyperion imagery calculating three VIs predicted bronze bug (*Thaumastocoris peregrinus* Carpintero and

Dellapé) damage with an $R^2 = 0.74$ (Oumar et al., 2013), and VIs related to moisture content calculated from EO-1 Hyperion imagery were significantly related ($R^2 = 0.51$, $p = 0.00001$) to mountain pine beetle (*Dendroctonus ponderosae* Hopkins) damage (White et al., 2007). Huang (2015) is currently the only study that detected annual SBW defoliation and found a 15% improvement in classification accuracy for EO-1 Hyperion hyperspectral imagery compared to multispectral imagery. Change detection of narrow-band VIs defining light and severe defoliation classes resulted in overall accuracies of 63–78%, when using aerial survey data for training and validation (Huang, 2015). Although encouraging, accurate ground truth data such as plot-measured defoliation are needed for reliable verification (Rahimzadeh-Bajgiran et al., 2018).

1.3. Research Objectives

The overall objectives of this thesis were to: 1) test hemispherical image gap fraction changes and stand attributes for quantifying within-stand annual SBW defoliation as a viable alternative to ocular and branch defoliation methods; and 2) evaluate change detection of narrow-band VIs using hyperspectral imagery (EO-1 Hyperion) for assisting or improving upon aerial surveys for forest-level mapping of annual SBW defoliation.

Specific objectives of the hemispherical study (Chapter 2) were to:

1) construct models using metrics derived from hemispherical images and stand attributes to explain variations in defoliation by ocular and branch sampling;
2) compare logistic Generalized Linear Model (parametric) and RF (non-parametric) methods to create these models; and

3) examine whether models apply to both insecticide sprayed or unsprayed plots.

Specific objectives of the hyperspectral study (Chapter 3) were to:

1) use RF variable importance metrics to evaluate change detection of 14 narrow-band VIs calculated from hyperspectral imagery to detect three classes of annual SBW defoliation;
2) assess defoliation classification accuracies of semi-supervised machine learning RF and SVM classifiers validated using branch defoliation measured in 68 field plots; and
3) apply the best performing RF and SVM classifiers to map three defoliation classes for 14,000 ha and compare results with aerial survey maps

1.4. Study Design and Thesis Structure

This thesis consists of two different studies using two remote sensing datasets, both designed to quantify forest canopy changes from annual SBW defoliation. Chapter 2 assesses canopy gap fraction changes collected by a digital hemispherical camera during 2015 and 2016 SBW defoliation events. Images before, during, and after defoliation were acquired from 75 field plots located in central Gaspé peninsula, Québec, where a recent SBW outbreak began in 2012 (QMFFP 2019). Accurate tree-level ocular and branch defoliation measurements and extensive tree, stand, and bioinsecticide spraying data were collected from the field plots. Numerous hemispherical image gap fraction change and stand metrics were evaluated for predicting annual canopy defoliation using Generalized Linear Model and Random Forest (RF) statistical methods.

Chapter 3 used satellite hyperspectral (EO-1 Hyperion) images collected before and after peak defoliation and validated with accurate branch defoliation measurements from

68 field plots for classifying 2016 annual SBW defoliation over 14,000 ha of forest. The relative change detection of 14 VIs from vegetation greenness, canopy water content, and light use efficiency categories were compared to defoliation using RF variable importance analysis. The most sensitive VIs were incorporated into semi-supervised RF and Support Vector Machine (SVM) classifiers (Maxwell et al., 2018) for classifying three light (< 30%), moderate (30-70%) and severe (> 70%) defoliation classes.

Finally, this thesis is presented in four chapters. Following this introduction, Chapter 2, *Quantification of forest canopy changes caused by spruce budworm defoliation using digital hemispherical imagery*, used forest canopy changes measured by hemispherical images along with stand attributes as a method to predict within-stand annual SBW defoliation. Chapter 3, *Potential of satellite hyperspectral imagery for detecting annual spruce budworm defoliation*, examined narrow-band vegetation indices from satellite hyperspectral (EO-1 Hyperion) imagery for classifying three annual defoliation classes for 14,000 ha of forest located in the Gaspé Peninsula, Québec. Chapter 4 summarizes the main results and conclusions from Chapters 2 and 3, discusses the main applications in the context of SBW defoliation monitoring and management. Also, we review possible Chapter 2 and 3 limitations and suggest possible improvements and follow-up research opportunities.

1.5. References

Bergeron, Y., Leduc, A., Morin, H., Joyal, C., 1995. Balsam fir mortality following the last spruce budworm outbreak in northwestern Quebec. Can. J. For. Res. 25, 1375–1384.

Boulanger, Y., Arseneault, D., Morin, H., Jardon, Y., Bertrand, P., Dagneau, C., 2012.

Dendrochronological reconstruction of spruce budworm (*Choristoneura fumiferana*) outbreaks in southern Québec for the last 400 years. Can. J. For. Res. 42, 1264–1276.
Canadian National Forest Inventory, 2013. Area of forest land by species group and age class in Canada. https://nfi.nfis.org/resources/general/summaries/en/html/CA3_T14_LSAGE20_AREA_en.html (accessed 1.19.19).
Chang, W-Y., Lantz, V.A., Hennigar, C.R., MacLean, D.A., 2012. Economic impacts of forest pests: a case study of spruce budworm outbreaks and control in New Brunswick, Canada. Can. J. For. Res. 42, 490–505.
Chen, J.M., Rich, P.M., Gower, S.T., Norman, J.M., Plummer, S., 1997. Leaf area index of boreal forests: theory, techniques, and measurements. J. Geophys. Res. 102, 29429–29443.
Chianucci, F., Cutini, A., 2012. Digital hemispherical photography for estimating forest canopy properties: current controversies and opportunities. iForest - Biogeosciences For. 5, 290–295.
Cielsa, W.M., 2000. Remote sensing in forest health protection. United States Department of Agriculture Forest Service, Forest Health Technology Enterprise Team, Salt Lake City, Utah. FHTET Report No.00–03.
Claverie, M., Ju, J., Masek, J.G., Dungan, J.L., Vermote, E.F., Roger, J-C., Skakun, S. V., Justice, C., 2018. The Harmonized Landsat and Sentinel-2 surface reflectance data set. Remote Sens. Environ. 219, 145–161.
Coulombe Commission (Commission d'étude sur la gestion de la forêt publique québécoise), 2004. Chapitre 4: Protection, conservation et gestion multiressource: Des axes de changement. In Commission d'étude sur la gestion de la forêt publique québécoise, Rapport final; Ministère des Forêts, de la Faune et des Parcs: Québec, QC, Canada, 2004; pp.47–92.
Deák, M., Telbisz, T., Árvai, M., Mari, L., Horváth, F., Kohán, B., Szabó, O., Kovács, J., 2017. Heterogeneous forest classification by creating mixed vegetation classes using EO-1 Hyperion. Int. J. Remote Sens. 38 (18), 5215–5231.
Evan, G.C., Coombe, D.E., 1959. Hemisperical and woodland canopy photography and the light climate. J. Ecol. 47 (1), 103–113.
Fettes, J.J., 1950. Investigations of sampling techniques for population studies of the spruce budworm on balsam fir in Ontario. For. Insect Lab. Sault Ste. Marie, Ont., Ann. Tech. Rep. 4. pp. 163–401.
Franklin, S.E., Fan, H., Guo, X., 2008. Relationship between Landsat TM and SPOT vegetation indices and cumulative spruce budworm defoliation. Int. J. Remote Sens. 29 (4), 1215–1220.
Fuentealba, A., Dupont, A., Hébert, C., Berthiaume, R., Quezada-García, R., Bauce, É., 2019. Comparing the efficacy of various aerial spraying scenarios using *Bacillus thuringiensis* to protect trees from spruce budworm defoliation. For. Ecol. Manage. 432, 1013–1021.
Goodbody, T.R.H., Coops, N.C., Hermosilla, T., Tompalski, P., McCartney, G., MacLean, D.A., 2018. Digital aerial photogrammetry for assessing cumulative spruce budworm defoliation and enhancing forest inventories at a landscape-level. ISPRS J. Photogramm. Remote Sens. 142, 1–11.

Gray, D.R., MacKinnon, W.E., 2006. Outbreak patterns of the spruce budworm in Canada. For. Chron. 82 (4).
Hall, R.J., Castilla, G., White, J.C., Cooke, B.J., Skakun, R.S., 2016. Remote sensing of forest pest damage: a review and lessons learned from a Canadian perspective. Can. Entomol. 148, S296–S356.
Hanssen, K.H., Solberg, S., 2007. Assessment of defoliation during a pine sawfly outbreak: calibration of airborne laser scanning data with hemispherical photography. For. Ecol. Manage. 250, 9–16.
Hennigar, C.R., Erdle, T.A., Gullison, J.J., MacLean, D.A., 2013. Re-examining wood supply in light of future spruce budworm outbreaks: a case study in New Brunswick. For. Chron. 89 (1).
Hennigar, C.R., MacLean, D.A., Quiring, D.T., Kershaw, J.A., 2008. Differences in spruce budworm defoliation among balsam fir and white, red, and black spruce. For. Sci. 54 (2), 158–166.
Huang, Z., 2015. Remote sensing of spruce budworm defoliation in Québec, Canada using EO-1 Hyperion data. MScE thesis. University of New Brunswick, Fredericton, NB, Canada.
Kettela, E.G., 1983. A cartographic history of spruce budworm defoliation 1967-1981 in eastern North America. Canadian Forestry Service, Maritime Forest Research Centre, Fredericton, N.B., Canada. Inf. Rep. DPC-X-14.
Kubo, M., Gavrilov, S., Muramoto, K., Kamata, N., 2012. Analysis of fisheye photography for monitoring canopy structure during larch sawfly outbreak, in: IEEE International Geoscience and Remote Sensing Symposium (IGARSS), Munich, Germany. pp. 6352–6355.
Lausch, A., Erasmi, S., King, D.J., Magdon, P., Heurich, M., 2016. Understanding forest health with remote sensing Part I - a review of spectral traits, processes and remote sensing characteristics. Remote Sens. 8 (1029).
Leckie, D.G., Yuan, X., Ostaff, D.P., Piene, H., Maclean, D.A., 1992. Analysis of high resolution multispectral MEIS imagery for spruce budworm damage assessment on a single tree basis. Remote Sens. Environ. 40, 125–136.
Lévesque, R.C., Cusson, M., Lucarotti, C., 2010. BEGAB: Budworm Eco-Genomics: Applications & Biotechnology. Institut de biologie intégrative et des systemès, Université Laval: Québec City, QC, Canada.
Liu, E.Y., Lantz, V.A., MacLean, D.A., Hennigar, C., 2019. Economics of early intervention to suppress a potential spruce budworm outbreak on crown land in New Brunswick, Canada. Forests 10 (481).
Liu, Z., Wang, C., Chen, J.M., Wang, X., Jin, G., 2015. Empirical models for tracing seasonal changes in leaf area index in deciduous broadleaf forests by digital hemispherical photography. For. Ecol. Manage. 351, 67–77.
MacLean, D.A., 1980. Vulnerability of fir-spruce stands during uncontrolled spruce budworm outbreaks: a review and discussion. For. Chron. 56 (5).
MacLean, D.A., Lidstone, R.G., 1982. Defoliation by spruce budworm: estimation by ocular and shoot-count methods and variability among branches, trees, and stands. Can. J. For. Res. 12, 582–594.
MacLean, D.A., MacKinnon, W.E., 1996. Accuracy of aerial sketch-mapping estimates

of spruce budworm defoliation in New Brunswick. Can. J. For. Res. 26, 2099–2108.
MacLean, D.A., MacKinnon, W.E., 1997. Effects of stand and site characteristics on susceptibility and vulnerability of balsam fir and spruce to spruce budworm in New Brunswick. Can. J. For. Res. 27, 1859–1871.
MacLean, D.A., MacKinnon, W.E., 1998. Sample sizes required to estimate defoliation of spruce and balsam fir caused by spruce budworm accurately. North. J. Appl. For. 15 (3).
MacLean, D.A., Ostaff, D.P., 1989. Patterns of balsam fir mortality caused by an uncontrolled spruce budworm outbreak. Can. J. For. Res. 19, 1087–1095.
MacLean, D.A., Porter, K.B., 1994. Development of a decision support system for spruce budworm and forest management planning in Canada. In: Decision Making with GIS - The Fourth Dimension. Vol. 2. Proc. GIS 1994 Symposium, Vancouver, BC. pp. 863–872.
MacLean, D.A., Hunt, T.L., Eveleigh, E.S., Morgan, M.G., 1996. The relation of balsam fir volume increment to cumulative spruce budworm defoliation. For. Chron. 72 (5).
MacLean, D.A., MacKinnon, W.E., Porter, K.B., Beaton, K.P., Cormier, G., Morehouse, S., 2000. Use of forest inventory and monitoring data in the spruce budworm decision support system. Comput. Electron. Agric. 28, 101–118.
MacLean, D.A., Amirault, P., Amos-Binks, L., Carleton, D., Hennigar, C., Johns, R., Régnière, J., 2019. Positive results of an early intervention strategy to suppress a spruce budworm outbreak after five years of trials. Forests 10 (448).
MacLean, D.A., Erdle, T.A., MacKinnon, W.E., Porter, K.B., Beaton, K.P., Cormier, G., Morehouse, S., Budd, M., 2001. The Spruce Budworm Decision Support System: forest protection planning to sustain long-term wood supply. Can. J. For. Res. 31, 1742–1757.
Maxwell, A.E., Warner, T.A., Fang, F., 2018. Implementation of machine-learning classification in remote sensing: an applied review. Int. J. Remote Sens. 39 (9), 2784–2817.
Miller, C.A., 1977. The feeding impact of spruce budworm on balsam fir. Can. J. For. Res. 7, 76–84.
Nealis, V.G., Régnière, J., 2004. Insect-host relationships influencing disturbance by the spruce budworm in a boreal mixedwood forest. Can. J. For. Res. 34, 1870–1882.
Nenzén, H.K., Peres-Neto, P., Gravel, D., 2018. More than Moran: coupling statistical and simulation models to understand how defoliation spread and weather variation drive insect outbreak dynamics. Can. J. For. Res. 48, 255–264.
Oumar, Z., Mutanga, O., Ismail, R., 2013. Predicting *Thaumastocoris peregrinus* damage using narrow band normalized indices and hyperspectral indices using field spectra resampled to the Hyperion sensor. Int. J. Appl. Earth Obs. Geoinf. 21, 113–121.
Pontius, J., Hallett, R., Martin, M., 2005. Using AVIRIS to assess hemlock abundance and early decline in the Catskills, New York. Remote Sens. Environ. 97, 163–173.
Pontius, J., Martin, M., Plourde, L., Hallett, R., 2008. Ash decline assessment in emerald ash borer-infested regions: a test of tree-level, hyperspectral technologies. Remote Sens. Environ. 112, 2665–2676.

Pothier, D., Elie, J.G., Auger, I., Mailly, D., Gaudreault, M., 2012. Spruce budworm-caused mortality to balsam fir and black spruce in pure and mixed conifer stands. For. Sci. 58 (1), 24–33.

Pureswaran, D.S., De Grandpré, L., Pare, D., Taylor, A., Barrette, M., Morin, H., Regniere, J., Kneeshaw, D.D., 2015. Climate-induced changes in host tree-insect phenology may drive ecological state-shift in boreal forests. Ecology 96 (6), 1480–1491.

Québec Ministère des Forêts de la Faune et des Parcs (QMFFP), 2019. Aires infestées par la tordeuse des bourgeons de l'épinette au Québec en 2019 - Québec Ministère des Forêts de la Faune et des Parcs, Direction de la protection des forêts, Québec. 32p.

Rahimzadeh-Bajgiran, P., Weiskittel, A., Kneeshaw, D., MacLean, D., 2018. Detection of annual spruce budworm defoliation and severity classification using Landsat imagery. Forests 9 (357).

Royama, T., 1984. Population dynamics of the spruce budworm *Choristoneura fumiferana*. Ecol. Monogr. 54 (4), 429–462.

Royama, T., Mackinnon, W.E., Kettela, E.G., Carter, N.E., Hartling, L.K., 2005. Analysis of spruce budworm outbreak cycles in New Brunswick, Canada, since 1952. Ecology 86 (5), 1212–1224.

Royama, T., Eveleigh, E.S., Morin, J.R.B., Pollock, S.J., McCarthy, P.C., McDougall, G.A., Lucarotti, C.J., 2017. Mechanisms underlying spruce budworm outbreak processes as elucidated by a 14-year study in New Brunswick, Canada. Ecol. Monogr. 87 (4), 600–631.

Rullan-Silva, C.D., Olthoff, A.E., Delgado de la Mata, J.A., Pajares-Alonso, J.A., 2013. Remote monitoring of forest insect defoliation: a review. For. Syst. 22 (3), 377–391.

Su, Q., MacLean, D.A., Needham, T.D., 1996. The influence of hardwood content on balsam fir defoliation by spruce budworm. Can. J. For. Res. 26, 1620–1628.

Taylor, S.L., MacLean, D.A., 2008. Validation of spruce budworm outbreak history developed from aerial sketch mapping of defoliation in New Brunswick. North. J. Appl. For. 25 (3).

White, J.C., Coops, N.C., Hilker, T., Wulder, M.A., Carroll, A.L., 2007. Detecting mountain pine beetle red attack damage with EO-1 Hyperion moisture indices. Int. J. Remote Sens. 28 (10), 2111–2121.

Zhang, B., MacLean, D.A., Johns, R.C., Eveleigh, E.S., 2018. Effects of hardwood content on balsam fir defoliation during the building phase of a spruce budworm outbreak. Forests 9 (530).

Zhao, K., MacLean, D.A., Hennigar, C.R., 2014. Spatial variability of spruce budworm defoliation at different scales. For. Ecol. Manage. 328, 10–19.

CHAPTER 2: QUANTIFICATION OF FOREST CANOPY CHANGES CAUSED BY SPRUCE BUDWORM DEFOLIATION USING DIGITAL HEMISPHERICAL IMAGERY

Published in the journal *Agricultural and Forest Meteorology* as:

Donovan, S.D., MacLean, D.A., Kershaw, J.A., and Lavigne, M.B. 2018. Quantification of forest canopy changes caused by spruce budworm defoliation using digital hemispherical imagery. Agric. For. Meteorol. 262, 89–99.

2.1. Abstract

Detection of spruce budworm (*Choristoneura fumiferana* Clem.) defoliation is critical for forest protection strategies aimed at minimizing losses in growth and mortality. However, current aerial and ground survey methods of detecting defoliation are imprecise and subjective, limiting their usefulness. We evaluated the use of hemispherical crown canopy images to quantify annual spruce budworm defoliation, comparing images taken before and after defoliation in each of two years in 75 sample plots in Québec, Canada. Gradient Boosting Machine analysis identified gap fraction change from May-October, gap fraction after defoliation, insecticide spraying, and % balsam fir (*Abies balsamea* (L.) Mill.) basal area as important explanatory variables of defoliation. Logistic Generalized Linear Model (GLM) and Random Forests (RF) models were trained on a random two-thirds of sample plots combining both years, and defoliation predictions were validated on the remaining one-third of plots. RF predictions consistently resulted in slightly higher correlations and lower root mean square errors (RMSEs) than GLM predictions. Defoliation models including insecticide spraying, gap fraction change May-October, and % balsam fir basal area had RMSEs of 14–22%, whereas models excluding insecticide spraying had higher RMSEs of 18–24%. Model goodness-of-fit using two-sample Kolmogorov-Smirnov tests indicated that predicted and measured annual defoliation had similar distributions, with the exception of GLM and RF models excluding spray compared to ocular defoliation. The use of hemispherical images to quantify gap fraction change is a feasible, non-destructive, and objective method to assess canopy foliage changes caused by spruce budworm defoliation.

2.2. Introduction

Spruce budworm (*Choristoneura fumiferana* Clem.) outbreaks are a major, episodic natural disturbance in eastern Canadian forests. Spruce budworm larvae repeatedly defoliate the current year foliage of balsam fir (*Abies balsamea* (L.) Mill.) and spruce (*Picea* spp.) (Blais, 1983; Kettela, 1983; MacLean et al., 2001). From 1978–1987, budworm caused an estimated 32–43 million m^3/year of timber volume reduction in Canada (Power, 1991; Sterner and Davidson, 1982). As a result, the economic impacts of spruce budworm outbreaks are severe (Chang et al., 2012; MacLean, 2004). Only aerial spray of biological insecticides can reduce defoliation during an outbreak (Fuentealba et al., 2015) but rescheduling of harvesting can also reduce impacts (Hennigar et al., 2007). The Spruce Budworm Decision Support System (SBW DSS; MacLean et al. 2001) facilitates planning for the integrated use of insecticide spraying, salvage harvesting, and harvest rescheduling to reduce economic impacts (Hennigar et al., 2011, 2007; MacLean et al., 2002). However, use of SBW DSS requires accurate defoliation estimates and predictions.

Methods of measuring spruce budworm defoliation differ with spatial scale, from aerial surveys for regions, to ocular whole-tree assessment for plots, and branch sampling for plots and individual trees (Fettes 1950; MacLean and Lidstone 1982; MacLean and MacKinnon 1998). Aerial surveys are subject to errors due to variability among observers, spatial georeferencing, inconsistency of survey methods, the use of broad and subjective classes (typically light, moderate, severe), and effects of wind and rain altering detectability of defoliation (MacLean and MacKinnon, 1996; Zhao et al., 2014). Ocular

methods are more precise than aerial surveys but are also subject to error due to variation among observers, crown viewing conditions, and difficulties separating defoliation of previous years from current estimates (MacLean and Lidstone, 1982). Branch sampling and assessing defoliation on sampled shoots is the most precise but is time-consuming and sample sizes (number of shoots per branch and branches per plot) are high at moderate defoliation levels (MacLean and MacKinnon 1998).

Hemispherical canopy photographs may be a rapid, repeatable alternative to ocular surveys and branch sampling for measuring defoliation at plot and stand spatial scales due to development of digital cameras and image processing software (Chianucci and Cutini, 2012; Jonckheere et al., 2005; Macfarlane, 2011). Hemispherical photos effectively capture seasonal variation of LAI (Liu et al., 2015), demonstrating sensitivity. In addition, studies investigating the use of airborne laser scanning as an alternative to traditional aerial surveys found that stand-level defoliation estimates by hemispherical photography effectively calibrated airborne laser estimates (Hanssen and Solberg, 2007; Solberg et al., 2006).

We tested the use of hemispherical canopy photos collected before and after spruce budworm defoliation, to assess annual defoliation in 75 sample plots in the Gaspé Peninsula, Quebec, Canada over two years. Our objective was to construct models using metrics derived from hemispherical photos and stand attributes to explain variations in defoliation measured by ocular surveys and branch sampling. We compared the use of logistic Generalized Linear Model (GLM) (parametric) and Random Forests (RF) (non-parametric) methods to create these models. In addition, we examined whether models apply to both insecticide sprayed and unsprayed plots.

2.3. Methods

2.3.1. Study area

The study area was located in the central Gaspé Peninsula in Québec, Canada, in the Great Lakes-St. Lawrence Forest Region, section L6 Témiscouata-Restigouche (Rowe, 1972). It is identified as a balsam fir-white birch (*Betula papyrifera* Marsh.) mixed forest ecodistrict (Bélanger et al. 1992). The landscape consists of rolling topography with elevations ranging from 275 to 575 metres (m), with mean annual temperatures between 0 °C and 2.5 °C and growing degree days of 150 to 160 days (Archambault et al., 1998).

Balsam fir and white spruce (*Picea glauca* (Moench) Voss) are abundant at lower elevations in valleys (Rowe, 1972). Black spruce (*Picea mariana* (Mill.) B.S.P.), along with balsam poplar (*Populus balsamifera* L.), trembling aspen (*Populus tremuloides* Michx.), white birch, eastern white cedar (*Thuja occidentalis* L.), eastern white pine (*Pinus strobus* L.), and eastern larch (*Larix laricina* (*Du Roi*) K. Koch) also occur (Rowe, 1972).

The most recent spruce budworm outbreak was first detected in 2012 on the Gaspé Peninsula. Spruce budworm defoliation began in the study area in 2014, and areas of light, moderate, and severe defoliation increased rapidly in 2015 and 2016 (Figure 2.1) (Québec Ministère des Forêts de la Faune et des Parcs (QMFFP), 2016).

2.3.2. Plot establishment and data collection

A total of 75 sample plots were selected in 2014, with 22 plots northeast of Amqui and 53 plots southwest of Causapscal (Figure 2.1). Circular 0.04 ha plots were

established at least 75 m apart, with plot groupings ranging from 1 to 6 per stand. Criteria for plot selection included forested conditions dominated by spruce budworm host species (balsam fir and spruce) and the full range of current defoliation present at the time of plot establishment (we attempted to locate 10 plots in each 10% current defoliation class from 0 to 100% to achieve a balanced sampling design).

At the time of plot establishment, each tree ≥ 3cm diameter at breast height (DBH; at 1.3m) was measured for species, DBH to the nearest 0.1 cm, total and live crown heights to the nearest 0.1 m (measured with Vertex III and Transponder T3, Haglöf, Sweden), crown widths in the four cardinal directions to the nearest 0.1 m, and location (distance and azimuth direction from plot center).

Current annual defoliation was measured in each plot in 2015 and 2016, using both ocular and branch sampling methods in late July to early August, after spruce budworm feeding ceased. For ocular sampling, annual defoliation of each tree ≥ 10 cm DBH was assessed using binoculars and assigned to one of seven defoliation classes (0, 1–20, 21–40, 41–60, 61–80, 81–99, or 100%). Ocular assessments were based on observing the entire crown of each tree for loss of current annual foliage. Mean annual ocular defoliation per plot for each year was calculated by assigning class midpoints for each tree, weighted by the percent individual tree basal area to the total spruce budworm host species basal area per plot, and summed.

Branch sampling of current annual defoliation per year also used the same seven percentage defoliation classes. One mid-crown branch per tree was sampled from 8 to 15 trees per host species (balsam fir, white spruce, black spruce) per plot, based on species and defoliation-level minimum sample sizes required to estimate mean defoliation with

90% confidence and ±10% error (MacLean and MacKinnon 1998). Defoliation was recorded on each of 25 randomly selected current year shoots (MacLean and MacKinnon 1998) per branch, and the mean calculated. Mean annual branch defoliation per plot was calculated using defoliation of each sample branch, weighted by the relative tree basal area.

We adjusted both ocular and branch defoliation values to account for zero defoliation on non-spruce budworm host species per plot by multiplying by 1 – P, where P is the proportion of basal area of non-spruce budworm host species. Mean annual branch defoliation per plot data was used for model calibration and training as it is the most accurate survey method.

2.3.3. Hemispherical image acquisition and processing

Hemispherical photos were taken at four permanently marked locations per plot, facilitating canopy change detection (Figure 2.2). Camera locations were approximately 6 m from plot centre in the cardinal directions (north, east, south, and west), positioned to avoid understory vegetation, and marked to allow repeated placement of the camera lens 1.2 m above ground. Photos were taken at three times during the growing season in 2015 and 2016: in May before shoot emergence, in July after spruce budworm feeding ceased, and in late October, after leaf fall of deciduous trees. At each plot camera location and acquisition date several photos were taken across a range of camera exposure settings (–1.0, –0.7, –0.3, 0.0, 0.3, 0.7, 1.0, relative to first setting the camera to aperture priority mode, setting the lens aperture manually to eight, and focus ring position to infinity) avoiding many of the exposure determination issues such as the effects of varying sky

conditions and sun angles (Beckschäfer et al., 2013; Zhang et al., 2005). According to Chen et al. (1991) and Zhang et al. (2005), automatic exposure causes overestimation of gap fraction and underestimation of effective LAI. Since our study is based on relative change, this systematic bias may not influence conclusions, but we used and tested the effects of several manual exposure settings. Sky conditions at the times of image acquisition ranged from clear blue and sunny to overcast cloudy skies, all during low wind speed conditions.

The hemispherical camera system uses a Sony 24 megapixel digital single-lens reflex camera with a 180-degree fish-eye lens, mounted to an O-Mount magnetic NorthFinder with bubble level and sun blocker attachments (Regent Instruments Inc., Quebec, Canada), mounted to a camera tripod suitable for forest terrain. All images were stored in JPEG format (6000 x 4000 pixels resolution).

All digital hemispherical images were analyzed for gap fraction using ImageJ version 1.50i (Rasband, 2016), along with the macro plugin, Hemispherical_2.0 (Donovan et al., 2018). The plugin includes the “Minimum” thresholding algorithm (Prewitt and Mendelsohn, 1966) for classifying each image pixel as vegetation or sky, which has been shown to produce above-average accuracies among the many binarization algorithms (Glatthorn and Beckschäfer, 2014). For each image, a bimodal gray value histogram was iteratively smoothed using a running average until a single minimum between two modes was reached in the histogram and selected as the global threshold for image binarization (Glatthorn and Beckschäfer, 2014) (Figure 2.2b). Circular masking of each image was first performed to analyze zenith angles ranging from 0–70°(Chen et al., 2006). Only the blue colour channel was used for analysis because it provides the best

sky to vegetation contrast (Brusa and Bunker, 2014; Leblanc et al., 2005). Outputs from ImageJ analysis for each image included: number of gaps, total gap area (pixels), and percent gap fraction.

2.3.4. Defoliation explanatory variables and variable importance analysis

Windthrow, problematic sky conditions that compromised image analyses, or harvesting of several plots reduced sample sizes to 72 plots in 2015 (three plots removed due to sky condition) and 68 plots in 2016 (two plots removed due to windthrow and five plots were harvested) leaving a combined sample size of 140 plots. After testing the effects of the several manual exposure settings, average plot gap fraction was calculated for each acquisition date using the three intermediate camera exposure settings (–0.3, 0.0, 0.3) taken from all four camera locations per plot. The three middle exposure values were selected with the aim of achieving consistent gap fraction estimates and comparisons over time at multiple sites with less concern for systematic bias as long as variance was relatively constant along the gap fraction gradient. Preliminary findings post image processing showed the middle exposures consistently classified image pixels well across various sky and lighting conditions. Consideration was given to limit significant errors often associated with dark blue sky pixels being classified as vegetation and sunlight tree stems/crowns being classified as sky.

A total of 30 gap fraction, gap fraction change, and plot attribute variables were evaluated for their explanatory power in relation to percent annual branch defoliation per plot (Table 2.1). Single date (May, July, October) average plot gap fraction variables were included to see whether total gap fraction, in addition to gap fraction change, might

reflect differences in sample plot species composition and density. Gap fraction change (GFC) and gap fraction ratio (GFR) variables (Table 2.1) were calculated for periods May-July, July-October, and May-October. Basal area, percent basal area, and density by tree host species (balsam fir, white spruce, and black spruce), non-host softwood species, and hardwood species per plot were also calculated, to address possible effects of specific host and nonhost species stand structure conditions (Table 2.1). Evaluation of plot variables was important because stand species composition and age are important determinants of stand vulnerability to spruce budworm defoliation, with balsam fir content the most important (Sainte-Marie et al., 2015). Non-host species hardwood content has been shown to reduce balsam fir defoliation (Su et al., 1996). Basal area was selected as a measure of stand species composition because it is closely related to crown biomass (Coyea and Margolis, 1992). Finally, an indicator variable for insecticide spraying was included to differentiate insecticide sprayed and non-sprayed plots based on a minimum distance of 250 m from spraying. Aerial spraying is commonly applied because it is highly effective at reducing budworm populations and defoliation (Fuentealba et al., 2015).

We used the R statistical software package (R Development Core Team, 2016) and the "train" function in the caret package (Kuhn, 2008) to perform Gradient Boosting Machine (GBM) analysis (Ridgeway, 2007) to select strong explanatory variables prior to modelling defoliation. One of the outputs from GBM analysis is the relative influence (variable importance) of each explanatory variable, which measures the number of times variables are selected for splitting weighted by the squared improvement to the model (Elith et al., 2008; Friedman, 2001). Relative influence results for the 30 explanatory

variables (Table 2.1) were scaled so that the sum added to 100, with values indicating the percentage influence on the response variable annual branch defoliation per plot. Model parameters used for GBM relative influence analysis included train function parameters "GBM" for method and "RMSE" for metric. Relative influence analyses were conducted on the combined dataset of 140 plots from both sampling years while including and excluding the Spray variable to determine whether hemispherical data alone could accurately assess defoliation of sprayed and unsprayed plots in multiple years.

The selection of model explanatory variables combined relative influence results and multicollinearity diagnostics. Significant data multicollinearity influences interpretability for model prediction methods such as GLM and RF (Dormann et al., 2013). Pairwise collinearity diagnostics (e.g., correlation matrix) using a rule-of-thumb $r > 0.7$ (Dormann et al., 2013) identified variables to remove. We reduced variable candidates to three variables, selecting for strong relative influence and collinearity below $r < 0.7$. Preliminary modelling of defoliation indicated that additional model variables did not significantly increase the model variance explained. Pairwise scatterplots and Pearson's and Point-Biserial correlations (r) aided in examining the relationship between the selected variables and annual branch defoliation by year and for combined years.

2.3.5. Model selection and validation

We compared GLM and RF methods to use hemispherical image change detection and forest structure values to predict annual defoliation per plot. GLMs allow for specification of the error distribution, modelling family, and link function appropriate for a particular modelling task (Lopatin et al., 2016), e.g., logistic regression for dealing with

discrete response variables ranging from 0–1. RF methods are robust to overfitting (L. Breiman, 2001) and can handle categorical, continuous, and discrete explanatory and response variables (Penner et al., 2013). We used the R statistical software and partitioned the combined dataset of 140 plots from both sampling years into a random two-thirds data (96) for training and one-third (44) retained for validating models (Morrison et al., 2013). Using a stepwise approach, we tested all possible model combinations including the top three explanatory variables, including and excluding Spray, because some jurisdictions do not use insecticide spraying.

For logistic GLMs, a binomial family distribution and logit link function appropriate for discrete/bounded data were used. The response variable annual branch defoliation per plot was transformed to 0–1 by dividing by 100. RF models used randomForest (Liaw and Wiener 2002), with parameters ntree = 500 (total number of trees to be grown in a model run) and mtry = 1 (number of predictor variables randomly sampled at each node split). The same model response and explanatory variables were used in GLM and RF models. GLM and RF models were each used to predict annual defoliation for the retained 44 validation sample plots using the "glm.predict" and RF "predict" functions. Predicted defoliation was back-transformed to a percentage by multiplying by 100.

Model performance was evaluated using mean bias, mean absolute bias (MAB) and root mean square error (RMSE) calculated from model residuals for the random 44 sample plots retained for model validation. Bias indicates systematic error, whereas MAB and RMSE measure the magnitude/deviation between predictions and observations or variance explained. We placed more importance on lower RMSE values as this penalizes

larger errors. For assessing model goodness-of-fit, the two-sample Kolmogorov-Smirnov (KS) test (Massey, 1951) with a significance level of $\alpha = 0.05$ was used. The nonparametric KS test does not assume normality and enabled pairwise comparisons of model-predicted and measured annual defoliation. Formally, the test evaluates the null hypothesis that the two datasets come from a common distribution and the alternative hypothesis infers the datasets are not from a common distribution. Testing differences of their respective shape distributions was calculated using the cumulative distribution function and reporting the largest absolute difference (test statistic D) between the two datasets.

2.4. Results

2.4.1. Sample plot characteristics and defoliation

Mean tree density of the 75 plots sampled was 2030 stems·ha^{-1}, mean DBH 13.9 cm, mean tree height 14.7 m, and mean basal area 44 m^2·ha^{-1} (Table 2.2). Species composition of plots averaged 92% spruce budworm host species, including 64% (by basal area) balsam fir, 19% black spruce, and 9% white spruce, along with 6% hardwoods (deciduous), and 2% other softwood species (Table 2.2). A total of 32 plots (43%) in 2015 and 19 plots (28%) in 2016 were affected by insecticide spraying to reduce defoliation. Sampling these plots was the only way to obtain low defoliation levels in the study area.

Spruce budworm defoliation measured by branch sampling ranged from 0 to 99% in 2015 and 2 to 98% in 2016, while ocular defoliation ranged from 4 to 93% in 2015 and from 4 to 90% in 2016 (Table 2.2). Correlations between branch and ocular defoliation

were r = 0.94 and 0.90 for 2015 and 2016, respectively (Figure 2.3). Mean defoliation was higher in 2015 than 2016 for both branch sampling (52% vs. 35%) and ocular defoliation (49% vs. 28%) (Figure 2.3). Distribution of plots in four 25% annual branch defoliation classes (i.e., 0–25, 26–50, 51–75 and 76–100%) had 31, 13, 24 and 32% of plots in the four classes in 2015 and 39, 37, 14 and 10% in 2016.

Annual branch defoliation of balsam fir averaged 58% in 2015 and 44% in 2016, whereas defoliation of the less abundant black and white spruces (combined) averaged 28% and 10%, respectively (Figure 2.3). With lower spruce budworm populations in 2016, defoliation of spruce (32 plots) was generally less than 20%, whereas defoliation of balsam fir ranged up to near 100% (Figure 2.3).

2.4.2. GBM analysis of relative influence of explanatory variables

Spray had the strongest relative influence of any explanatory variable at 43%, followed by Gap Fraction Change May-October (GFC_MO) at 15% and balsam fir % basal area (BF_BA%) at 10%, combining for 68% of the total relative influence (Figure 2.4a). Correlation analysis indicated that Spray, GFC_MO and BF_BA% were not collinear, and we selected these three variables as model candidates (Figure 2.4a). The remaining 27 variables had lower relative influence ranging from 0 to 5% and had numerous collinearity issues with the top three variables; hence they were not used in subsequent analyses (Figure 2.4a).

Excluding the Spray variable and keeping sprayed plots in the analysis, the top three explanatory variables were GFC_MO at 25% relative influence, BF_BA% at 10%, and Gap Fraction Ratio from May-October (GFR_MO) at 8% (Figure 2.4b). These

variables combined for 43% of the total relative influence. The third strongest ranked variable GFR_MO was highly correlated (r = 0.95) with GFC_MO, so we replaced it with the next strongest ranked variable, Gap Fraction in October (GF_October), with relative influence 7%, in subsequent model building (Figure 2.4b).

2.4.3. Relationship of defoliation to explanatory variables

Annual branch defoliation and GFC_MO were linearly correlated (r = 0.58 in 2015, 0.32 in 2016, and 0.49 combining both years), indicating stronger association than other variables (Figure 2.5a). Annual branch defoliation and BF_BA% had the weakest correlations r = 0.28 in 2015, 0.24 in 2016, and 0.24 combining years (Figure 2.5b). GF_October had consistent but weak correlation with annual branch defoliation, with r = 0.35 for 2015 and 2016, and 0.33 combining both years (Figure 2.5c). Finally, the Spray variable had the strongest correlation with annual branch defoliation, with r = -0.81 in 2015, -0.60 in 2016, and -0.65 combining both years. Most plots that were sprayed had < 50% measured branch defoliation (Figure 2.5d).

2.4.4. Predicted annual defoliation from GLM and RF models

Logistic GLM and RF-fit models more successfully explained defoliation for the 44 validation plots when Spray was included as a variable (Table 2.3). The best overall models included the variables Spray, GFC_MO, and BF_BA%, with biases of 1.1 and -0.1%, MABs of 15.5 and 15.1% and RMSEs of 18.8 and 18.2% for GLM and RF, respectively (Table 2.3). For models excluding Spray, the RF model including GFC_MO, BF_BA%, and GF_October was best, with bias = -1.6%, MAB = 18.2%, and RMSE = 21.1% (Table 2.3). The best GLM excluding Spray included GFC_MO and BF_BA%

and had bias = -0.5%, MAB = 18.0%, and RMSE = 22.4% (Table 2.3). Overall, fit parameters were more often better for RF models than GLM models, in pairwise comparisons.

2.4.5. Comparing defoliation predicted by GLM and RF models with measured defoliation

Pearson correlation coefficients between observed (branch) and predicted annual defoliation for the 44 validation sample plots were higher for models including Spray versus models excluding Spray, and RMSE was lower (Figure 2.6). Fit statistics of RF models were not consistently different from those of GLM. Comparisons between ocular defoliation estimates, which are faster and more commonly used in many studies, and model predicted defoliation were substantially similar to those using branch defoliation, although RMSE and correlation statistics for combined years were generally slightly worse (Figure 2.7).

All KS tests of pairwise comparisons between model predicted versus measured annual defoliation indicated no statistical differences in their shape distributions, except for the GLM and RF models excluding Spray versus measured ocular defoliation (Table 2.4). The GLM including Spray assessed against measured branch defoliation had the lowest maximum difference of all predicted versus measured defoliation, but other results were generally similar (Table 2.4). However, measured branch versus ocular defoliation and GLM versus RF predicted defoliation with both models excluding spray had the best results (Table 2.4).

2.5. Discussion

2.5.1. Gap fraction metrics for predicting defoliation

Our analysis of gap fraction variables derived from hemispherical imagery showed that the May-October change variable GFC_MO was the best imagery-derived predictor of defoliation. These two image acquisitions reflected changes from before to after annual defoliation and were both primarily leaf-off periods for deciduous trees. Gap fraction October also showed value in predicting defoliation; it reflected a measure of post-defoliation canopy conditions and possibly contributed differences in canopy conditions among plots, which were selected to be generally similar highly vulnerable mature balsam fir. The timing of image acquisitions is an important factor in remote sensing insect damage using change detection methods (Cielsa, 2000). Solberg et al. (2006) similarly showed success using LAI change detection methods between hemispherical imagery, LAI-2000 instruments and airborne laser scanning data during a European pine sawfly (*Neodiprion sertifer* Geoffroy) outbreak.

2.5.2. Comparison of GLM and RF models of defoliation

GLM (parametric) and RF (non-parametric) defoliation prediction models had comparable variance explained results, with RMSEs from 13.7 to 23.9%, although RF models consistently had slightly lower errors. The slight advantage for RF models may have resulted from our sample plots encompassing a large range of gap fraction changes caused by defoliation, because RF, like other imputation methods, do not extrapolate well beyond the training data (Hayashi et al., 2016; Penner et al., 2013). Other studies have shown varying results comparing GLM and RF models: Lopatin et al. (2016) concluded

that GLM methods were superior for modelling species richness count data, whereas Penner et al. (2013) suggested RF methods were superior using airborne laser data for predicting forest inventory attributes.

2.5.3. Inclusion of insecticide spraying variable improves defoliation predictions

Annual branch defoliation had the highest correlation with Spray of any variable tested. Defoliation prediction accuracy was improved somewhat for models including the Spray variable, with lower RMSE by 2.9% for RF and 3.7% for GLM, compared to models excluding Spray. Including the Spray variable in models predicting defoliation with hemispherical imagery is recommended, and it is already an important input to SBW DSS and defoliation-based growth models (MacLean, 1996).

2.5.4. Accuracy of defoliation models compared to branch and ocular defoliation

Model goodness-of-fit tests showed that defoliation predicted by GLM and RF models and measured annual defoliation had similar distributions with acceptable RMSE errors. Two exceptions were GLM and RF models excluding Spray compared to ocular defoliation as KS tests rejected the null hypothesis that the shape distributions were similar. Also, linear correlations indicated overestimation at low defoliation and underestimation at high defoliation severities. MacLean and Lidstone (1982) similarly found errors (20–30%) of overestimating budworm defoliation at low levels using the ocular method, underlining the challenge of detecting low defoliation. Difficulties of separating annual defoliation from previous defoliation through binoculars is likely a contributing factor for ocular surveys, which is avoided using our change detection hemispherical method.

Factors complicating the relationship between canopy gap fraction change and spruce budworm defoliation include variation in weather and sky conditions during image acquisition, high variability in stand canopy structure, and image processing procedures (Hall et al. 2003). Diffuse overcast is the optimal weather condition to acquire images (Frazer et al., 2001), although requiring ideal weather conditions for hemispherical-based defoliation surveys would be impractical. Individual tree defoliation levels are highly variable at low to moderate defoliation levels (MacLean and Lidstone 1982), and may not be fully captured by four hemispherical photos per plot. Finally, our approach using image batch processing with the "Minimum" thresholding algorithm and averaging of gap fraction was an attempt to reduce image processing requirements, and although other image processing options exist that potentially could improve results, they require user input increasing processing time.

Our approach of relating gap fraction changes to budworm defoliation was focused on achieving a viable, simple, and flexible photo-based defoliation survey method. Ideally, diffuse overcast sky conditions are recommended (Chianucci and Cutini, 2012; Leblanc et al., 2005), and results may be better for balsam fir stands with foliage arranged on a more horizontal plane than in spruce species with foliage covering all angles (Boyce, 1993). Hemispherical image-derived gap fraction change was sensitive to annual spruce budworm defoliation and can be a viable ground-based survey method in repeated measurement plots. Our method also has potential for determining cumulative defoliation and as a defoliation survey method for other defoliating insects. Hemispherical imagery has an advantage over branch and ocular defoliation methods as it quantifies the foliage remaining rather than the proportion of foliage removed, which could help improve

prediction of tree and stand response to defoliation. Hemispherical imagery is widely applied as calibration data in aerial laser scanning and satellite-based remote sensing studies (Hall et al., 2016).

2.6. Conclusions

We demonstrated that hemispherical imagery-derived canopy gap fraction change variables, combined with balsam fir % basal area and an aerial insecticide spray variable, can be used to predict annual budworm defoliation. Both GLM and RF modelling methods were similar in performance, although RF consistently had slightly lower prediction errors and higher correlations. Including an aerial spraying variable reduced defoliation prediction RMSE of the full models by 2.9 to 3.7% and is recommended if applicable. Model-predicted defoliation (GLM including Spray was best) and measured annual defoliation had statistically similar shape distributions, indicating acceptable model goodness-of-fit except for models excluding Spray compared with ocular defoliation. Hemispherical imagery-derived canopy gap fraction methods have potential for use in spruce budworm monitoring programs and in determining cumulative defoliation, especially for permanent sample plots used in calibrating relationships between tree growth, survival, defoliation, and foliage remaining on trees.

2.7. Acknowledgements

This research was funded an AWARE (Assessment of Wood Attributes using Remote Sensing) Natural Sciences and Engineering Research Council of Canada Collaborative Research and Development grant to a Canada wide team led by Dr.

Nicholas Coops at the University of British Columbia in partnership with J.D. Irving, Limited. Also, special thanks to the Gretta Goodine (Canadian Forest Service, Atlantic Forestry Centre) and assistants who helped with field data collection: Maggie Brewer, Jessica Cormier, Olivia Doran, Evan Dracup, Matt Hill, Sean Lamb, Rebecca Landry, and Bo Zhang.

2.8. References

Archambault, L., Morissette, J., Bernier-Cardou, M., 1998. Forest succession over a 20-year period following clearcutting in balsam fir-yellow birch ecosystems of eastern Québec, Canada. For. Ecol. Manage. 102, 61–74.

Beckschäfer, P., 2015. Hemispherical_2.0 – Batch processing hemispherical and canopy photographs with ImageJ – User Manual. Chair of Forest Inventory and Remote Sensing, Georg- August-Universität Göttingen, Germany. www.uni-goettingen.de/en/75936.html

Beckschäfer, P., Seidel, D., Kleinn, C., Xu, J., 2013. On the exposure of hemispherical photographs in forests. iForest - Biogeosciences For. 6, 228–237.

Bélanger, L., Bergeron, Y., Camiré, C., 1992. Ecological land survey in Quebec. For. Chron. 68 (1).

Blais, J.R., 1983. Trends in the frequency, extent, and severity of spruce budworm outbreaks in eastern Canada. Can. J. For. Res. 13, 539–547.

Boyce, R.L., 1993. A comparison of red spruce and balsam fir shoot structures. Tree Physiol. 12, 217–230.

Breiman, L., 2001. Random Forests. Mach. Learn. 45, 5–32.

Brusa, A., Bunker, D.E., 2014. Increasing the precision of canopy closure estimates from hemispherical photography: blue channel analysis and under-exposure. Agric. For. Meteorol. 195–196, 102–107.

Chang, W.Y., Lantz, V.A., Hennigar, C.R., MacLean, D.A., 2012. Economic impacts of forest pests: a case study of spruce budworm outbreaks and control in New Brunswick, Canada. Can. J. For. Res. 42, 490–505.

Chen, J.M., Black, T.A., Adams, R.S., 1991. Evaluation of hemispherical photography for determining plant area index and geometry of a forest stand. Agric. For. Meteorol. 56, 129–143.

Chen, J.M., Govind, A., Sonnentag, O., Zhang, Y., Barr, A., Amiro, B., 2006. Leaf area index measurements at Fluxnet-Canada forest sites. Agric. For. Meteorol. 140, 257–268.

Chianucci, F., Cutini, A., 2012. Digital hemispherical photography for estimating forest canopy properties: current controversies and opportunities. iForest - Biogeosciences For. 5, 290–295.

Cielsa, W.M., 2000. Remote Sensing in Forest Health Protection. United States Department of Agriculture Forest Service, Forest Health Technology Enterprise Team, Salt Lake City, Utah. FHTET Report No.00–03.
Coyea, M.R., Margolis, H.A., 1992. Factors affecting the relationship between sapwood area and leaf area of balsam fir. Can. J. For. Res. 22, 1684–1693.
Dormann, C.F., Elith, J., Bacher, S., Buchmann, C., Carl, G., Carré, G., Marquéz, J.R.G., Gruber, B., Lafourcade, B., Leitão, P.J., Münkemüller, T., Mcclean, C., Osborne, P.E., Reineking, B., Schröder, B., Skidmore, A.K., Zurell, D., Lautenbach, S., 2013. Collinearity: a review of methods to deal with it and a simulation study evaluating their performance, Ecography. 36, 27–46.
Elith, J., Leathwick, J.R., Hastie, T., 2008. A working guide to boosted regression trees. J. Anim. Ecol. 77, 802–813.
Fettes, J.J., 1950. Investigations of sampling techniques for population studies of the spruce budworm on balsam fir in Ontario. Forest Insect Laboratory, Sault Ste. Marie, Ont., Ann. Tech. Rep. 4. pp. 163–401.
Frazer, G.W., Fournier, R.A., Trofymow, J.A., Hall, R.J., 2001. A comparison of digital and film fisheye photography for analysis of forest canopy structure and gap light transmission. Agric. For. Meteorol. 109, 249–263.
Friedman, J.H., 2001. Greedy function approximation: a gradient boosting machine. Ann. Stat. 29 (5), 1189–1232.
Fuentealba, A., Bauce, É., Dupont, A., 2015. *Bacillus thuringiensis* efficacy in reducing spruce budworm damage as affected by host tree species. J. Pest Sci. 88, 593–603.
Glatthorn, J., Beckschäfer, P., 2014. Standardizing the protocol for hemispherical photographs: accuracy assessment of binarization algorithms. PLoS ONE 9 (11), e111924.
Hall, R.J., Castilla, G., White, J.C., Cooke, B.J., Skakun, R.S., 2016. Remote sensing of forest pest damage: a review and lessons learned from a Canadian perspective. Can. Entomol. 148, S296–S356.
Hall, R.J., Fernandes, R.A., Hogg, E.H., Brandt, J.P., Butson, C., Case, B.S., Leblanc, S.G., 2003. Relating aspen defoliation to changes in leaf area derived from field and satellite remote sensing data. Can. J. Remote Sens. 29, 299–313.
Hanssen, K.H., Solberg, S., 2007. Assessment of defoliation during a pine sawfly outbreak: calibration of airborne laser scanning data with hemispherical photography. For. Ecol. Manage. 250, 9–16.
Hayashi, R., Weiskittel, A., Kershaw, J.A., 2016. Influence of prediction cell size on LiDAR-derived area-based estimates of total volume in mixed-species and multicohort forests in northeastern North America. Can. J. Remote Sens. 42, 473–488.
Hennigar, C.R., MacLean, D.A., Porter, K.B., Quiring, D.T., 2007. Optimized harvest planning under alternative foliage-protection scenarios to reduce volume losses to spruce budworm. Can. J. For. Res. 37, 1755–1769.
Hennigar, C.R., Wilson, J.S., MacLean, D. A., Wagner, R.G., 2011. Applying a spruce budworm decision support system to Maine: projecting spruce-fir volume impacts under alternative management and outbreak scenarios. J. For. 109, 332–342.
Jonckheere, I., Nackaerts, K., Muys, B., Coppin, P., 2005. Assessment of automatic gap

fraction estimation of forests from digital hemispherical photography. Agric. For. Meteorol. 132, 96–114.
Kettela, E.G., 1983. A cartographic history of spruce budworm defoliation 1967 to 1981 in eastern North America. Canadian Forestry Service, Maritime Forest Research Centre, Fredericton, N.B., Canada. Inf. Rep. DPC-X-14.
Kuhn, M., 2008. Building predictive models in R using the caret package. J. Stat. Softw. 28 (5).
Leblanc, S.G., Chen, J.M., Fernandes, R., Deering, D.W., Conley, A., 2005. Methodology comparison for canopy structure parameters extraction from digital hemispherical photography in boreal forests. Agric. For. Meteorol. 129, 187–207.
Liaw, A., Wiener, M., 2002. Classification and regression by randomForest. R news 2, 18–22.
Liu, Z., Wang, C., Chen, J.M., Wang, X., Jin, G., 2015. Empirical models for tracing seasonal changes in leaf area index in deciduous broadleaf forests by digital hemispherical photography. For. Ecol. Manage. 351, 67–77.
Lopatin, J., Dolos, K., Hernández, H.J., Galleguillos, M., Fassnacht, F.E., 2016. Comparing Generalized Linear Models and Random Forest to model vascular plant species richness using LiDAR data in a natural forest in central Chile. Remote Sens. Environ. 173, 200–210.
Macfarlane, C., 2011. Classification method of mixed pixels does not affect canopy metrics from digital images of forest overstorey. Agric. For. Meteorol. 151, 833–840.
MacLean, D.A., 1996. The role of stand dynamics model in the spruce budworm decision support system. Can. J. For. Res. 26, 1731–1741.
MacLean, D.A., 2004. Predicting forest insect disturbance regimes for use in emulating natural disturbance. In: Perera, A.H., Buse, L.J., Weber, M.G. (Eds.), Emulating Natural Forest Landscape Disturbance: Concepts and Applications. Columbia University Press, New York, pp. 69–82.
MacLean, D.A., Lidstone, R.G., 1982. Defoliation by spruce budworm: estimation by ocular and shoot-count methods and variability among branches, trees, and stands. Can. J. For. Res. 12, 582–594.
MacLean, D.A., MacKinnon, W.E., 1996. Accuracy of aerial sketch-mapping estimates of spruce budworm defoliation in New Brunswick. Can. J. For. Res. 26, 2099–2108.
MacLean, D.A., MacKinnon, W.E., 1998. Sample sizes required to estimate defoliation of spruce and balsam fir caused by spruce budworm accurately. North. J. Appl. For. 15 (3).
MacLean, D.A., Beaton, K.P., Porter, K.B., MacKinnon, W.E., Budd, M.G., 2002. Potential wood supply losses to spruce budworm in New Brunswick estimated using the Spruce Budworm Decision Support System. For. Chron. 78 (5).
MacLean, D.A., Erdle, T.A., MacKinnon, W.E., Porter, K.B., Beaton, K.P., Cormier, G., Morehouse, S., Budd, M., 2001. The Spruce Budworm Decision Support System: forest protection planning to sustain long-term wood supply. Can. J. For. Res. 31, 1742–1757.
Massey, F.J. Jr., 1951. The Kolmogorov-Smirnov test for goodness of fit. J. Am. Stat.

Assoc. 46 (253), 68–78.
Morrison, R.E., Bryant, C.M., Terejanu, G., Prudhomme, S., Miki, K., 2013. Data partition methodology for validation of predictive models. Comput. Math. with Appl. 66, 2114–2125.
Penner, M., Pitt, D.G., Woods, M.E., 2013. Parametric vs. nonparametric LiDAR models for operational forest inventory in boreal Ontario. Can. J. Remote Sens. 39, 426–443.
Power, J.M., 1991. National data on forest pest damage. *In* Canada's timber resources. Edited by D.G. Brand. Canadian Forest Service, Petewawa National Forest. Inf. Rep. PI-X-101. pp. 119–129.
Prewitt, J.M.S., Mendelsohn, M.L., 1966. The analysis of cell images. Ann. N. Y. Acad. Sci. 128, 1035–1053.
Québec Ministère des Forêts de la Faune et des Parcs (QMFFP), 2016. Aires infestées par la tordeuse des bourgeons de l'épinette au Québec en 2016 - Québec Ministère des Forêts de la Faune et des Parcs, Direction de la protection des forêts, Québec. 16p.
R Development Core Team, 2016. R: A language and environment for statistical computing. Vienna, Austria: R Foundation for Statistical Computing. https://cran.r-project.org/.
Rasband, W.S., 2016. ImageJ. U.S. National Institutes of Health, Bethesda, Maryland, USA. https://imagej.nih.gov/ij/.
Ridgeway, G., 2007. Generalized Boosted Models: a guide to the gbm package. R package vignette. 12p. http://cran.r-project.org/package=gbm.
Rowe, J.S., 1972. Forest Regions of Canada. Canadian Forestry Service. Ottawa, Canada. Publication 1300.
Sainte-Marie, G.B., Kneeshaw, D.D., MacLean, D.A., Hennigar, C.R., 2015. Estimating forest vulnerability to the next spruce budworm outbreak: will past silvicultural efforts pay dividends? Can. J. For. Res. 45, 314–324.
Solberg, S., Næsset, E., Hanssen, K.H., Christiansen, E., 2006. Mapping defoliation during a severe insect attack on Scots pine using airborne laser scanning. Remote Sens. Environ. 102, 364–376.
Sterner, T.E., Davidson, A.G., 1982. Forest insect and disease conditions in Canada 1981. Canadian Forest Service, Ottawa, Ont.
Su, Q., MacLean, D.A., Needham, T.D., 1996. The influence of hardwood content on balsam fir defoliation by spruce budworm. Can. J. For. Res. 26, 1620–1628.
Zhang, Y., Chen, J.M., Miller, J.R., 2005. Determining digital hemispherical photograph exposure for leaf area index estimation. Agric. For. Meteorol. 133, 166–181.
Zhao, K., MacLean, D.A., Hennigar, C.R., 2014. Spatial variability of spruce budworm defoliation at different scales. For. Ecol. Manage. 328, 10–19.

Table 2.1: Description of 30 plot-level explanatory variables investigated in GBM analysis to determine the relative influence (variable importance) in relation to the response variable percent annual branch defoliation per plot.

Explanatory variable	Description
Spray	Aerial insecticide application
BF_BA%	Balsam fir basal area %
BS_BA%	Black spruce basal area %
WS_BA%	White spruce basal area %
SP_BA%	Spruce basal area %
SBW_BA%	Spruce budworm host species basal area %
HW_BA%	Hardwood basal area %
NonSBW_BA%	Non-spruce budworm host species basal area %
BF_BA	Balsam fir basal area per plot (m^2/ha)
BS_BA	Black spruce basal area per plot (m^2/ha)
WS_BA	White spruce basal area per plot (m^2/ha)
SP_BA	Spruce basal area (m^2/ha)
SBW_BA	Spruce budworm host species basal area (m^2/ha)
HW_BA	Hardwood basal area per plot (m^2/ha)
NonSBW_BA	Non-spruce budworm host species basal area (m^2/ha)
Total_BA	Total basal area per plot (m^2/ha)
BF_density	Balsam fir (stems/ha)
BS_density	Black spruce (stems/ha)
WS_density	White spruce (stems/ha)
HW_density	Hardwood (stems/ha)
Total_density	Total (stems/ha)
GF_May	Average May gap fraction (GF)
GF_July	Average July GF
GF_October	Average October GF
GFC_MO	Gap fraction change: GF May - GF October
GFC_JO	Gap fraction change: GF July - GF October
GFC_MJ	Gap fraction change: GF May - GF July
GFR_MO	Gap fraction ratio: GF May / GF October
GFR_JO	Gap fraction ratio: GF May / GF October
GFR_MJ	Gap fraction ratio: GF May / GF October

Table 2.2: Summary of mean tree characteristics and measured defoliation for 75 sample plots near Amqui and Causapscal, Quebec.

Sample plot characteristics	Mean	Standard Deviation	Minimum	Maximum
Density (stems/ha)	2030	738	900	4475
DBH[a] (cm)	13.9	6.4	3.1*	60.2*
Height (m)	14.7	4.9	1.4*	26.1*
Basal area (m^2/ha)	44.0	4.7	29.3	54.0
Balsam fir (% basal area)	64	25	2	99
Black spruce (% basal area)	19	25	0	90
White spruce (% basal area)	9	18	0	93
Hardwoods[b] (% basal area)	6	6	0	25
Other softwoods[b] (% basal area)	2	5	0	17
Annual branch defoliation 2015	52	34	0	99
Annual branch defoliation 2016	35	26	1	98
Annual ocular defoliation 2015	48	32	4	93
Annual ocular defoliation 2016	28	24	4	40

* Represents individual tree values observed across sample plots.
[a] Abbreviations: DBH = diameter at breast height (1.3m above ground).
[b] Hardwood species = balsam popular, mountain ash, trembling aspen, willow sp., trembling aspen, white birch, yellow birch, red maple, mountain maple, striped maple; Other softwoods species = eastern white cedar, eastern white pine, eastern larch.

Table 2.3: Bias, mean absolute bias (MAB), and root mean square error (RMSE) of predictions of current annual defoliation (%) for a random one-third of plots (44) withheld for model validation, using logistic Generalized Linear Model (GLM) and Random Forests (RF) models. Variable names are defined in Table 2.1.

Variables	Bias (%)		MAB (%)		RMSE (%)	
	GLM	RF	GLM	RF	GLM	RF
A. **Models including Spray**						
1. Spray	2.9	1.5	18.1	17.9	22.0	21.8
2. Spray + GFC_MO	2.8	–0.6	16.0	16.2	19.8	20.0
3. Spray + BF_BA%	1.3	0.9	17.1	16.3	20.5	19.7
4. Spray + GFC_MO + BF_BA%	**1.1**	**–0.1**	**15.5**	**15.1**	**18.8**	**18.2**
B. **Models excluding Spray**						
5. GFC_MO	1.2	–4.9	18.6	**18.0**	22.4	23.2
6. BF_BA%	–0.8	–0.8	22.4	25.3	27.2	31.2
7. GF_October	1.0	–0.6	20.3	21.9	24.5	27.2
8. BF_BA% + GF_October	**–0.5**	–0.9	19.9	**18.0**	24.5	22.0
9. GFC_MO + GF_October	1.2	–2.5	18.5	19.4	**22.3**	23.7
10. GFC_MO + BF_BA%	**–0.5**	**–0.2**	**18.0**	19.4	22.4	23.3
11. GFC_MO + BF_BA% + GF_October	**–0.5**	–1.6	18.1	18.2	22.5	**21.1**

[1] Model construction consisted of combinations of the top three variables from GBM relative influence analyses, for models A. including, and B. excluding the Spray variable, in order to assess models based on stand and photo-based variables only.

[2] Bold font indicates the lowest bias, MAB, and RMSE.

Table 2.4: Two-sample Kolmogorov-Smirnov (KS) test evaluating goodness-of-fit of model predicted defoliation against measured annual branch and ocular defoliation for 44 sample plots retained for validation. The test statistic D reports the maximum absolute difference between shape distributions calculated from cumulative distribution functions.

	Measured ocular defoliation	GLM excluding Spray	RF excluding Spray	GLM including Spray	RF including Spray
Measured branch defoliation	0.14 (0.81)	0.23 (0.21)	0.23 (0.21)	0.18 (0.47)	0.23 (0.21)
Measured ocular defoliation	–	0.30 (0.04)	0.32 (0.02)	0.21 (0.32)	0.25 (0.13)
GLM excluding Spray	–	–	0.14 (0.81)	0.27 (0.08)	0.21 (0.32)
RF excluding Spray	–	–	–	0.25 (0.13)	0.21 (0.32)
GLM including Spray	–	–	–	–	0.18 (0.47)
RF including Spray	–	–	–	–	–

***** Values not inside parentheses are the test statistic D and values inside parentheses are the corresponding p-values.

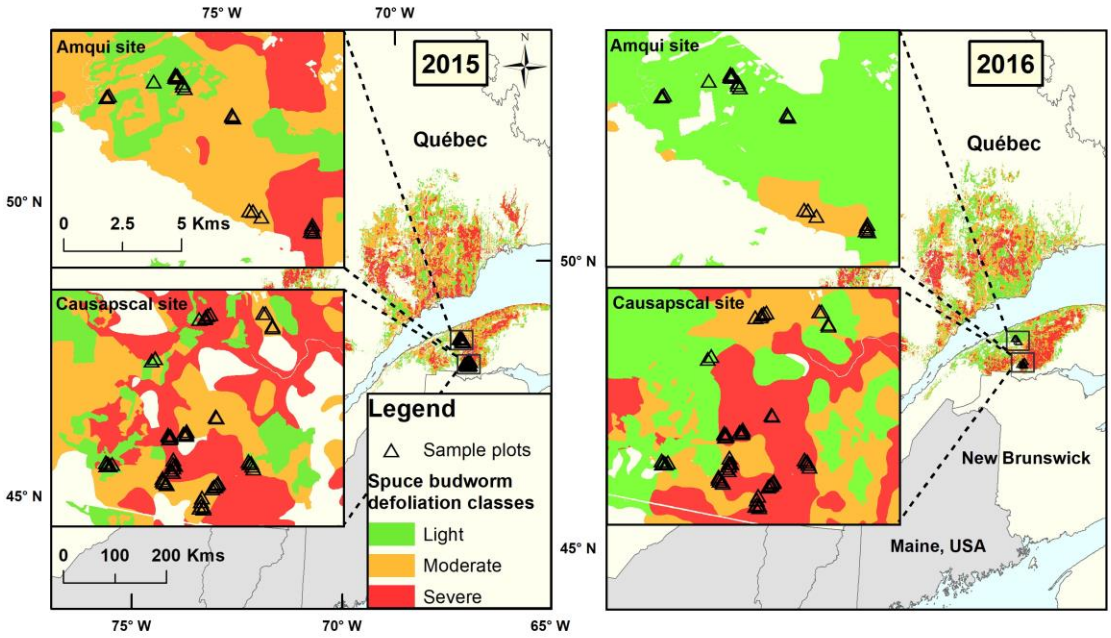

Figure 2.1: Map of 75 sample plot locations near Amqui and Causapscal, Quebec overlaid on aerial spruce budworm defoliation survey results for 2015 and 2016 (QMFFP, 2016).

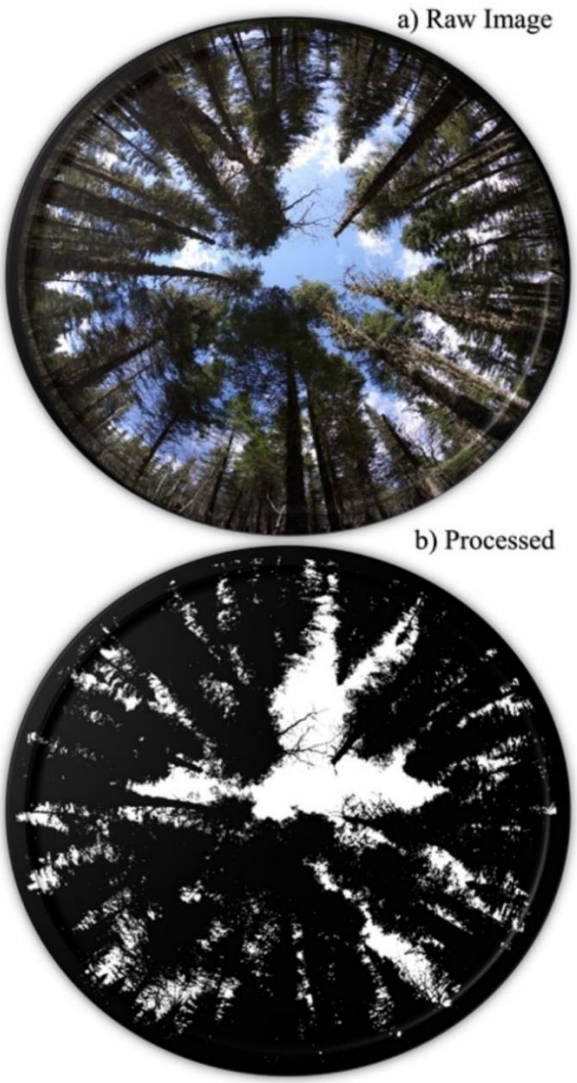

Figure 2.2: Examples of a) a canopy image from a hemispherical camera collected at one of four camera locations per plot and b) the same image following processing using ImageJ software and the “Minimum” thresholding algorithm to classify each pixel as vegetation (black) or sky (white).

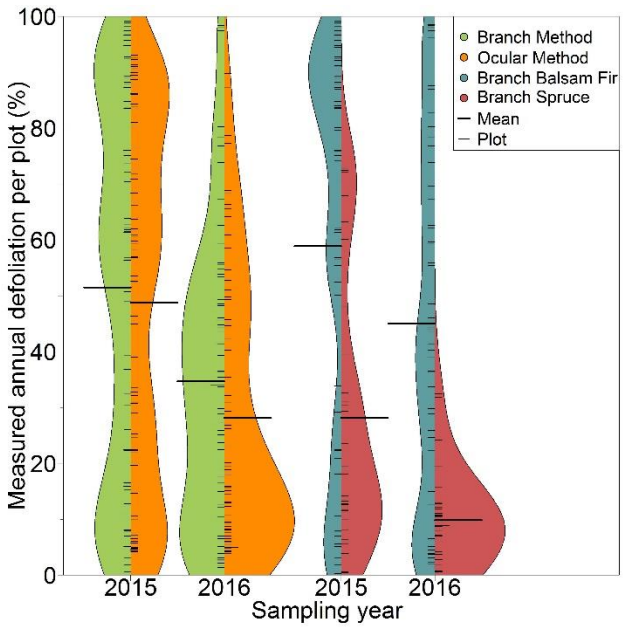

Figure 2.3: Beanplot summary of the distributions of measured current annual branch defoliation (green) and ocular defoliation (orange) among plots each year and annual branch defoliation per species among plots each year for balsam fir (blue) and black and white spruce (red) for 75 sample plots. Coloured polygon shapes indicate the overall density trace of plot defoliation measurements.

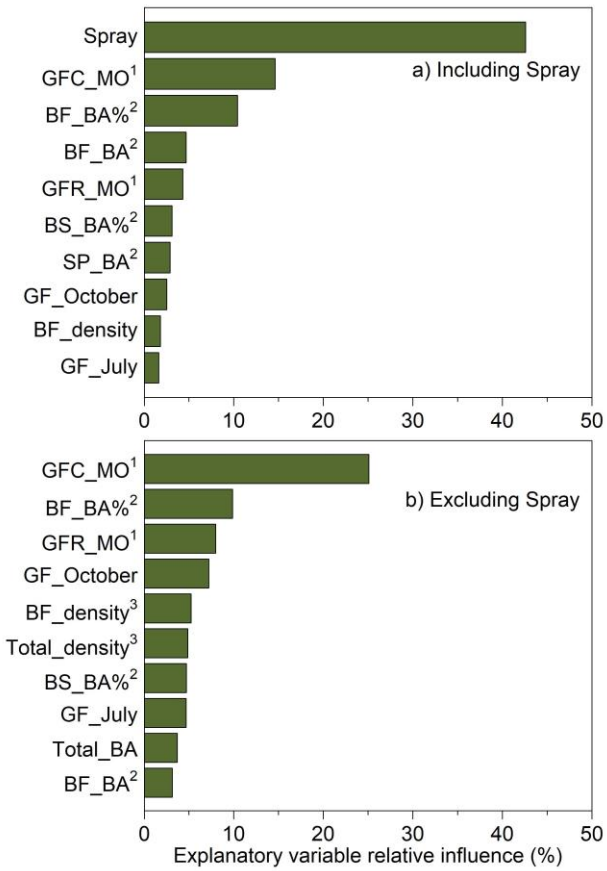

Figure 2.4: Relative influence (variable importance) for the top 10 out of 30 explanatory variables using the combined year dataset (n = 140) to predict annual branch defoliation per plot (%) for a) including, and b) excluding the Spray variable. Variables with the same superscript number were multicollinear at a correlation coefficient threshold of $r \geq 0.7$. Variable names are defined in Table 2.1.

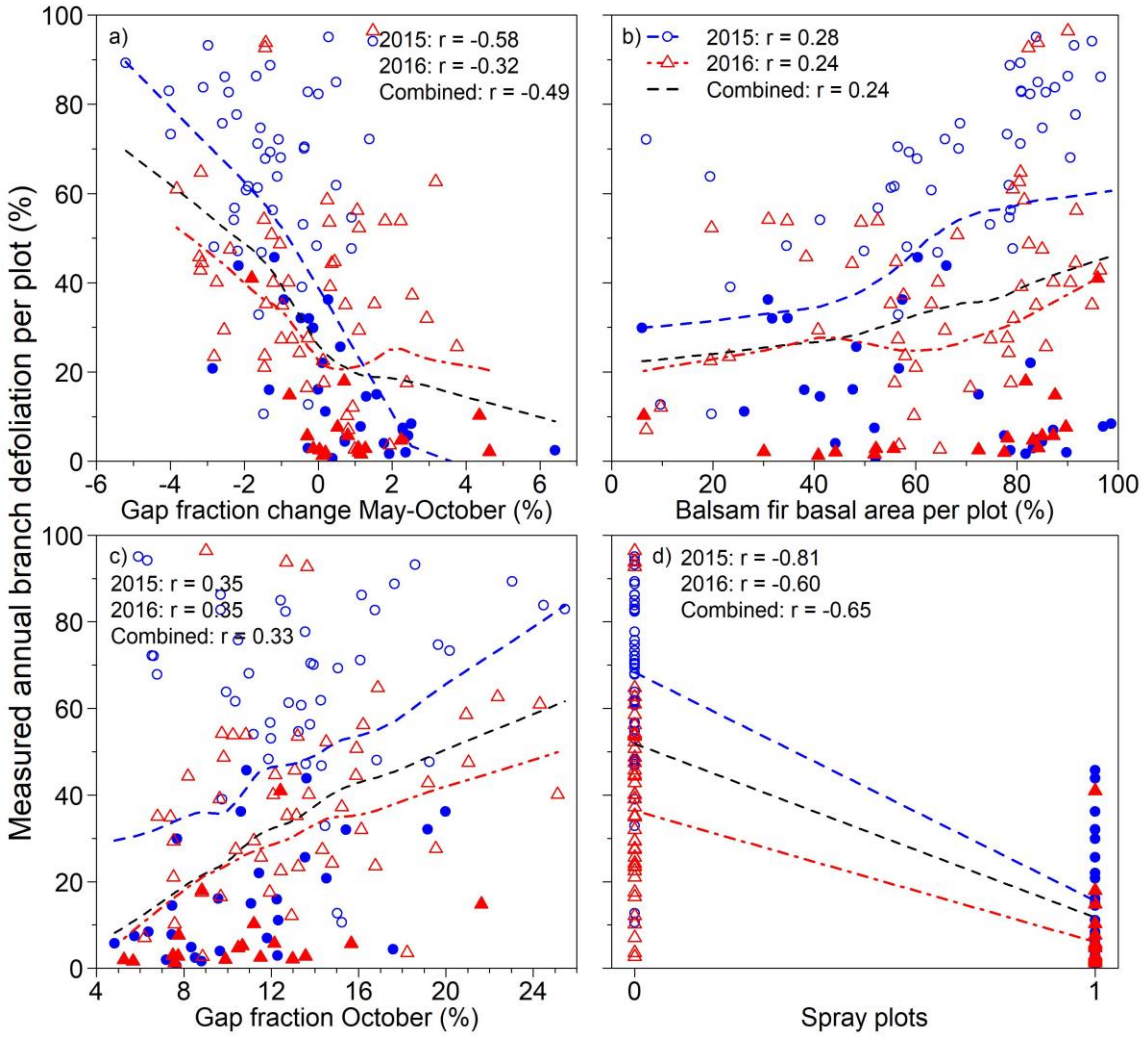

Figure 2.5: Relationships between mean annual branch defoliation per plot in 2015 and 2016 and a) gap fraction change May-October, b) balsam fir basal area %, c) gap fraction October and d) plots sprayed with insecticide (1) and not sprayed (0). LOWESS regression lines are fit per year, and for combined data, and solid coloured symbols represent sample plots affected by insecticide spraying.

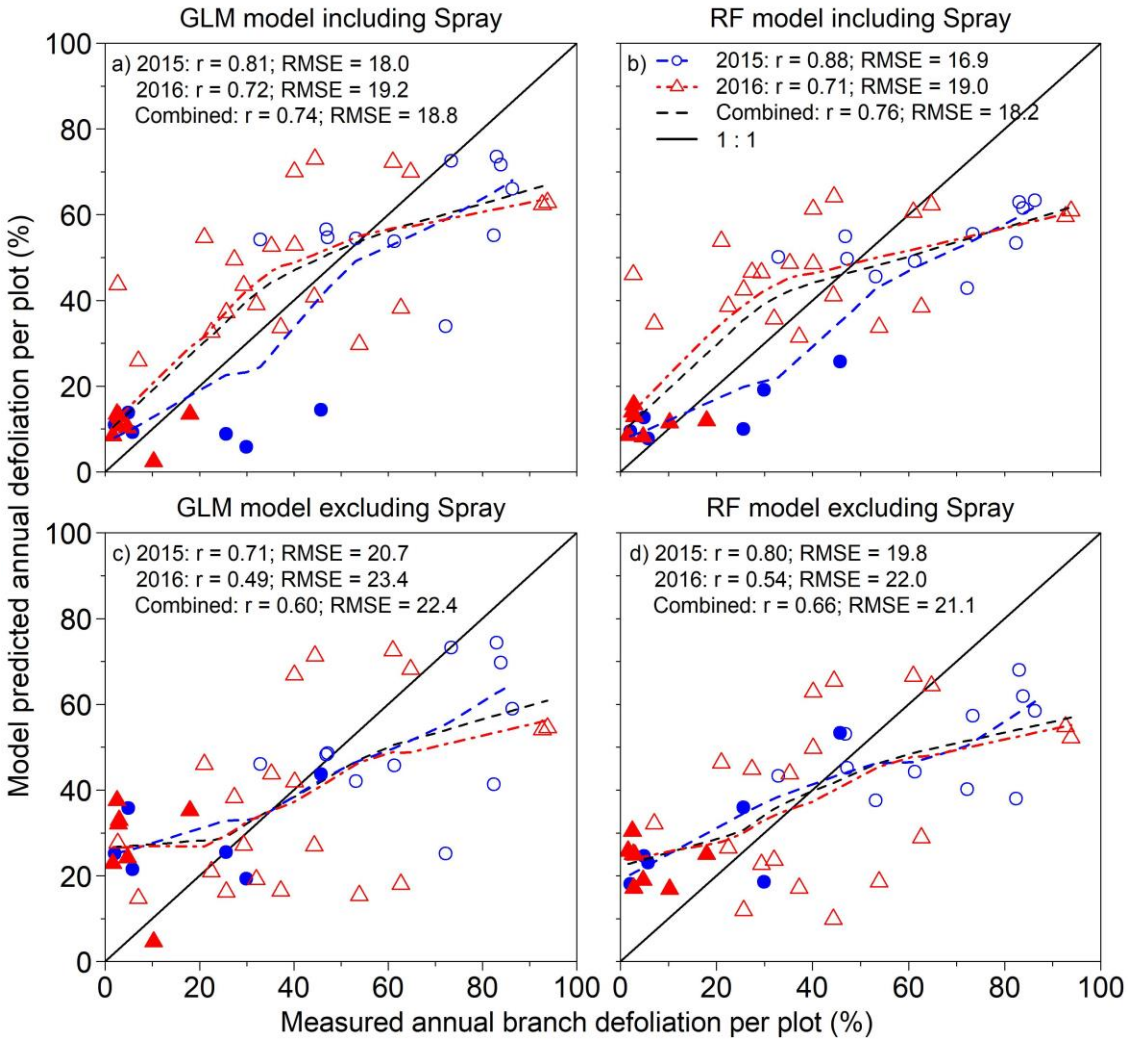

Figure 2.6: Annual defoliation predicted using four models plotted against measured annual branch defoliation for 44 retained validation plots, for 2015, 2016, and combined data: a) GLM and b) Random Forests (RF) models using Spray, GFC_MO, and BF_BA% explanatory variables; c) GLM model using GFC_MO and BF_BA%; and d) RF model using GFC_MO, BF_BA%, and GF_October. LOWESS regression lines are fit per year and for combined data, and solid coloured symbols represent sample plots affected by insecticide spraying.

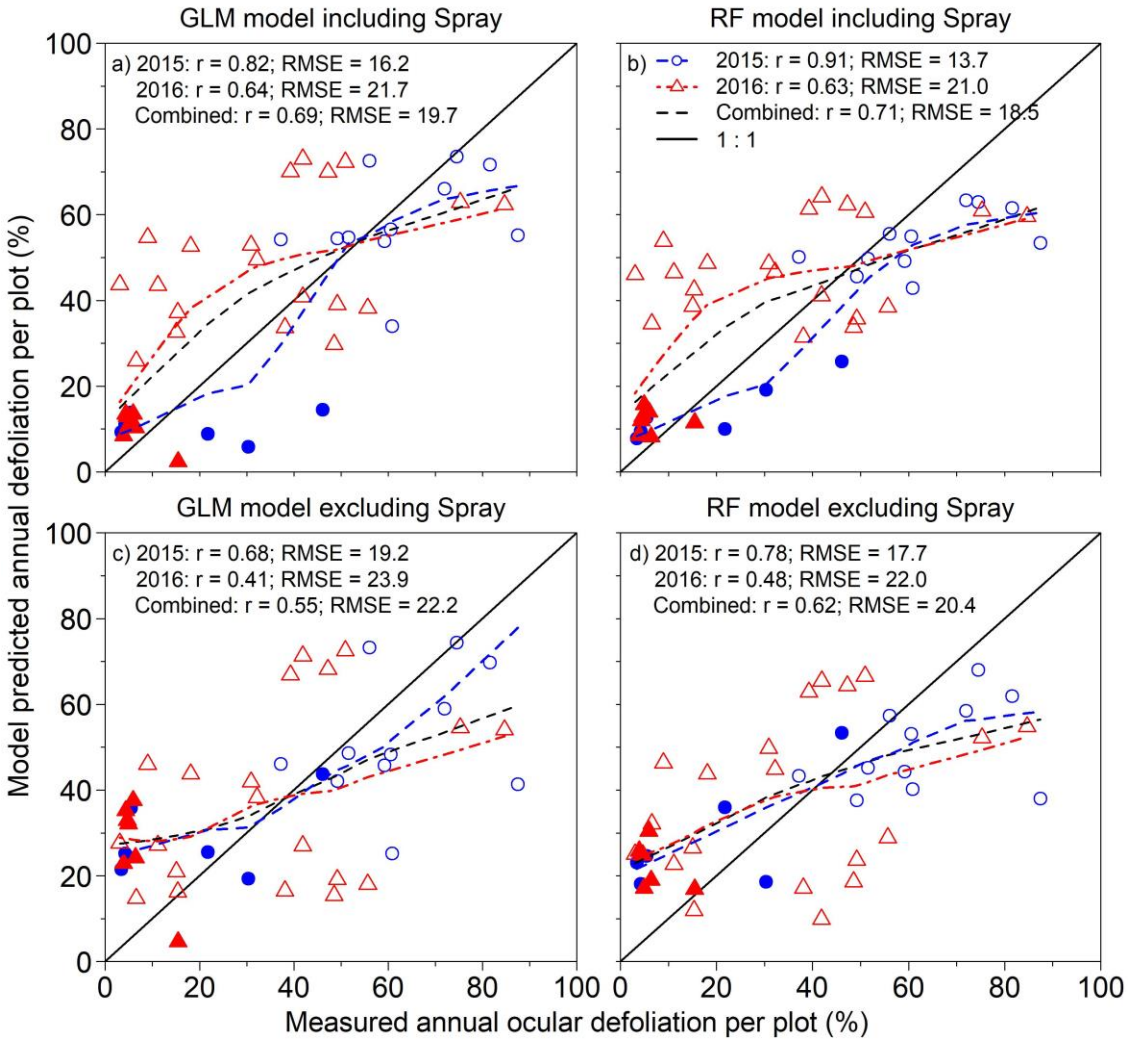

Figure 2.7: Annual defoliation predicted using four models plotted against measured annual ocular defoliation for 44 retained validation plots, for 2015, 2016, and combined data: a) GLM and b) Random Forests (RF) models using Spray, GFC_MO, and BF_BA% explanatory variables; c) GLM model using GFC_MO and BF_BA%; and d) RF model using GFC_MO, BF_BA%, and GF_October. LOWESS regression lines are fit per year and for combined data, and solid coloured symbols represent sample plots affected by insecticide spraying.

CHAPTER 3: POTENTIAL OF SATELLITE HYPERSPECTRAL IMAGERY FOR DETECTING ANNUAL SPRUCE BUDWORM DEFOLIATION

Submitted to the journal Remote Sensing of Environment on February 6th, 2020

Authors: S.D. Donovan, D.A., MacLean, Y. Zhang, M.B. Lavigne, J.A. Kershaw

3.1. Abstract

During spruce budworm (SBW; *Choristoneura fumiferana* (Clem.)) outbreaks, defoliation causes severe tree damage and mortality to spruce-fir (*Picea spp.-Abies balsamea* (L.) Mill.) forests causing long-term impacts on ecological processes and species and age-class distributions. Current methods used for annual defoliation surveys are visual observations by professionals from small aircraft, which are subjective, spatially variable, limited to a short detection period, and with low detection accuracies (approximately 35% to 40%). Remote sensing studies have mainly focused on using multispectral images for detecting cumulative, multi-year SBW defoliation, reaching accuracies of 50% to 70%. However, detecting annual defoliation is more difficult but the information is more important for informing SBW management. Only one study has used satellite hyperspectral imagery to detect annual SBW defoliation, reaching accuracies of 63–78%. In this paper, a reliable method for classifying three classes (≤ 30%, 30–70%, and ≥ 70%) of annual SBW defoliation is achieved using change detection of vegetation indices (VIs) derived from satellite hyperspectral imagery (EO-1 Hyperion, acquired before and after annual defoliation) and Random Forest (RF) and Support Vector Machine (SVM) classifiers. Accurate defoliation measurements by branch sampling SBW-host trees for 68 field plots in Québec, Canada, were used for validating classifiers. The top five VIs for detecting annual defoliation, based on RF Total Variable Importance Score (TVIS) and Spearman's rank correlations (r), were: Plant Senescence Reflectance Index (TVIS = 121; r = -0.64), Moisture Stress Index (TVIS = 75, r = -0.53), Enhanced Vegetation Index (TVIS = 58; r = 0.43), Modified Simple Ratio (TVIS = 58; r = 0.37),

and Normalized Difference Water Index (TVIS = 72; r = 0.32). Accuracies of the three defoliation classes (light, moderate, and severe) are 89–97%, 83–97%, and 83–100%, respectively, reaching an overall accuracy of 88–91%. Our method proved that using hyperspectral satellite data can detect annual SBW defoliation and was superior to aerial surveys. Also, our results provide objective pixel-level within-stand defoliation, and such high-resolution spatial data are in operational demand for use in aerial bioinsecticide spray programs, monitoring SBW levels, and projecting outbreak impacts.

3.2. Introduction

Spruce (*Picea spp.*)-balsam fir (*Abies balsamea* (L.) Mill.) forests in North America provide important ecological and economic values, such as carbon storage and timber resources (Chang et al., 2012). Spruce-fir is the most abundant forest type in Canada, comprising 59% of 348 million hectares (ha) of forests (Canadian National Forest Inventory, 2013). Spruce-fir forests are vulnerable to spruce budworm (SBW; *Choristoneura fumiferana* (Clem.)), a native insect that defoliated 11, 25, and 57 million ha at the peak of the 1910s, 1940s, and 1970s outbreaks (Kettela, 1983). Severe SBW defoliation results in up to 90% reduction of tree growth (Erdle and MacLean, 1999), and mortality averages 85% in mature balsam fir stands (MacLean, 1980). SBW-caused mortality in Quebec reached 238 million m^3 during the 1970s (Coulombe Commission (Commission d'étude sur la gestion de la forêt publique québécoise) 2004) resulting in commercial value losses estimated at $12.5 billion (Lévesque et al., 2010). Forecasts for the province of New Brunswick estimate present-value losses of $3.3 and $4.7 billion for future uncontrolled moderate and severe outbreaks scenarios lasting 30 years (Chang et al., 2012). However, if strategic spray programs using bioinsecticides (best method for reducing SBW populations and keeping trees alive) are deployed, timber harvest reductions can be minimized by 30–50% (Hennigar et al., 2013). Monitoring SBW outbreaks and estimating the economic and environmental impacts relies on collecting accurate annual defoliation data.

Many jurisdictions use annual aerial surveys by observers in small aircraft as the operational method to estimate defoliation over forests during SBW outbreaks. Surveys

are limited to a 2–3 week detection period after SBW completes feeding primarily on the newest foliage age-class each year. Feeding causes partially damaged or dead foliage to turn reddish-brown, and observers delineate areas of similar color change into broad defoliation classes (typically nil 0–10%, light 11–30%, moderate 31–70%, and severe 71–100% removal of current-year foliage) (MacLean and MacKinnon, 1996). Defoliation data are used in planning aerial bioinsecticide spray programs, monitoring outbreak extent and SBW populations, and as an input for defoliation-based stand growth models (e.g., Chen et al., 2018) and the SBW Decision Support System (MacLean et al., 2001) for quantifying timber supply and economic impacts. Although aerial surveys can provide reasonable accuracy, they are subjective, vulnerable to observer bias, the red-stage coloration can be lost during rain and wind, and are limited to a short detection period (MacLean and MacKinnon, 1996). The main issues are an inability to discriminate low levels of defoliation and underestimation of scattered severe defoliation (MacLean and MacKinnon, 1996).

Remote sensing of SBW defoliation based on satellite imagery and vegetation spectral information is a desirable option to assist or replace aerial surveys. Benefits of modern sensors include 1) the high spatial resolution of Worldview-3 (0.31 meter (m) pixel size) permits within-stand and tree-level detection (Lausch et al., 2016); 2) Sentinel-2 twin satellites allow global coverage and near-continuous temporal images (5-day imaging period), improving monitoring capabilities (Claverie et al., 2018); and 3) hyperspectral sensors such as Earth Observing-1 (EO-1) Hyperion have many narrow wavelength bands (242 bands) with continuous 10 nm bandwidths from 400–2500 nanometers (nm) (Datt et al., 2003). Hyperspectral sensors enable detection of subtle

spectral changes related to biophysical vegetation characteristics, such as leaf area and chlorophyll content, that are affected by defoliation, which would be obscured using broadband multispectral sensors (Hall et al., 2016; Oumar et al., 2013).

Remote sensing has had limited application in operational forest health monitoring because of high costs and unavailability of quality images, lack of in-house personnel for processing and analyzing data, and limited availability of ground verification datasets (Senf et al., 2017). For detecting SBW defoliation, image cloud cover, and coarse temporal resolutions, relative to the short period required for detection are limiting factors (Rahimzadeh-Bajgiran et al., 2018). The use of multi-image change detection analysis, which attempts to isolate a specific spectral response, is an advantage in monitoring versus using a single image (Hall et al., 2016). Change detection methods include: bi-image differencing of raw image digital values or calculated vegetation indices (VIs); classifying each image separately and defining the resulting class change; using spectral mixture analysis to extract proportional change of different objects per pixel; and multi-image time series analysis for separating target reflectance signals from seasonal reflectance changes (Hall et al., 2016). The high spectral resolution of hyperspectral sensors in combination with change detection methods could provide extended monitoring. However, images should still be acquired in a manner that maximizes reflectance change specific to annual defoliation, 87% of which occurs during a short period of feeding by sixth-instar larvae (Miller, 1977).

Many remote sensing classification algorithms are available, but the Random Forest (RF) and Support Vector Machine (SVM) machine-learning algorithms have been demonstrated to produce good results (Maxwell et al., 2018; Noi and Kappas, 2018). RF

and SVM classifiers have been applied for remote sensing insect defoliation (Adelabu et al., 2014a; Hawryło et al., 2018), mapping bark beetle-induced tree mortality (Fassnacht et al., 2014), and RF was used for detecting annual SBW defoliation (Rahimzadeh-Bajgiran et al., 2018). Both classifiers can manage high dimensional hyperspectral data, have low computation times, and handle complex multi-class problems (Ballanti et al., 2016).

Previous studies using satellite remote sensing to assess SBW defoliation have mainly detected cumulative, multi-year defoliation rather than the current-year-only annual defoliation. However, annual defoliation is more difficult to detect, and the information is needed for SBW management and currently achieved by visual aerial surveys. For example, Franklin et al. (2008) used multi-temporal Landsat-5 TM (Thematic Mapper) and single date SPOT-4 HRVIR (High Resolution Visible and Infrared) imagery and found correlations of r = 0.81 and 0.88 between three cumulative SBW defoliation classes and VIs. Goodbody et al. (2018) used digital aerial photogrammetric data to assess percent cumulative SBW defoliation, with spectral metrics explaining 79% of the variation. Rahimzadeh-Bajgiran et al. (2018) used Landsat-5 TM imagery to estimate annual SBW defoliation (in comparison with aerial survey data) and achieved accuracies of 52–77% for four defoliation classes.

Hyperspectral narrow-band VIs have advantages for detecting insect defoliation (Pontius et al., 2008). Three VIs derived from EO-1 Hyperion imagery were used to predict bronze bug (*Thaumastocoris peregrinus* Carpintero and Dellapé) damage with an $R^2 = 0.74$ (Oumar et al., 2013). Vegetation moisture indices calculated from EO-1 Hyperion imagery were significantly related ($R^2 = 0.51$, $p = 0.0001$) to mountain pine

beetle (*Dendroctonus ponderosae* Hopkins) damage (White et al., 2007). Huang (2015) tested EO-1 Hyperion imagery to detect annual SBW defoliation and achieved 15% higher accuracy using Hyperion hyperspectral imagery than with EO-1 multispectral Advanced Land Imager imagery. Change detection of narrow-band VIs for mapping annual defoliation defined by light and severe classes resulted in overall accuracies of 63–78%; however, only aerial survey data were used for training and validation (Huang, 2015). Although promising, accurate ground truth data such as plot-measured defoliation are needed to verify methods (Rahimzadeh-Bajgiran et al., 2018).

In this study, we tested change detection of hyperspectral images (EO-1 Hyperion) for classifying annual SBW defoliation during an ongoing outbreak in Québec, Canada. Images were acquired before and after peak defoliation in 2016 for two study areas, where accurate defoliation measurements by branch sampling SBW-host trees were collected for 68 field plots (over 1300 branches sampled for defoliation). Specific objectives were to: 1) use RF variable importance metrics to evaluate change detection of 14 narrow-band VIs calculated from hyperspectral imagery to detect three classes of annual SBW defoliation; 2) assess defoliation classification accuracies of semi-supervised machine-learning RF and SVM classifiers validated using branch defoliation measured in 68 field plots; and 3) apply the best performing RF and SVM classifiers to map three defoliation classes for 14,000 ha of forest, and compare results with aerial survey maps.

3.3. Methods

3.3.1. Study area

The most recent SBW outbreak in Canada started in Québec in 2004, and by 2019, 9.6 million ha of forests have been defoliated (QMFFP, 2019). Our study area is in central Gaspé Peninsula in Québec, part of Great Lakes-St. Lawrence Forest Region, section L6 Témiscouata-Restigouche (Rowe, 1972), SBW defoliation was first detected in the study area in 2012. Forests are comprised mainly of balsam fir and white birch (*Betula papyrifera* Marsh.) (Bélanger et al., 1992). SBW host species balsam fir and white spruce (*Picea glauca* (Moench) Voss) are abundant at low elevations and black spruce (*Picea mariana* (Mill.) B.S.P.) is common in poorly drained areas. Other common non-host species include balsam poplar (*Populus balsamifera* L.), trembling aspen (*Populus tremuloides* Michx.), red maple (*Acer rubrum* L.), sugar maple (*Acer saccharum* Marsh.), yellow birch (*Betula alleghaniensis* Britton), eastern white cedar (*Thuja occidentalis* L.), eastern white pine (*Pinus strobus* L.), and eastern larch (*Larix laricina* (Du Roi) K.Koch) (Rowe, 1972).

The landscape has a rolling topography with rivers creating narrow valleys and alluvial flats (Rowe, 1972). Elevations range from 275 to 575 m, mean annual temperatures between 0°C and 2.5°C and growing degree days of 150 to 160 days (Archambault et al., 1998).

3.3.2. Annual SBW defoliation field plot measurements and aerial surveys

A geographic overview of light, moderate, and severe defoliation from 2016 aerial surveys (QMFFP, 2016), along with EO-1 Hyperion image scene extents, study area

boundaries, and locations of 68 plots with field-measured defoliation, are shown in Figure 3.1. Québec aerial surveys define three defoliation classes: light – slight loss of foliage in the upper third of the crown of some trees; moderate – loss of foliage in the upper half of the crown of the majority of trees; and severe – loss of foliage across the crown length of most trees (QMFFP, 2016). For comparison and analysis, our plot-level branch defoliation data were converted to align with the three classes of aerial survey defoliation (light <30%, moderate 30–70%, and severe >70%).

In the early stages of the SBW outbreak, 99 circular 0.04 ha research field plots were established in 2014 attempting to collect a range (0–100% balanced across 10% classes) of annual defoliation. A subset of 68 plots were selected for this study due to satellite hyperspectral images only being available in 2016 and covering a portion of field plots for the two study areas. The two study areas included 20 plots northeast of Amqui and 48 plots southwest of Causapscal (Fig. 3.1) and plot species compositions were dominated by SBW hosts balsam fir, black spruce, and white spruce, with percent mean basal areas per hectare of 64%, 19%, and 9%, respectively. For measuring plot-level annual defoliation, one mid-crown branch was cut using pole pruners from a minimum of 15 host trees (≥ 10 cm at breast height) per species per plot, based on species and defoliation-level specific sample sizes required to estimate mean defoliation with 90% confidence and ± 10% error (MacLean and MacKinnon, 1998). A total of 1338 branches were measured using the shoot count method (Fettes, 1950), rating 25 individual shoots by one of seven defoliation classes (0, 1–20, 21–40, 41–60, 61–80, 81–99, or 100%) and averaged per branch to determine tree defoliation. Plot mean annual branch defoliation was calculated, weighted by tree basal area of all branch sampled trees per plot. More

detailed descriptions of the plot network, tree attributes, and tree defoliation measurements were presented in Donovan et al. (2018).

3.3.3. Hyperspectral image acquisition and processing

Pre-defoliation image acquisitions were timed to ensure completion of as much current-year foliage growth as possible but before feeding by sixth-instar larvae. Post-defoliation image acquisitions were timed based on the completion of SBW feeding, enabling foliage reduction and dead or damaged foliage to turn reddish-brown. We used BioSIM software (version 11; Régnière et al., 2017) applying local weather station data, growing degree-day, and geographic data inputs to model SBW phenology, and estimated that peak defoliation (sixth instar stage) occurred on June 28. Cloud cover conditions, in combination with the 16-day imaging period for the EO-1 orbit (Eigemeier et al., 2012), influenced the availability of quality images. Four cloud-free images were acquired in 2016 on June 18 and 26 for pre-defoliation and September 5 and 10 for post-defoliation, for the Causapscal and Amqui study areas, respectively.

Hyperspectral images were provided via data-acquisition-request from the National Aeronautics Space Administration (NASA) in level 1R file format. Level 1R imagery is radiometrically corrected to at-sensor radiance from steps including spectral calibration, smear and echo corrections, bad pixel masking, and alignment of Visual Near Infrared (VNIR) and Shortwave Infrared (SWIR) bands (Pearlman et al., 2003). EO-1 Hyperion image scene dimensions were 7.5 km wide and 100 km long. Only forested areas near our field plot locations were selected, resulting in spatial extents of 7270 ha and 6838 ha for the Amqui and Causapacal areas (Figure 3.1). To produce surface reflectance images,

preprocessing steps included band selection, abnormal pixel correction, vertical stripe removal, smile correction, atmospheric correction, and geometric correction (Datt et al., 2003; Goodenough et al., 2003) and was done using the Environment for Visualizing Images Interactive Data Language (ENVI/IDL; version 5.5) software.

Visual inspection identified 44 non-calibrated bands, two bands overlapping between the Visual Near Infrared (VNIR) and Shortwave Infrared (SWIR) detectors, and 32 bands of low reflectance sensitivity (noisy) due to atmospheric water vapour and these were excluded from further analyses. As a result, 164 bands per image were available for processing. Abnormal pixels with lower digital numbers compared to their neighbours were corrected by averaging the immediate left and right adjacent pixels (Han et al., 2002). Due to detector malfunction or poor calibration, some bands had vertical along-track striping issues and were corrected using the "Spear Vertical Stripe Removal" tool. Across-track wavelength shifting "Smile" from the wavelength centre due to change in dispersion angle and field position occurred for all images (Goodenough et al., 2003), and corrections were completed using the "Cross-Track Illumination Correction" (San and Süzen, 2011). Atmospheric correction producing at-surface reflectance was completed with the Fast Line-of-sight Atmospheric Analysis of Spectral Hypercubes (FLAASH) module (Datt et al., 2003). Geometric corrections were completed using the "Image to Map Registration" process and 30 cm resolution 2015 aerial orthophotos as reference provided by the Québec Ministère des Forêts de la Faune et des Parcs. Images were projected to datum WGS 84 UTM 19N coordinate system, and 20 ground control points (e.g., mainly road junctions) were used to align each image to orthophotos. Bilinear resampling of after defoliation images resized pixels to the same resolution as the before

defoliation images. Geometric corrections resulted in overall pixel root mean square errors (RMSEs) of 5.0 to 5.8 m.

Before calculating the spectral change of VIs caused by defoliation, pixel masks were applied to hyperspectral images using the Normalized Difference Vegetation Index (NDVI; Tucker, 1979). The goal was to avoid false-positive classifications of defoliation by separating forested from non-forested pixels (Liu et al., 2017a). An NDVI threshold of < 0.7 was selected for removing pixels dominated by roads, water bodies, agriculture fields, and silviculture activity.

3.3.4. Change detection of narrow-band vegetation indices

We investigated the spectral response of 14 narrow-band VIs, representing vegetation greenness, canopy water content, and light use efficiency characteristics, to annual SBW defoliation (Table 3.1). VIs within the vegetation greenness category provide measures of overall quantity and vigor of foliage, canopy water content measures the amount of foliage water, and light use efficiency measures vegetation's photosynthesis ability.

For calculating narrow-band VIs using hyperspectral data, selecting a subset of sensitive bands using dimensionality reduction methods is shown to perform better than techniques using all original bands (Liu et al., 2017b). We selected VI bands by reviewing relevant literature and referencing a database of remote sensing indices (Index Database; Henrich et al., 2012). For each VI, the hyperspectral band closest to the wavelength centre reported in the literature/database was selected (Table 3.1). All narrow-band VI calculations were completed using the "raster" package (Hijmans, 2019)

and R statistical software (R Core Team, 2019).

The change detection procedure described by De Beurs and Townsend (2008) was used, producing a relative percent change of each VI using the before- and after-defoliation images. Raster calculations used R software and the De Beurs and Townsend (2008) equation:

$$VI\ change\ (\%) = \frac{VI_{before\ defoliation} - VI_{after\ defoliation}}{VI_{before\ defoliation}} \quad (1)$$

where VI refers to pixel values for the before defoliation and after defoliation images.

3.3.5. Vegetation index change extraction for calibration and validation defoliation plot data

Before identifying the VIs most sensitive to annual defoliation, extraction of VI changes related to field plot locations was required. Examination of the 68 measured defoliation field plots revealed an imbalance across light, moderate, and severe defoliation classes. Imbalanced datasets can be problematic, causing majority class bias and minority class possibly treated as noise during classification model training (Haixiang et al., 2017). We implemented a semi-supervised classification design whereby the 68 field plots were retained for classifier validation, and a set of training plots was created within spatial proximity of each of the 68 validation plots (Li and Plaza, 2016). This method assumed that each training plot was assigned defoliation that was the same as the adjacent actual validation plot. Furthermore, creating a larger training plot dataset captured a broader range of VI change conditions for each defoliation class, improving classifier training. A 30 X 30 m grid of 400 m^2 circular plots was created to select training plots up to a maximum distance of 50 m from each of the 68 validation plot

locations, resulting in a total of 824 training plots. Training and validation plots had different shapes, locations, and areas compared to image pixels, so a mean area-weighted extraction method averaged pixel VI changes based on georeferenced intersections between plots and image pixels.

3.3.6. Vegetation index importance and selection related to annual defoliation

Selection of VIs most sensitive to annual SBW defoliation was completed using Random Forest (RF; Breiman, 2001) and a method by Han et al. (2016). Both RF default outputs Mean Decrease in Accuracy (MDA) and Mean Decrease in Gini (MDG) were combined into a Total Variable Importance Score index (TVIS). MDA utilizes prediction error of random Out-Of-Bag samples (OOB; random testing data) from each decision tree to compute mean variable importance (Ishak, 2016). MDG is the average of a variable's decrease in node impurity across all trees (Han et al., 2016). Model setup included three annual defoliation classes as the response for all training and validation plots, all 14 VIs as explanatory variables, and setting input parameters ntree = 500 (number of decision trees) and mtry = 3 (random variables selected at each tree node). In addition to RF-based VI importance analysis, monotonic relationships between defoliation and VI change and collinearity between VIs were considered (Dormann et al., 2013), using Spearman's rank correlation thresholds of $\geq \pm 0.3$ and $\leq \pm 0.7$, respectively. A forward stepwise variable selection was implemented to evaluate the accuracy improvement of adding additional VIs to each RF and SVM classifier.

3.3.7. Classifying defoliation using Random Forest and Support Vector Machine classifiers

RF and SVM classifiers were selected for classifying annual SBW defoliation based on good performance dealing with overfitting and handling limited training data (Ballanti et al., 2016; Noi and Kappas, 2018). A general rule in remote sensing with machine learning classifiers is to evaluate accuracy using separate validation data not used in classifier training (Maxwell et al., 2018). We stratified our dataset by retaining the original 68 measured defoliation field plots as our validation dataset and using all 824 created training plots for classifier training.

The RF classifier uses many decision trees to vote a majority final classification (Ballanti et al., 2016). RF models related three annual SBW defoliation classes to VI change and five models (Table 3.2) were explored using variable selection methods described in Section 2.6 by sequentially adding the top VI based on importance ranking. The R software "randomForest" package (Liaw and Wiener, 2002) was used, with the default model parameters of ntree = 500 trees and mtry = $\sqrt{n}$, where *n* equals the number of predictor variables (Liaw and Wiener, 2002).

The SVM classifier separates defoliation classes in feature space by defining an optimal hyperplane (split) between classes based on support vectors (training data) (Noi and Kappas, 2018). Classification studies using SVM commonly report good performance selecting a Radial Basis Function kernel, which defines the hyperplane shape (Ballanti et al., 2016; Maxwell et al., 2018). The Radial Basis Function kernel requires setting two user-defined parameters: cost, which defines the size of misclassification allowed for non-separable training data, and gamma, which determines

the smoothing of the class-defining hyperplane (Ballanti et al., 2016). We performed model tuning for each of five SVM models, using the same VIs selected for the RF models (Table 3.2). To identify optimal cost and gamma parameters, the "tune" function within the R software "e1071" package (Meyer et al., 2019) enabled testing a range of cost (1–250) and gamma (0–2.5) parameters for the five SVM models (Noi and Kappas, 2018).

Evaluation of RF and SVM classifier accuracies was based on comparing classified and measured defoliation for the 68 validation plots. Comparisons between the five RF and five SVM models examined producer's accuracy per defoliation class along with overall accuracy and overall error. Preliminary results indicated that additional VI variables exceeding five did not significantly improve classification performance for either RF or SVM. For the top-performing RF and SVM classifiers, classification accuracies were computed and summarized into confusion matrices including producer's accuracy (compared to validation dataset), user's accuracy (accuracy expected on the ground) per defoliation class and overall accuracy with 95% confidence interval referenced to the validation dataset (Congalton, 1991). The Kappa index was not reported as Pontius and Millones (2011) recommended against it. Instead, classification agreement, commission error (when a feature is incorrectly included in the category being evaluated) and omission error (when a feature is left out of the category being evaluated; an error of omission in one category will be counted as an error in commission in another category) (Congalton, 1991) were graphed representing their respective counts per defoliation class for RF and SVM classifiers compared to the validation dataset. Pixel-level maps of annual SBW defoliation classes, generated using the best RF and

SVM classifiers, allowed visual comparison with Québec aerial survey data and validation plots.

3.4. Results

3.4.1. Classifier training and validation plot distributions per defoliation class

Percent mean annual branch defoliation of 68 field plots grouped by light, moderate, and severe defoliation classes shows the distribution of classifier validation plots (Figure 3.2a). Most validation plots were classified as light (33 plots; 49%) and moderate (29 plots; 43%), and only 6 plots (9%) as severe defoliation (Figure 3.2b). For training plots (400m^2 circular plots adjacent to and assigned the same defoliation value as each actual field plot), a total of 364 light, 292 moderate, and 168 severe defoliation plots were available (Figure 3.2b). Thus, a total of 824 and 68 plots were used for classifier training and validation, respectively.

3.4.2. Vegetation index importance related to annual SBW defoliation

The top VI selected for classifying defoliation was Plant Senescence Reflectance Index (PSRI; Merzlyak et al., 1999) with the second-best MDA, best MDG, and best TVIS results of 35.8, 85.1, and 120.9, respectively (Figure 3.3). The next best VI based on TVIS was Green Normalized Difference Vegetation Index (GNDVI; Gitelson et al., 1996) but weak correlation with defoliation (r = -0.19) supported GNDVI not being selected. The second VI selected was Moisture Stress Index (MSI; Hunt and Rock, 1989) with the third-best MDA, fourth-best MGA, and third-best TVIS (Figure 3.3). Following MSI, the next ranked VI by decreasing TVIS was Normalized Difference Moisture Index

(NDMI; Wilson and Sader, 2002), but was not selected due to collinearity (r = -0.98) with MSI. The third, fourth, and fifth VIs selected for classifying defoliation were Normalized Difference Water Index (NDWI; Gao, 1996), Modified Stress Ratio (MSR; Chen, 1996), and Enhanced Vegetation Index (EVI; Huete et al., 2002) (Figure 3.3). The five VIs selected by forward stepwise variable selection represented all three VI categories, with two (MSR and EVI) in vegetation greenness, two (NDWI and MSI) in canopy water content, and one (PSRI) in the light use efficiency category (Table 3.2).

Spearman's rank correlation between each of the five selected VIs and three annual defoliation classes showed that PSRI was the best VI with a decreasing relationship and r = -0.65 (Figure 3.4a). The second-best relationship was for MSI, having a decreasing relationship and r = -0.53 (Figure 3.4b), followed by EVI with an increasing relationship and r = 0.43 (Figure 3.4e), MSR with r = 0.37 (Figure 3.4d), and NDWI with r = 0.32 (Figure 3.4c).

3.4.3. Random Forest and Support Vector Machine classification of defoliation

Using forward stepwise selection, the top five VIs were consecutively added, creating five models each for both RF and SVM classifiers (Table 3.2). For the RF classifier, producer's accuracy for light and severe defoliation increased by 30% and 33% between RF-1 and RF-5, ranging from 67–97% and 67–100%, respectively (Figure 3.5). Producer's accuracy for the moderate defoliation class gradually increased from 55% to 86% from RF-1 to RF-4, then slightly decreased for RF-5 to 83% (Figure 3.5). Overall accuracy gradually increased from RF-1 to RF-5, ranging from 62% to 91%, while overall error declined from 38% to 9% (Figure 3.5). Producer's accuracy for the SVM

light defoliation class remained relatively constant from SVM-1 to SVM-4 at 84–88% versus 94% for SVM-5 (Figure 3.5). Producer's accuracy for the SVM severe defoliation class was highest at 100% for SVM-1 and dropped to 83% for each of SVM-2 to SVM-5 (Figure 3.5). Producer's accuracy for the SVM moderate defoliation class increased substantially from SVM-1 to SVM-5, ranging from 41% to 83% (Figure 3.5). Consistent with RF, SVM-1 to SVM-5 overall accuracy gradually increased from 77% to 88%, and overall error decreased from 23% to 12% with each additional VI added (Figure 3.5). We deemed models using all five VIs (RF-5 and SVM-5; hereafter termed "RF" and "SVM") were the best for classifying annual defoliation across all classes and were used for mapping defoliation.

Confusion matrices for RF and SVM classified defoliation and 2016 provincial aerial survey results were compared to the 68 validation plots (Table 3.3). RF performed slightly better with an overall accuracy of 91% versus 88% for SVM, and both were significantly better than aerial surveys at 38% (Table 3.3). Across the three defoliation classes, RF producer's and user's accuracies ranged from 83–100% (moderate defoliation lowest) and 86–96% (severe defoliation lowest), respectively (Table 3.3). SVM producer's and user's accuracies ranged from 83–94% (moderate defoliation lowest) and 83–89% (severe defoliation lowest) (Table 3.3). Finally, aerial survey producer's and user's accuracies ranged from 3–67% (moderate defoliation lowest) and 11–81% (severe defoliation lowest) (Table 3.3).

Out of the 68 validation plots, 62 plots were correctly classified by RF, and 60 correctly classified by SVM (Figure 3.6). The majority of misclassifications were between light and moderate defoliation classes (Figure 3.6). For RF, four of the six

omission errors were a result of moderate defoliation plots misclassified as light defoliation (Figure 3.6a). Similarly, for SVM, four of the eight omission errors occurred when moderate defoliation plots were classified as light (Figure 3.6b).

Pixel-based annual SBW defoliation classified by RF and SVM is compared with polygon-based aerial survey results for Amqui (a-c), and Causapscal (d-f) study areas in Figure 3.7. In the Amqui study area, 98% of 2016 provincial aerial survey results were classified as having light defoliation, within which 78–83% of RF and SVM pixels were also light defoliation. The remaining 2% of aerial survey results were classified having moderate defoliation, and 45–51% of RF and SVM pixels had the same moderate defoliation class (Table 3.4). In the Causapscal study area, aerial surveys classified 31%, 27%, and 42% of the area as light, moderate, and severe defoliation (Figure 3.7), within which 45–46%, 22–24%, and 48% of pixels were also classified as light, moderate, and severe defoliation, respectively (Table 3.4). RF and SVM classified images with 30m pixels provide higher resolution within-stand defoliation estimates, whereas aerial surveys delineate large polygons containing multiple stands with a single defoliation class.

3.5. Discussion

3.5.1. Hyperspectral narrow-band vegetation indices most sensitive to SBW defoliation

Our results showed that PSRI was the VI most sensitive to SBW defoliation-induced spectral change, based on RF variable importance analysis. Hawryło et al. (2018) also tested PSRI values from single Sentinel-2 images to estimate Scots pine (*Pinus*

sylvestris L.) defoliation but it was reported to be non-significant. Our methods differed by using change detection and narrow-band VIs. PSRI was developed as a non-destructive method to estimate plant senescence and foliage color change (Merzlyak et al., 1999). PSRI can be considered more objective compared to aerial surveys that attempt to visually discriminate healthy green foliage from damaged red-brown foliage caused by SBW defoliation.

MSI and NDWI describe canopy water content calculated from bands in the NIR (non-sensitive to water absorption) and SWIR (sensitive to water absorption) spectral regions and have been tested for detecting forest damage by insects. NDWI and a modified version incorporating 1640 nm and 2130 nm water absorption regions were important for detecting gypsy moth (*Lymantria dispar* L.) defoliation (De Beurs and Townsend, 2008; Townsend et al., 2012). MSI also showed sensitivity to cumulative SBW defoliation and mountain pine beetle damage (Franklin et al., 2008; White et al., 2007). Rahimzadeh-Bajgiran et al. (2018) did not evaluate MSI or NDWI for detecting annual SBW defoliation but concluded the mathematically similar NDMI was best. Collectively, research shows VIs describing canopy water content are useful in detecting annual SBW defoliation.

MSR and EVI are indicators of vegetation chlorophyll content (Chen, 1996) and canopy foliage structure (Huete et al., 2002), respectively, and both indices showed sensitivity to SBW defoliation. MSR and EVI are more resistant to reflectance saturation in high biomass conditions and atmospheric effects on spectral signal compared to the similar Simple Ratio (SR) and NDVI (Huete et al., 2002). The relatively dense, high biomass forest conditions of our study area may have factored in ranking MSR and EVI

higher for detecting defoliation versus the similar SR and NDVI. However, not all sensor spectral ranges are equal, and if limited (e.g., no bands ≤ 500 nm), deriving MSR and EVI may not be possible making SR and NDVI suitable alternatives.

The five selected VIs (PSRI, MSI, NDWI, MSR, and EVI) represent portions of the red-edge, NIR, and SWIR spectral regions that are appropriate for monitoring stress-induced vegetation change (Adelabu et al., 2012). Our results also support the single tree spectrometer measurements of current SBW defoliation by Leckie et al. (1988), which identified the spectral regions 2030–2210, 660–670, 1560–1620, and 770–790 nm in decreasing order of importance; only the 2030–2210 nm region was not relevant in our study. The relationship of VIs to forest defoliation can vary from site to site, and Rullan-Silva et al. (2013) recommended exploring multiple VIs. The influence that different variable selection methods have on results is not fully understood. However, the versatility of the RF algorithm has led to its increased use in remote sensing studies (Belgiu and Dra, 2016).

3.5.2. Random Forest and Support Vector Machine classifiers for SBW defoliation

RF and SVM classifiers have become common methods for remote sensing forest defoliation. Adelabu et al. (2014b) applied the RF classifier to FieldSpec HandHeld 2 hyperspectral data for estimating three classes of Mopane woodland (*Colophospermum mopane* Benth.) defoliation achieving 81% accuracy. Rahimzadeh-Bajgiran et al. (2018) applied RF to Landsat-5 imagery classifying annual SBW defoliation by four classes achieving 64% overall accuracy. Fassnacht et al. (2014) used SVM for classifying European bark beetle induced (*Ips typograpus* L.) tree mortality from HyMap

hyperspectral imagery, reporting accuracies of 84–96%. Finally, Hawryło et al. (2018) found overall accuracies of 75% and 78% using RF and SVM with Sentinel-2 imagery for estimating two classes of Scots pine defoliation. Our results are encouraging with overall accuracies of 91% and 88% for RF and SVM using five VIs, and considerably more accurate than the 38% for aerial surveys. RF and SVM classifiers combining multiple VIs leveraging different aspects of forest health changes can detect defoliation (Hawryło et al., 2018; Rahimzadeh-Bajgiran et al., 2018).

3.5.3. Classifier performance compared with sample plot SBW defoliation classes

Semi-supervised RF and SVM classifiers were trained using 824 plots generated within the same stands as the 68 measured defoliation field plots retained for validation. The approach produced a large classifier training dataset, and extracting mean area-weighted VI changes avoided replicating data similar to validation plots, which can inflate accuracy. Also, we assumed that within-stand defoliation variability is relatively low (MacLean and Lidstone, 1982; Ostaff and MacLean, 1989) and therefore assigning training plots a similar defoliation class as the nearest validation plot was acceptable. However, with inherently high spatial autocorrelation between training and validation plots, inflated accuracies are possible (Millard and Richardson, 2015). Branch sampling, which accurately measures SBW defoliation is a time-consuming method (MacLean and MacKinnon, 1996, 1998) that limited the number of validation plots that could properly be established. Although, the validation plot dataset provided support for the recommended use of accurate tree- and plot-level defoliation data for classifying

defoliation using remote sensing data (Hall et al., 2009; Rahimzadeh-Bajgiran et al., 2018).

3.5.4. Remote sensing challenges and limitations for detecting annual SBW defoliation

Misclassified annual SBW defoliation occurred mainly between light and moderate classes. All three validation plots with misclassified light defoliation were rated as moderate defoliation. Similarly, four of five plots with misclassified moderate defoliation were classified as light defoliation. Similar issues discriminating light from nil or moderate defoliation levels have been observed using Landsat-5 imagery (Rahimzadeh-Bajgiran et al., 2018) and during aerial surveys (MacLean and MacKinnon, 1996). During early stages of SBW outbreaks, within-stand defoliation can vary with uneven SBW populations, stand structure, and SBW-host species compositions (Nealis and Régnière, 2004). Such defoliation conditions can result in overlapping spectral data per pixel, increasing misclassifications. Detecting low defoliation levels is also logistically challenging, if not impossible, for aerial survey methods to detect subtle foliage damage and discoloration within single stands. Our results demonstrate that pixel-level within-stand defoliation can be estimated using satellite hyperspectral imagery. This higher spatial resolution defoliation data could greatly improve the effectiveness in spraying bioinsecticides, forecasting outbreak spread, and accuracy of quantifying damage in SBW management.

Satellite sensor spatial resolutions often include large pixel sizes as a trade-off for increased image scene coverage. Achieving finer spatial resolutions producing single tree defoliation is of interest for disentangling noisy spectra signals. Sensors with submeter

spatial resolutions (< 1 m; Worldview-3), above canopy aerial platforms (Unmanned Aerial Vehicles; UAVs), and image-enhancing methods (panchromatic-sharpening) could increase the accuracy of defoliation estimates for use in SBW management. However, spatial coverage, image availability, and cost currently limit the operational use of such technologies.

Although the EO-1 satellite was decommissioned in 2017, many new satellite hyperspectral missions have recently or are soon planned for launch. For example, the German Aerospace Center DESIS (DLR Earth Sensing Imaging Spectrometer) sensor was installed on the International Space Station in August 2018 (Alonso et al., 2019). The hyperspectral satellite PRISMA (PRecursore IperSpettrale della Missione Applicativa) is an Italian Space Agency mission launched in March 2019 (Loizzo et al., 2019). Moreover, the German satellite EnMAP (Environmental Mapping and Analysis Program) is expected to launch in 2020 (Sornig et al., 2018). Also, the CHIME (Copernicus Hyperspectral Imaging Mission for the Environment) project aims to develop synergies between PRISMA and EnMAP image products, increasing the availability of hyperspectral observations (Nieke and Rast, 2018). These advancements will allow further research using hyperspectral imagery to improve the detection of annual SBW defoliation. Reliable detection of low-level defoliation using hyperspectral or high spatial and temporal resolution sensors would be of research value for the SBW Early Intervention Strategy test currently underway in Atlantic Canada (MacLean et al., 2019).

3.6. Conclusions

We used change detection of narrow-band VIs calculated from satellite hyperspectral images with semi-supervised RF and SVM classifiers to estimate three classes of annual SBW defoliation. The results demonstrated promise for use of satellite hyperspectral imagery to detect annual SBW defoliation and were significantly superior to defoliation estimates by aerial surveys. Accuracy was improved from 38% by aerial surveys to 91% by using satellite hyperspectral imagery and RF or SVM classification.

From the technical experiments conducted in this study, the key findings included:

1. In order of decreasing importance, PSRI, MSI, NDWI, MSR, and EVI were the top five VIs sensitive to annual SBW defoliation. These VIs used the red-edge, NIR, and SWIR spectral regions for monitoring stress-induced vegetation change, and represented foliage senescence (PSRI), canopy water content (MSI; NDWI), chlorophyll content (MSR), and canopy structure (EVI) changes caused by SBW defoliation.
2. Both RF and SVM machine-learning classifiers performed similarly, with overall classification accuracies of 91% and 88%, respectively, using five VIs and both outperformed aerial surveys, which were only 38% accurate compared to a detailed validation plot dataset. Model parameter tuning of SVM did not increase classification accuracies in comparison with using parameter defaults for RF.
3. Of the three defoliation classes, discriminating between light and moderate defoliation was most difficult, making up 83% and 88% of the total misclassifications for RF and SVM, respectively. One contributing factor is the defoliation variability

among trees at lower levels per pixel, which is a common issue for other remote sensing technology with spatial resolutions encompassing groups of trees and for aerial surveys.

4. The timing of satellite hyperspectral images was approximately six weeks after the ideal 2–3 week defoliation detection period for both study areas. Defoliation classification accuracies were acceptable, supporting hyperspectral image change detection can provide a technique for extending monitoring outside the ideal detection period.

3.7. Acknowledgements

This research was funded by the AWARE (Assessment of Wood Attributes using Remote sEnsing) Natural Sciences and Engineering Research Council of Canada Collaborative Research and Development project led by Dr. Nicholas Coops, Grant number CRDPJ 462973-14. The Québec Ministère des Forêts de la Faune et des Parcs and the Société de Protection des Forêts contre les Insectes et Maladies provided aerial orthophotos and SBW defoliation survey data. Special thanks to field technicians Jessica Cormier, Olivia Doran, and Rebecca Landry, who assisted in collecting field plot defoliation data.

3.8. References

Adelabu, S., Mutanga, O., Adam, E., 2014a. Evaluating the impact of red-edge band from Rapideye image for classifying insect defoliation levels. ISPRS J. Photogramm. Remote Sens. 95, 34–41.

Adelabu, S., Mutanga, O., Adam, E., Sebego, R., 2014b. Spectral discrimination of insect defoliation levels in Mopane woodland using hyperspectral data. IEEE J. Sel. Top. Appl. Earth Obs. Remote Sens. 7 (1).

Adelabu, S., Mutanga, O., Azong, M., 2012. A review of remote sensing of insect defoliation and its implications for the detection and mapping of *Imbrasia belina* defoliation of Mopane woodland. African J. Plant Sci. Biotechnol. 6 (1), 1–13.

Alonso, K., Bachmann, M., Burch, K., Carmona, E., Cerra, D., de los Reyes, R., Dietrich, D., Heiden, U., Hölderlin, A., Ickes, J., Knodt, U., Krutz, D., Lester, H., Müller, R., Pagnutti, M., Reinartz, P., Richter, R., Ryan, R., Sebastian, I., Tegler, M., 2019. Data products, quality and validation of the DLR earth sensing imaging spectrometer (DESIS). Sensors 19 (4471).

Archambault, L., Morissette, J., Bernier-Cardou, M., 1998. Forest succession over a 20-year period following clearcutting in balsam fir-yellow birch ecosystems of eastern Québec, Canada. For. Ecol. Manage. 102, 61–74.

Ballanti, L., Blesius, L., Hines, E., Kruse, B., 2016. Tree species classification using hyperspectral imagery: a comparison of two classifiers. Remote Sens. 8 (445).

Bélanger, L., Bergeron, Y., Camiré, C., 1992. Ecological land survey in Québec. For. Chron. 68 (1).

Belgiu, M., Dra, L., 2016. Random forest in remote sensing: a review of applications and future directions. ISPRS J. Photogramm. Remote Sens. 114, 24–31.

Breiman, L., 2001. Random Forests. Mach. Learn. 45, 5–32.

Canadian National Forest Inventory, 2013. Area of forest land by species group and age class in Canada. https://nfi.nfis.org/resources/general/summaries/en/html/CA3_T14_LSAGE20_AREA_en.html (accessed 1.19.19).

Chang, W-Y., Lantz, V.A., Hennigar, C.R., MacLean, D.A., 2012. Economic impacts of forest pests: a case study of spruce budworm outbreaks and control in New Brunswick, Canada. Can. J. For. Res. 42, 490–505.

Chen, C., Weiskittel, A., Bataineh, M., MacLean, D.A., 2018. Refining the Forest Vegetation Simulator for projecting the effects of spruce budworm defoliation in the Acadian Region of North America. For. Chron. 94 (3).

Chen, J.M., 1996. Evaluation of vegetation indices and a modified simple ratio for boreal applications. Can. J. Remote Sens. 22, 229–242.

Claverie, M., Ju, J., Masek, J.G., Dungan, J.L., Vermote, E.F., Roger, J-C., Skakun, S. V., Justice, C., 2018. The Harmonized Landsat and Sentinel-2 surface reflectance data set. Remote Sens. Environ. 219, 145–161.

Congalton, R.G., 1991. A review of assessing the accuracy of classifications of remotely sensed data. Remote Sens. Environ. 37, 35–46.

Coulombe Commission (Commission d'étude sur la gestion de la forêt publique québécoise), 2004. Chapitre 4: Protection, conservation et gestion multiressource: Des axes de changement. In Commission d'étude sur la gestion de la forêt publique québécoise, Rapport final; Ministère des Forêts, de la Faune et des Parcs: Québec, QC, Canada, 2004; pp.47–92.

Datt, B., McVicar, T.R., Van Niel, T.G., Jupp, D.L.B., Pearlman, J.S., 2003. Preprocessing EO-1 Hyperion hyperspectral data to support the application of agricultural indexes. IEEE Trans. Geosci. Remote Sens. 41 (6).

Daughtry, C.S.T., Walthall, C.L., Kim, M.S., Brown de Colstoun, E., McMurtrey III, J.E., 2000. Estimating corn leaf chlorophyll concentration from leaf and canopy reflectance. Remote Sens. Environ. 74, 229–239.

De Beurs, K.M., Townsend, P.A., 2008. Estimating the effect of gypsy moth defoliation using MODIS. Remote Sens. Environ. 112, 3983–3990.
Donovan, S.D., MacLean, D.A., Kershaw, J.A., Lavigne, M.B., 2018. Quantification of forest canopy changes caused by spruce budworm defoliation using digital hemispherical imagery. Agric. For. Meteorol. 262, 89–99.
Dormann, C.F., Elith, J., Bacher, S., Buchmann, C., Carl, G., Carré, G., Marquéz, J.R.G., Gruber, B., Lafourcade, B., Leitão, P.J., Münkemüller, T., Mcclean, C., Osborne, P.E., Reineking, B., Schröder, B., Skidmore, A.K., Zurell, D., Lautenbach, S., 2013. Collinearity: a review of methods to deal with it and a simulation study evaluating their performance. Ecography. 36, 27–46.
Eigemeier, E., Heiskanen, J., Rautiainen, M., Mttus, M., Vesanto, V-H., Majasalmi, T., Stenberg, P., 2012. Narrowband vegetation indices for estimating boreal forest leaf area index. In: Escalante-Ramirez, B. (Ed.), Remote Sensing - Applications (Chapter 1). Croatia. pp. 1–29.
Erdle, T.A., MacLean, D.A., 1999. Stand growth model calibration for use in forest pest impact assessment. For. Chron. 75 (1).
Fassnacht, F.E., Latifi, H., Ghosh, A., Joshi, P.K., Koch, B., 2014. Assessing the potential of hyperspectral imagery to map bark beetle-induced tree mortality. Remote Sens. Environ. 140, 533–548.
Fettes, J.J., 1950. Investigations of sampling techniques for population studies of the spruce budworm on balsam fir in Ontario. For. Insect Lab. Sault Ste. Marie, Ont., Ann. Tech. Rep. 4. pp. 163–401.
Franklin, S.E., Fan, H., Guo, X., 2008. Relationship between Landsat TM and SPOT vegetation indices and cumulative spruce budworm defoliation. Int. J. Remote Sens. 29, 1215–1220.
Gamon, J.A., Serrano, L., Surfus, J.S., 1997. The photochemical reflectance index: an optical indicator of photosynthetic radiation use efficiency across species, functional types, and nutrient levels. Oecologia 112, 492–501.
Gao, B., 1996. NDWI - a normalized difference water index for remote sensing of vegetation liquid water from space. Remote Sens. Environ. 58, 257–266.
Gitelson, A.A., Kaufman, Y.J., Merzlyak, M.N., 1996. Use of a green channel in remote sensing of global vegetation from EOS-MODIS. Remote Sens. Environ. 58, 289–298.
Goodbody, T.R.H., Coops, N.C., Hermosilla, T., Tompalski, P., McCartney, G., MacLean, D.A., 2018. Digital aerial photogrammetry for assessing cumulative spruce budworm defoliation and enhancing forest inventories at a landscape-level. ISPRS J. Photogramm. Remote Sens. 142, 1–11.
Goodenough, D.G., Dyk, A., Niemann, K.O., Pearlman, J.S., Chen, H., Han, T., Murdoch, M., West, C., 2003. Processing Hyperion and ALI for forest classification. IEEE Trans. Geosci. Remote Sens. 41 (6).
Haixiang, G., Yijing, L., Shang, J., Mingyun, G., Yuanyue, H., Bing, G., 2017. Learning from class-imbalanced data: review of methods and applications. Expert Syst. Appl. 73, 220–239.
Hall, R.J., Filiatrault, M., Deschamps, A., Arsenault, E., 2009. Mapping Eastern spruce budworm cumulative defoliation severity from Landsat and SPOT. In: 30th

Canadian Symposium on Remote Sensing (CSRS), Lethbridge, Alberta. pp. 1190–1194.
Hall, R.J., Castilla, G., White, J.C., Cooke, B.J., Skakun, R.S., 2016. Remote sensing of forest pest damage: a review and lessons learned from a Canadian perspective. Can. Entomol. 148, S296–S356.
Han, H., Guo, X., Yu, H., 2016. Variable selection using Mean Decrease Accuracy and Mean Decrease Gini based on Random Forest. In: Proceedings of the 7th IEEE International Conference on Software Engineering and Service Sciences (ICSESS), Beijing, China. pp. 219–224.
Han, T., Goodenough, D.G., Dyk, A., Love, J., 2002. Detection and correction of abnormal pixels in Hyperion images, in: IEEE International Geoscience and Remote Sensing Symposium (IGARSS), Toronto, Canada. pp. 1327–1330.
Hawryło, P., Bednarz, B., Wężyk, P., Szostak, M., 2018. Estimating defoliation of Scots pine stands using machine learning methods and vegetation indices of Sentinel-2. Eur. J. Remote Sens. 51, 194–204.
Hennigar, C.R., Erdle, T.A., Gullison, J.J., MacLean, D.A., 2013. Re-examining wood supply in light of future spruce budworm outbreaks: a case study in New Brunswick. For. Chron. 89 (1).
Henrich, V., Krauss, G., Götze, C., Sandow, C., 2012. IDB - A database for remote sensing indices. Dep. Geogr. Univ. Bonn, Ger. https://www.indexdatabase.de (accessed 7.1.19).
Hijmans, R.J., 2019. raster: Geographic Data Analysis and Modeling. R package version 2.9-5. https://CRAN.R-project.org/package=raster.
Huang, Z., 2015. Remote sensing of spruce budworm defoliation in Québec, Canada using EO-1 Hyperion data. MScE thesis. University of New Brunswick, Fredericton, NB, Canada.
Huete, A., Didan, K., Miura, T., Rodriguez, E.P., Gao, X., Ferreira, L.G., 2002. Overview of the radiometric and biophysical performance of the MODIS vegetation indices. Remote Sens. Environ. 83, 195–213.
Huete, A.R., 1988. A soil-adjusted vegetation index (SAVI). Remote Sens. Environ. 25, 295–309.
Hunt, E.R.J., Rock, B.N., 1989. Detection of changes in leaf water content using near- and middle-infrared reflectances. Remote Sens. Environ. 30, 43–54.
Ishak, A.B., 2016. Variable selection using support vector regression and random forests: a comparative study. Intell. Data Anal. 20, 83–104.
Jordan, C.F., 1969. Derivation of leaf-area index from quality of light on the forest floor. Ecology 50 (4), 663–666.
Kettela, E.G., 1983. A cartographic history of spruce budworm defoliation 1967–1981 in eastern North America. Canadian Forestry Service, Maritime Forest Research Centre, Fredericton, N.B., Canada. Inf. Rep. DPC-X-14.
Lausch, A., Erasmi, S., King, D.J., Magdon, P., Heurich, M., 2016. Understanding forest health with remote sensing Part I - a review of spectral traits, processes and remote sensing characteristics. Remote Sens. 8 (1029).
Leckie, D.G., Teillet, P.M., Ostaff, D.P., Defosejevs, G., 1988. Sensor band selection for detecting current defoliation caused by the spruce budworm. Remote Sens.

Environ. 26, 31–50.
Lévesque, R.C., Cusson, M., Lucarotti, C., 2010. BEGAB: Budworm Eco-Genomics: Applications & Biotechnology. Institut de biologie intégrative et des systemès, Université Laval: Québec City, QC, Canada.
Li, J., Plaza, A., 2016. Hyperspectral Image Processing: Methods and Approaches. In: Thenkabail, P. (Ed.), Remote Sensed Data Characterization, Classification, and Accuracies (Chapter 12). CRC Press: Boca Raton, FL, USA.
Liaw, A., Wiener, M., 2002. Classification and regression by RandomForest. R News 2, 18–22.
Liu, L., Coops, N.C., Aven, N.W., Pang, Y., 2017. Mapping urban tree species using integrated airborne hyperspectral and LiDAR remote sensing data. Remote Sens. Environ. 200, 170–182.
Liu, S., Du, Q., Tong, X., Samat, A., Pan, H., Ma, X., 2017. Band selection-based dimensionality reduction for change detection in multi-temporal hyperspectral images. Remote Sens. 9 (1008).
Loizzo, R., Daraio, M., Guarini, R., Longo, F., Lorusso, R., Dini, L., Lopinto, E., 2019. PRIMA Mission Status and Perspective. In: IEEE International Geoscience and Remote Sensing Symposium (IGARSS), Yokohama, Japan. pp. 4503–4506.
MacLean, D.A., 1980. Vulnerability of fir-spruce stands during uncontrolled spruce budworm outbreaks: a review and discussion. For. Chron. 56 (5).
MacLean, D.A., Lidstone, R.G., 1982. Defoliation by spruce budworm: estimation by ocular and shoot-count methods and variability among branches, trees, and stands. Can. J. For. Res. 12, 582–594.
MacLean, D.A., MacKinnon, W.E., 1996. Accuracy of aerial sketch-mapping estimates of spruce budworm defoliation in New Brunswick. Can. J. For. Res. 26, 2099–2108.
MacLean, D.A., MacKinnon, W.E., 1998. Sample sizes required to estimate defoliation of spruce and balsam fir caused by spruce budworm accurately. North. J. Appl. For. 15 (3).
MacLean, D.A., Porter, K.B., 1994. Development of a decision support system for spruce budworm and forest management planning in Canada, in: Decision Making with GIS - The Fourth Dimension. Vol. 2. Proc. GIS 1994 Symposium, Vancouver, BC. pp. 863–872.
MacLean, D.A., Amirault, P., Amos-Binks, L., Carleton, D., Hennigar, C., Johns, R., Régnière, J., 2019. Positive results of an early intervention strategy to suppress a spruce budworm outbreak after five years of trials. Forests 10 (448).
MacLean, D.A., Erdle, T.A., MacKinnon, W.E., Porter, K.B., Beaton, K.P., Cormier, G., Morehouse, S., Budd, M., 2001. The Spruce Budworm Decision Support System: forest protection planning to sustain long-term wood supply. Can. J. For. Res. 31, 1742–1757.
Maxwell, A.E., Warner, T.A., Fang, F., 2018. Implementation of machine-learning classification in remote sensing: an applied review. Int. J. Remote Sens. 39 (9), 2784–2817.
Merzlyak, M.N., Gitelson, A.A., Chivkunova, O.B., Rakitin, V.Y., 1999. Non-destructive optical detection of pigment changes during leaf senescence and fruit ripening.

Physiol. Plant. 106, 135–141.
Meyer, D., Dimitriadou, E., Hornik, K., Weingessel, A., Leisch, F., 2019. e1071: Misc Functions of the Department of Statistics, Probability Theory Group (Formerly: E1071), TU Wien. R package version 1.7-2. https://CRAN.R-project.org/package=e1071.
Millard, K., Richardson, M., 2015. On the importance of training data sample selection in Random Forest image classification: a case study in peatland ecosystem mapping. Remote Sens. 7, 8489–8515.
Miller, C.A., 1977. The feeding impact of spruce budworm on balsam fir. Can. J. For. Res. 7, 76–84.
Nealis, V.G., Régnière, J., 2004. Insect-host relationships influencing disturbance by the spruce budworm in a boreal mixedwood forest. Can. J. For. Res. 34, 1870–1882.
Nieke, J., Rast, M., 2018. Towards the Copernicus Hyperspectral Imaging Mission For The Environment (CHIME). In: IEEE International Geoscience and Remote Sensing Symposium (IGARSS), Valencia, Spain. pp. 157–159.
Noi, P.T., Kappas, M., 2018. Comparison of Random Forest, k-Nearest Neighbor, and Support Vector Machine classifiers for land cover classification using Sentinel-2 imagery. Sensors 18 (18).
Ostaff, D.P., MacLean, D.A., 1989. Spruce budworm populations, defoliation, and changes in stand condition during an uncontrolled spruce budworm outbreak on Cape Breton Island, Nova Scotia. Can. J. For. Res. 19, 1077–1086.
Oumar, Z., Mutanga, O., Ismail, R., 2013. Predicting *Thaumastocoris peregrinus* damage using narrow band normalized indices and hyperspectral indices using field spectra resampled to the Hyperion sensor. Int. J. Appl. Earth Obs. Geoinf. 21, 113–121.
Pearlman, J.S., Barry, P.S., Segal, C.C., Shepanski, J., Beiso, D., Carman, S.L., 2003. Hyperion, a space-based imaging spectrometer. IEEE Trans. Geosci. Remote Sens. 41 (6).
Penuelas, J., Filella, I., 1998. Visible and near-infrared reflectance techniques for diagnosing plant physiological status. Trends Plant Sci. 3 (4).
Penuelas, J., Pinol, J., Ogaya, R., Filella, I., 1997. Estimation of plant water concentration by the reflectance Water Index WI (R900/R970). Int. J. Remote Sens. 18 (13), 2869–2875.
Pontius, J., Martin, M., Plourde, L., Hallett, R., 2008. Ash decline assessment in emerald ash borer-infested regions: a test of tree-level, hyperspectral technologies. Remote Sens. Environ. 112, 2665–2676.
Pontius, R.G.J., Millones, M., 2011. Death to Kappa: birth of quantity disagreement and allocation disagreement for accuracy assessment. Int. J. Remote Sens. 32 (15), 4407–4429.
Québec Ministère des Forêts de la Faune et des Parcs (QMFFP), 2016. Aires infestées par la tordeuse des bourgeons de l'épinette au Québec en 2016 - Québec Ministère des Forêts de la Faune et des Parcs, Direction de la protection des forêts, Québec. 16p.
Québec Ministère des Forêts de la Faune et des Parcs (QMFFP), 2019. Aires infestées par la tordeuse des bourgeons de l'épinette au Québec en 2019 - Québec Ministère des Forêts de la Faune et des Parcs, Direction de la protection des forêts, Québec. 32p.
R Core Team, 2019. R: A language and environment for statistical computing. R

Foundation for Statistical Computing, Vienna, Austria. https://www.R-project.org/.
Rahimzadeh-Bajgiran, P., Weiskittel, A., Kneeshaw, D., MacLean, D., 2018. Detection of annual spruce budworm defoliation and severity classification using Landsat imagery. Forests 9 (357).
Régnière, J., Saint-Amant, R., Béchard, A., Moutaoufik, A., 2017. BioSIM 11 User's Manual. Canadian Forest Service, Laurentian Forestry Centre, Québec. Information Report LAU-X-137, 67p.
Rowe, J.S., 1972. Forest regions of Canada. Canadian Forestry Service. Ottawa, Canada. Publication 1300.
Rullan-Silva, C.D., Olthoff, A.E., Delgado de la Mata, J.A., Pajares-Alonso, J.A., 2013. Remote monitoring of forest insect defoliation: a review. For. Syst. 22 (3), 377–391.
San, B.T., Süzen, M.L., 2011. Evaluation of cross-track illumination in EO-1 Hyperion imagery for lithological mapping. Int. J. Remote Sens. 32 (22), 7873–7889.
Senf, C., Seidl, R., Hostert, P., 2017. Remote sensing of forest insect disturbances: current state and future directions. Int. J. Appl. Earth Obs. Geoinf. 60, 49–60.
Sornig, M., Fischer, S., Chlebek, C., Muecke, M., Honold, H.-P., Heider, B., 2018. The hyperspectral instrument onboard EnMAP, overview and current status. In: International Conference on Space Optics (ICSO), Chania, Greece. p. 6.
Townsend, P.A., Singh, A., Foster, J.R., Rehberg, N.J., Kingdon, C.C., Eshleman, K.N., Seagle, S.W., 2012. A general Landsat model to predict canopy defoliation in broadleaf deciduous forests. Remote Sens. Environ. 119, 255–265.
Tucker, C.J., 1979. Red and photographic infrared linear combinations for monitoring vegetation. Remote Sens. Environ. 8, 127–150.
White, J.C., Coops, N.C., Hilker, T., Wulder, M.A., Carroll, A.L., 2007. Detecting mountain pine beetle red attack damage with EO-1 Hyperion moisture indices. Int. J. Remote Sens. 28 (10), 2111–2121.
Wilson, E.H., Sader, S.A., 2002. Detection of forest harvest type using multiple dates of Landsat TM imagery. Remote Sens. Environ. 80, 385–396.

Table 3.1: Details of 14 vegetation indices and their corresponding band wavelength formulas for detecting annual SBW defoliation using hyperspectral imagery. Indices are grouped into vegetation greenness, canopy water content, and light use efficiency categories.

Category	Vegetation Index	Acronym	Formula	Reference
Vegetation Greenness	Simple Ratio	SR	ρ_{800}/ρ_{680}	Jordan, 1969
	Modified Simple Ratio	MSR	$\frac{(\rho_{800}-\rho_{445})}{(\rho_{680}-\rho_{445})}$	Chen, 1996
	Normalized Difference Vegetation Index	NDVI	$\frac{(\rho_{800}-\rho_{680})}{(\rho_{800}+\rho_{680})}$	Tucker, 1979
	Green Normalized Difference Vegetation Index	GNDVI	$\frac{(\rho_{800}-\rho_{550})}{(\rho_{800}+\rho_{550})}$	Gitelson et al., 1996
	Enhanced Vegetation Index	EVI	$\left(\frac{(\rho_{800}-\rho_{670})}{(\rho_{800}-(6*\rho_{670})-(7.5*\rho_{475})+1)}\right)*2.5$	Huete et al., 2002
	Soil Adjusted Vegetation Index	SAVI	$\frac{(\rho_{800}-\rho_{670})*(1+0.5)}{(\rho_{800}+\rho_{670}+0.5)}$	Huete, 1988
Canopy Water Content	Moisture Stress Index	MSI	ρ_{1600}/ρ_{820}	Hunt and Rock, 1989
	Plant Water Index	PWI	ρ_{970}/ρ_{900}	Penuelas et al., 1997
	Normalized Difference Moisture Index	NDMI	$\frac{(\rho_{820}-\rho_{1600})}{(\rho_{820}+\rho_{1600})}$	Wilson and Sader, 2002
	Normalized Difference Water Index	NDWI	$\frac{(\rho_{860}-\rho_{1240})}{(\rho_{860}+\rho_{1240})}$	Gao, 1996

Table 3.1: *Continued*.

Category	Vegetation Index	Acronym	Formula	Reference
Light Use Efficiency	Modified Chlorophyll Absorption Reflectance Index	MCARI	$\left((\rho_{700} - \rho_{670}) - 0.2(\rho_{700} - \rho_{550})\right) * (\rho_{700}/\rho_{670})$	Daughtry et al., 2000
	Photochemical Reflectance Index	PRI	$\frac{(\rho_{531} - \rho_{570})}{(\rho_{531} + \rho_{570})}$	Gamon et al., 1997
	Plant Senescence Reflectance Index	PSRI	$(\rho_{680} - \rho_{500})/\rho_{750}$	Merzlyak et al., 1999
	Structure Insensitive Pigment Index	SIPI	$\frac{(\rho_{800} - \rho_{445})}{(\rho_{800} + \rho_{680})}$	Penuelas and Filella, 1998

* Note ρ_i represents the wavelengths (nm) corresponding to the closest EO-1 Hyperion band selected for calculating each vegetation index.

Table 3.2: Descriptions of semi-supervised Random Forest (RF) and Support Vector Machine (SVM) classifier models and corresponding vegetation indices (VIs) selected for classifying annual SBW defoliation. VIs were selected using forward stepwise selection in association with RF variable importance, Spearman's rank correlations relating defoliation and VI multicollinearities.

Model	Vegetation Indices
RF-1	PSRI
RF-2	PSRI + MSI
RF-3	PSRI + MSI + NDWI
RF-4	PSRI + MSI + NDWI + MSR
RF-5	PSRI + MSI + NDWI + MSR + EVI
SVM-1	PSRI
SVM-2	PSRI + MSI
SVM-3	PSRI + MSI + NDWI
SVM-4	PSRI + MSI + NDWI + MSR
SVM-5	PSRI + MSI + NDWI + MSR + EVI

* Description of VIs: PSRI (Plant Senescence Reflectance Index), MSI (Moisture Stress Index), NDWI (Normalized Difference Water Index), MSR (Modified Simple Ratio), and EVI (Enhanced Vegetation Index).

Table 3.3: Confusion matrices classifying three annual SBW defoliation classes using the best Random Forest (RF-5) and Support Vector Machine (SVM-5) classifier models and 2016 aerial survey data. Producer's and user's accuracies for each defoliation class and overall accuracy (including 95% confidence intervals) are compared to the 68 validation plots.

Random Forest Classifier

	Defoliation Class	Light	Moderate	Severe	Totals	**Producer's Accuracy %**
Validation Plot Observations	Light	**32**	1	0	33	**97.0**
	Moderate	4	**24**	1	29	**82.8**
	Severe	0	0	**6**	6	**100**
	Totals	36	25	7	**68**	
	User's Accuracy %	**88.8**	**96.0**	**85.7**		

Overall Accuracy % = 91.2 Conf. Interval % = 81.8–96.7

Support Vector Machine Classifier

	Defoliation Class	Light	Moderate	Severe	Totals	**Producer's Accuracy %**
Validation Plot Observations	Light	**31**	2	0	33	**93.9**
	Moderate	4	**24**	1	29	**82.8**
	Severe	0	1	**5**	6	**83.3**
	Totals	35	27	6	**68**	
	User's Accuracy %	**88.6**	**88.9**	**83.3**		

Overall Accuracy % = 88.2 Conf. Interval % = 78.1–94.8

Aerial Survey Defoliation

	Defoliation Class	Light	Moderate	Severe	Totals	**Producer's Accuracy %**
Validation Plot Observations	Light	**21**	3	9	33	**63.6**
	Moderate	5	**1**	**23**	29	**3.5**
	Severe	0	2	**4**	6	**66.7**
	Totals	26	6	36	**68**	
	User's Accuracy %	**80.8**	**16.7**	**11.1**		

Overall Accuracy % = 38.2 Conf. Interval % = 26.7–50.8

Table 3.4: Pixel proportions of annual defoliation by Random Forest (RF) and Support Vector Machine (SVM) classifiers compared to 2016 provincial aerial surveyed defoliation for the Amqui and Causapscal study areas. Three defoliation classes of light (L), moderate (M), and severe (S) are defined.

Study Area	**Aerial Survey (ha)**	**Defoliation Class**	**Proportion of RF classified pixels (%)**			**Proportion of SVM classified pixels (%)**		
			L	M	S	L	M	S
Amqui	4597	L	**83**	17	0	**78**	21	0
	100	M	49	**51**	0	55	**45**	0
	0	S						
Causapscal	1983	L	**46**	14	41	**45**	18	37
	1758	M	40	**22**	38	41	**24**	35
	2748	S	24	28	**48**	26	26	**48**

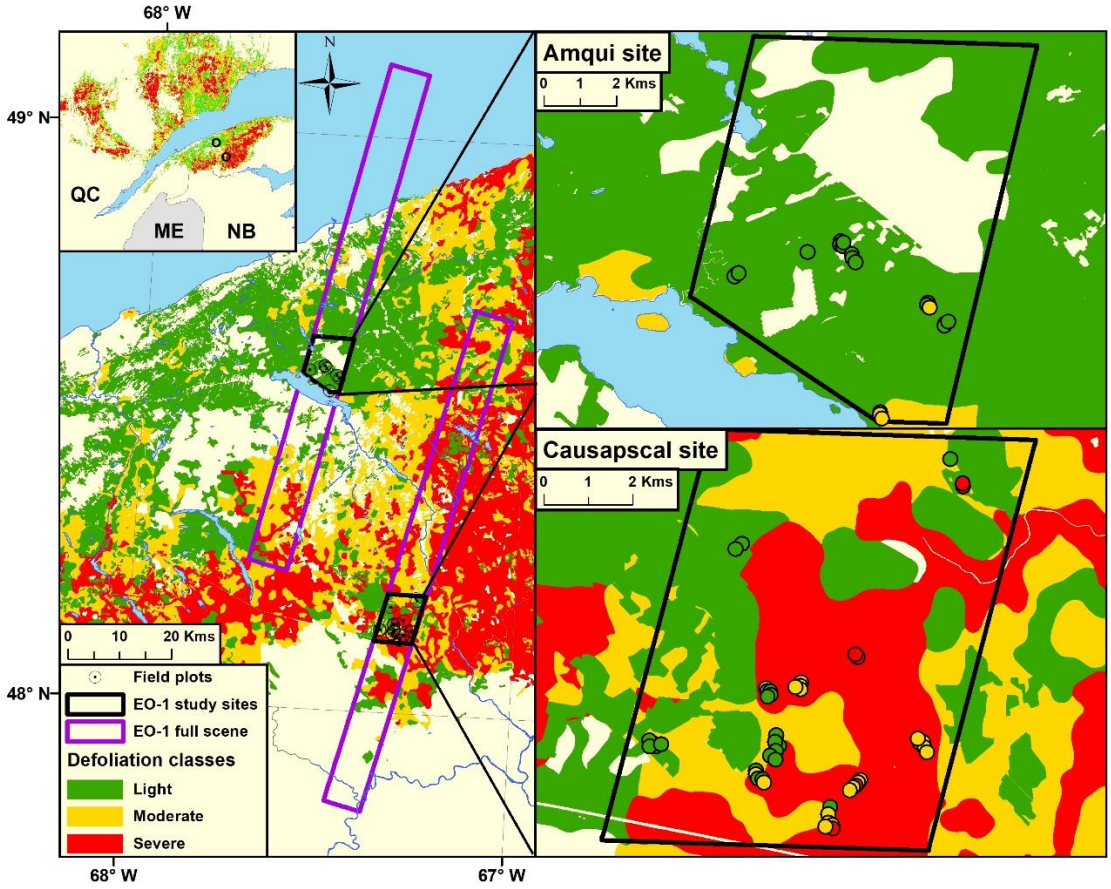

Figure 3.1: Map of study area showing 68 defoliation field plot locations and EO-1 Hyperion hyperspectral image coverage for two study areas (Amqui and Causapscal) overlaid on 2016 annual spruce budworm aerial survey defoliation (QMFFP, 2016).

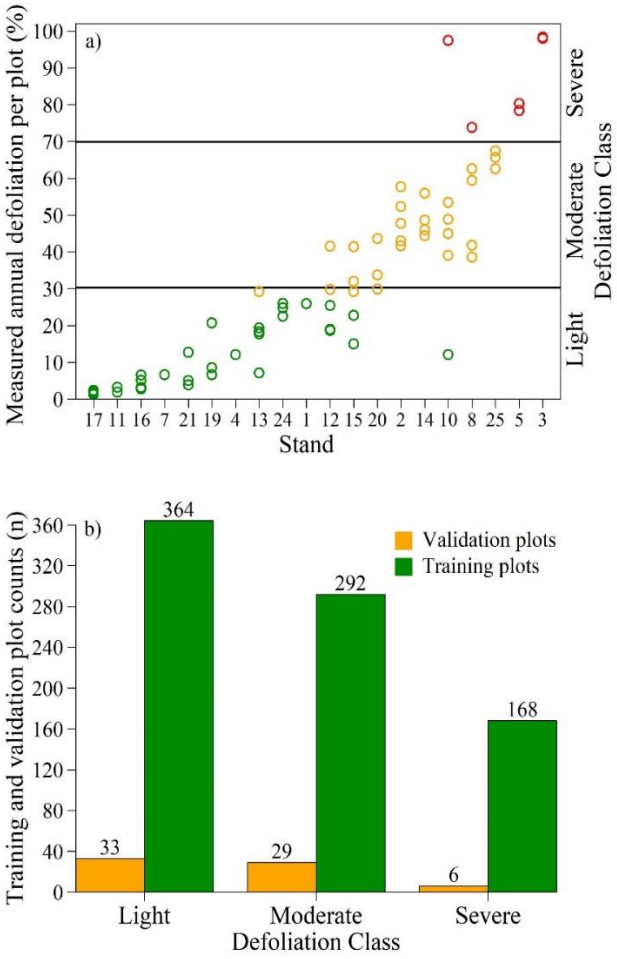

Figure 3.2: a) Distribution of mean annual branch defoliation per field plot per stand grouped by light, moderate, and severe defoliation classes. All field plot data were retained for classifier validation. b) Comparison of training plots (400m^2 circular plots adjacent to and assigned the same defoliation value as each actual field plot) and validation (actual field) plot counts per defoliation class.

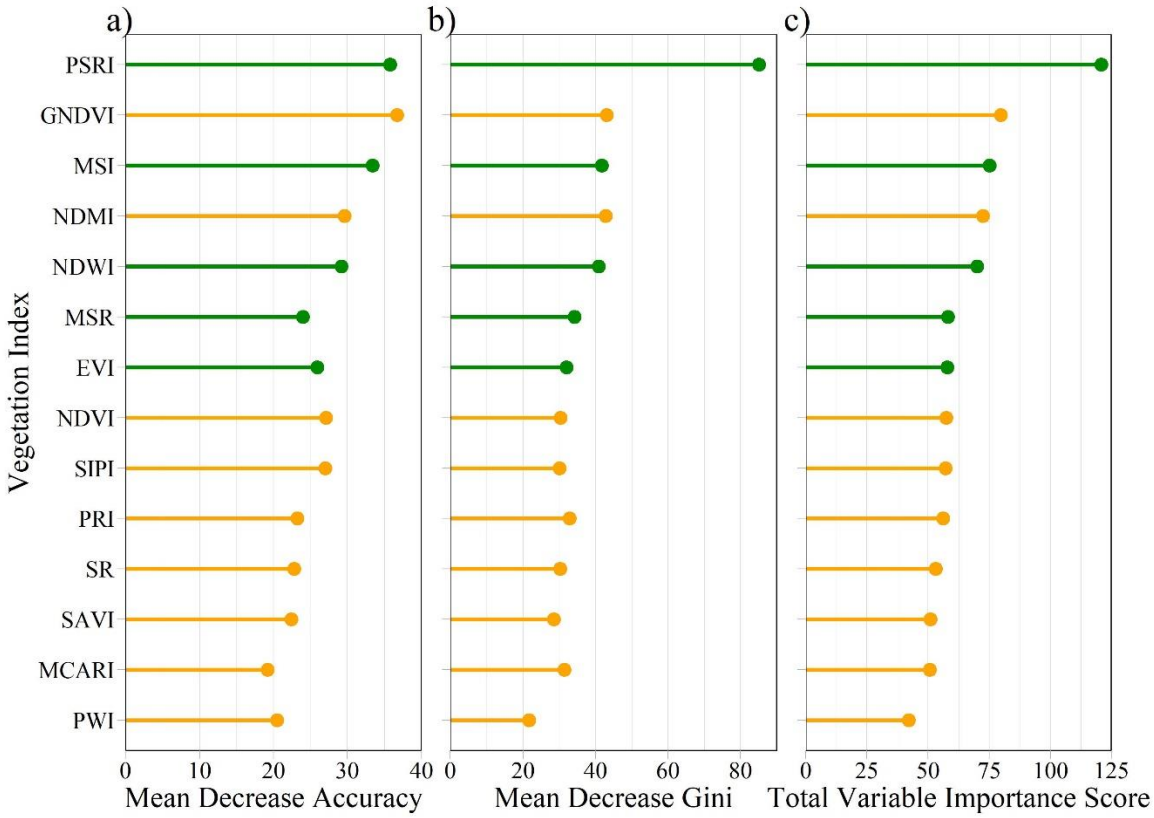

Figure 3.3: Variable importance ranking of 14 Vegetation Indices (VIs) related to three annual SBW defoliation classes. VIs colored green were selected for classifying defoliation by decreasing Total Variable Importance Score, VIs multicollinearity threshold $\leq \pm 0.7$, and a Spearman rank correlation threshold of $\geq \pm 0.3$ between VIs and defoliation. Table 3.2 describes each VI.

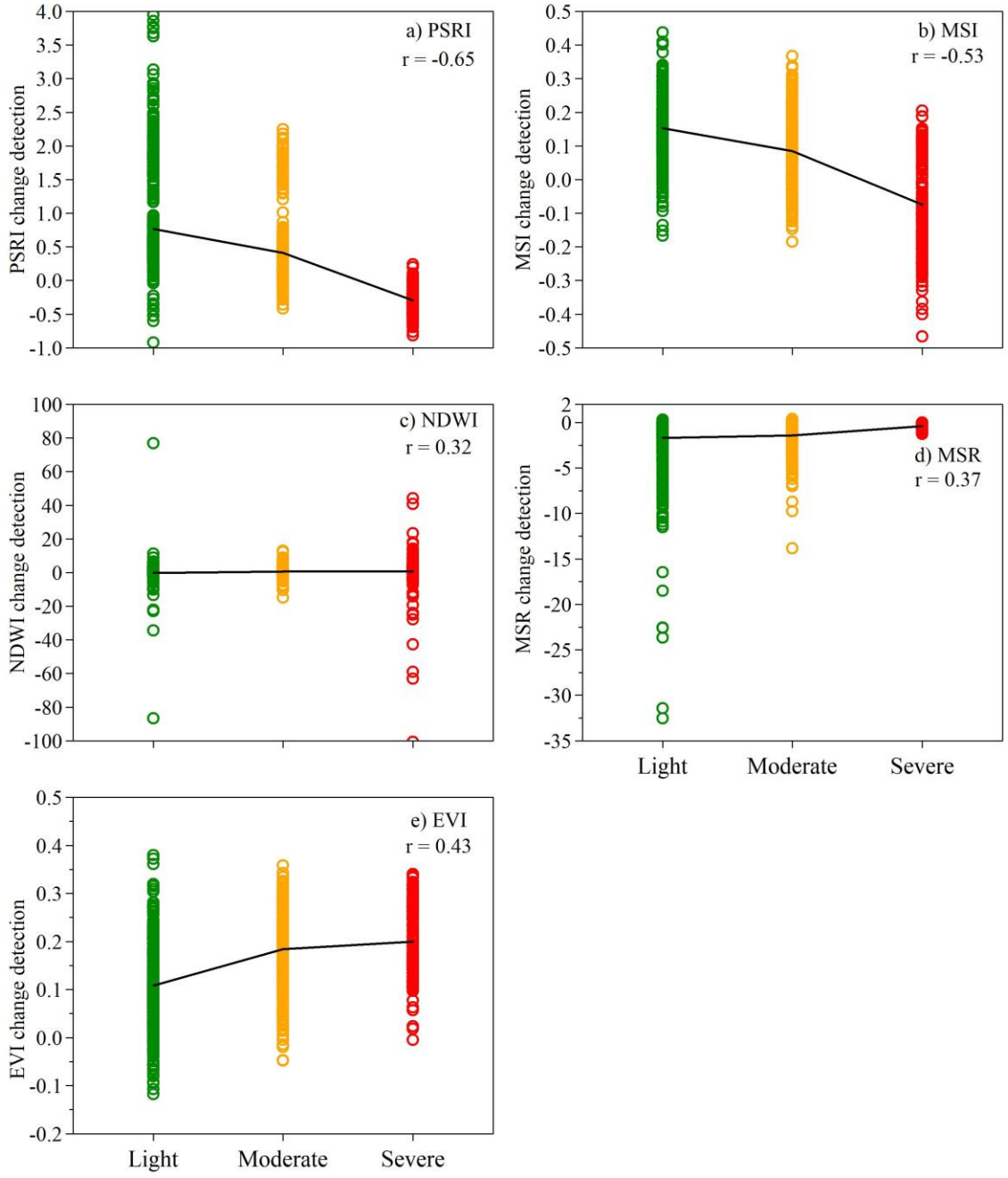

Figure 3.4: Change detection relationship of five vegetation indices selected for classifying defoliation and the combined training and validation classifier plots grouped by light (green), moderate (yellow), and severe (red) defoliation classes. Indices include: a) Plant Senescence Reflectance Index (PSRI); b) Moisture Stress Index (MSI); Normalized Difference Water Index (NDWI); Modified Simple Ratio (MSR); and Enhanced Vegetation Index (EVI). Black lines represent means for each VI per defoliation class.

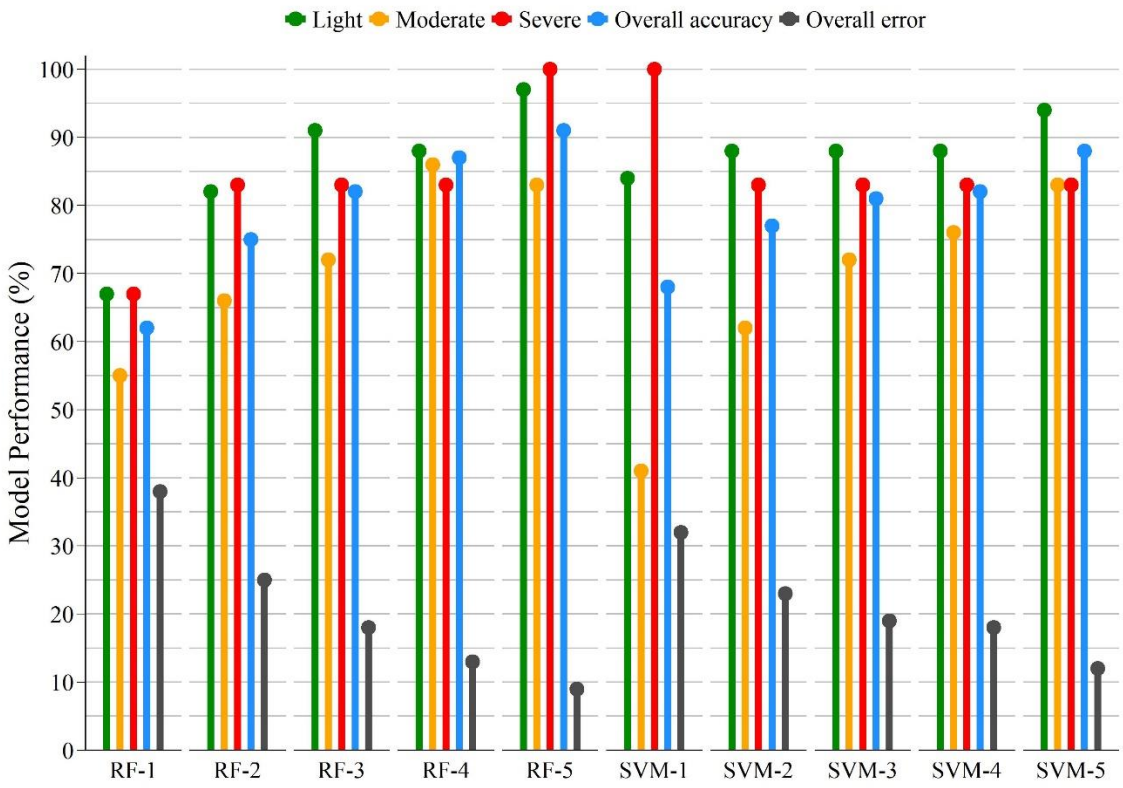

Figure 3.5: Comparison of model performance for Random Forest (RF) and Support Vector Machine (SVM) classifiers. Model Producer's accuracies for three annual SBW defoliation classes along with overall accuracies and errors are shown. Vegetation indices selected for each RF and SVM model are defined in Table 3.2.

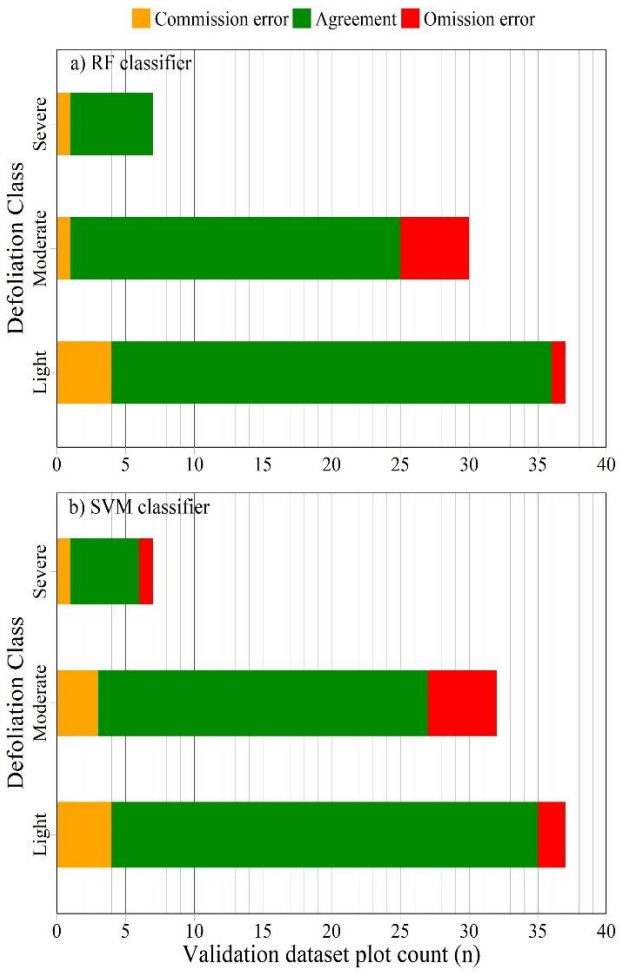

Figure 3.6: Random Forest (a) and Support Vector Machine (b) classification agreement, commission error, and omission error counts for three annual SBW defoliation classes using the 68 validation plots.

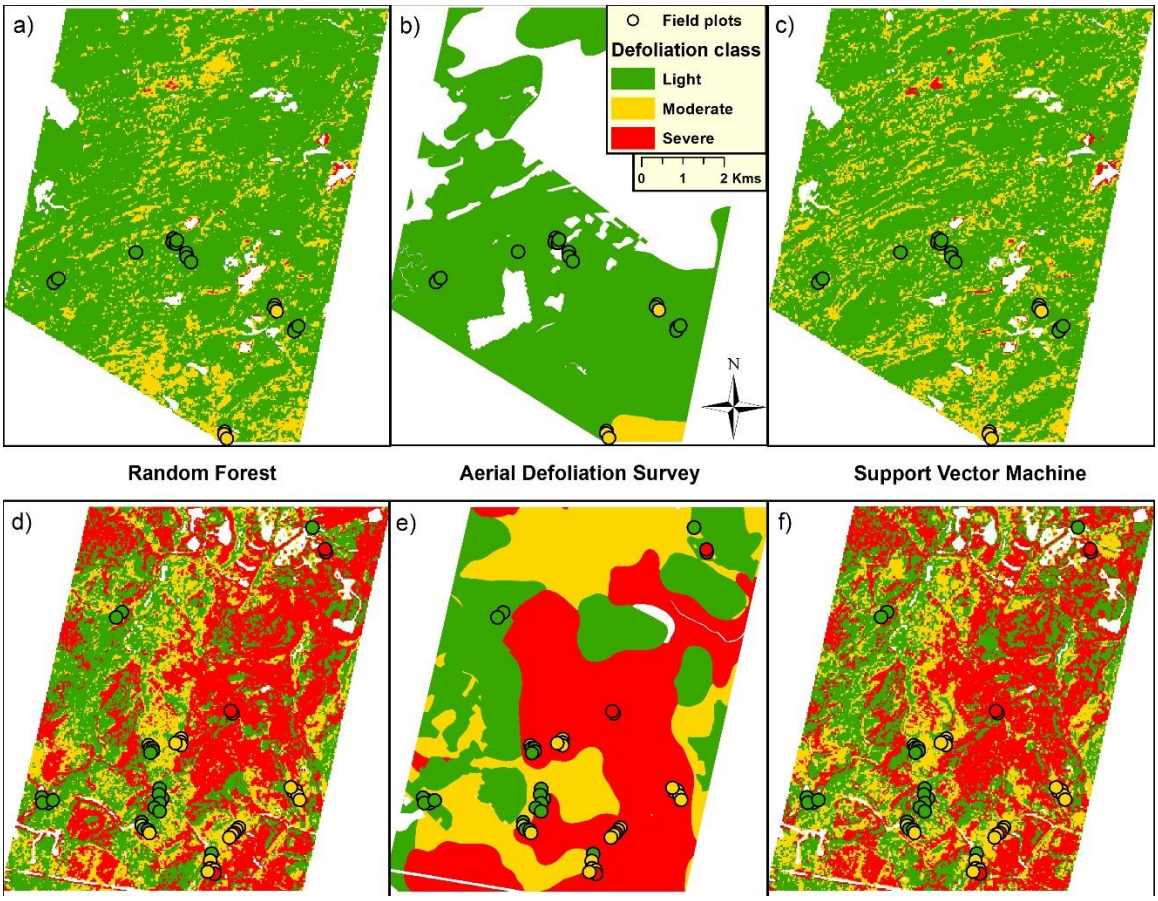

Figure 3.7: Maps comparing annual SBW defoliation from pixel-based Random Forest and Support Vector Machine classifiers and polygon-based 2016 Québec aerial survey data. Classified defoliation is mapped for two study areas near Amqui (a-c) and Causapscal (d-f), Québec. Locations of 68 field plots with measured defoliation used for classifier validation are shown as circles. White regions for RF and SVM maps represent masked/removed pixels describing roads and silviculture activity, whereas white regions for aerial survey maps were not surveyed.

CHAPTER 4: DISCUSSION AND CONCLUSIONS

4.1. Introduction

The goal of this thesis was to test two remote sensing methods for detecting annual SBW defoliation. The first method discussed in Chapter 2 examined estimating percent annual defoliation by canopy gap fraction changes collected using a digital hemispherical camera. In Chapter 3, I evaluated reflectance changes of narrow-band vegetation indices (VIs) calculated from satellite hyperspectral imagery (EO-1 Hyperion) for assisting or replacing aerial surveys in mapping forest-level defoliation.

The objectives of this chapter are to: 1) briefly summarize the main results from Chapters 2 and 3; 2) identify limitations for each remote sensing method and suggest potential improvements; and 3) discuss the management implications for improving forest health monitoring and SBW control strategic planning.

4.2. Summary of Results for Chapters 2 and 3

4.2.1. Quantification of forest canopy changes caused by spruce budworm defoliation using digital hemispherical imagery (Chapter 2)

A total of 30 explanatory variables were considered for estimating percent annual defoliation, including hemispherical image gap fraction changes, stand inventory attributes describing SBW host and non-host species basal area and density compositions, and whether sample plots had been recently sprayed with bioinsecticides. The Gradient Boosting Machine (GBM) analysis, including aerial spraying, ranked in decreasing order of relative influence spraying, gap fraction change May-October (GFC_MO), and balsam fir basal area % (BF_BA%) as the top three variables. Similarly, when spraying was

excluded GFC_MO, BF_BA%, and gap fraction October (GF_October) had the greatest relative influence. Results for GFC_MO indicated that quantifying canopy gap fraction change could be related to annual SBW defoliation through image acquisitions avoiding leaf-off periods for non-hosts trees (e.g., hardwoods).

Parametric logistic Generalized Linear Model (GLM) and non-parametric Random Forest (RF) models used to estimate defoliation included the variables spraying, GFC_MO, and BF_BA% resulted in the lowest mean bias, mean absolute bias (MAB), and root mean square error (RMSE) ranging from -0.1–1.0%, 15.1–15.5%, and 18.2–18.8%, respectively. Models excluding spraying, using the variables GFC_MO, BF_BA%, and GF_October, had less accurate results, with mean bias, MAB, and RMSE of -1.6–0.5%, 18.0–18.2%, and 21.1–22.4%. Goodness-of-fit statistics showed RF was marginal but consistently more accurate than GLM, however, either method is deemed acceptable.

When defoliation estimated using GLM and RF models were compared with ocular and branch measurements for a random 1/3 of plots held back for validation, models that included the insecticide spraying variable had higher Pearson correlations, indicating spraying can improve estimates if data is available. Additionally, both GLM and RF correlations with either ocular or branch defoliation data were higher in 2015 than in 2016, with results ranging from r = 0.68–0.91 for 2015, r = 0.41–0.72 for 2016, and r = 0.60–0.76 when combining both years. One aspect of this difference may be attributed to more lower defoliation estimates observed in 2016. Lower defoliation levels were often overestimated, and in contrast, severe defoliation estimates tended to be underestimated, but including aerial spraying as a variable helped correct these biases.

4.2.2. Potential of satellite hyperspectral imagery for detecting annual spruce budworm defoliation (Chapter 3)

In Chapter 3, the top five of 14 narrow-band change detection based VIs tested to estimate three annual defoliation classes were the Plant Senescence Reflectance Index (PSRI), Moisture Stress Index (MSI), Normalized Difference Water Index (NDWI), Modified Simple Ratio (MSR), and Enhanced Vegetation Index (EVI). Total Variable Importance Scores were 120, 75, 70, 58, and 57 and Spearman's rank correlation results between VIs and defoliation were r = -0.65, -0.53, 0.32, 0.37, and 0.43 for PSRI, MSI, NDWI, MSR, and EVI, respectively.

These top five VIs were consecutively added to RF and Support Vector Machine (SVM) classifiers and validated for classification accuracy using branch defoliation measurements from field plots. Both RF and SVM classifiers showed similar accuracy improvements for all three defoliation classes by adding VIs, and the resulting best overall accuracies were 88% for SVM and 91% for RF using all 5 VIs, versus only 38% accuracy for 2016 aerial survey data. The majority of omission and commission classification errors resulted from confusing light and moderate defoliation classes. Similar outcomes were observed using Landsat-5 imagery with the RF classifier for mapping SBW defoliation in 2008 and 2009 (Rahimzadeh-Bajgiran et al., 2018).

Comparing within-stand pixel-based RF and SVM classified defoliation with multi-stand polygon aerial survey data demonstrated that imagery-based estimates identified variation in defoliation within stands that was missed by aerial surveys. For the Amqui study area, aerial surveys identified 98% of the areas as light defoliation, but imagery based results classified 78–83% of pixels as light defoliation, and only about half (45–

51%) of the 2% of the area identified as moderate defoliation in aerial surveys was classified as moderate. For the Causapscal study area, aerial surveys delineated 31%, 27%, and 42% of the area as light, moderate, and severe in which 45–46%, 22–24%, and 48% of pixels had matching defoliation, respectively. The hyperspectral imagery-based method clearly resulted in much higher spatial resolution of defoliation estimation.

4.3. Critique and Study Limitations

4.3.1. Hemispherical image acquisitions for dealing with variable sky conditions

In Chapter 2, I demonstrated that use of hemispherical imagery was a viable method for detecting defoliation; however, challenges exist regarding collecting quality images, especially when attempting change detection analysis (Cielsa, 2000). Differing weather (wind and rain) and variable sky conditions (sunny, blue sky, and white clouds) between two imaging periods can cause gap fraction changes not related to defoliation. I collected images during hardwood leaf-off periods and minimal wind, but with variable sky conditions. Diffuse overcast sky conditions are ideal for estimating gap fraction (Frazer et al., 2001). My aim was to explore a method that was repeatable and scalable for use in future defoliation monitoring since varying sky conditions will be an inherent factor. My method involved averaging gap fraction changes for three camera exposures (-0.3, 0.0, and 0.3), batch processing images by the blue channel, which is best for separating blue sky from vegetation (Brusa and Bunker, 2014), and ensuring accurate camera placement within field plots. Of course, only sampling a few areas during overcast conditions and manually processing individual images for proper exposure would potentially improve defoliation estimates, but would also be time-consuming, so

the trade-off between accuracy and scalability is important to understand. Applying the method to stands less dominated by balsam fir-spruce may be challenging due to reduced image pixels related to SBW hosts, leading to less sensitivity between gap fraction change and defoliation.

4.3.2. Algorithms for thresholding sky and vegetation mixed pixels

Mixed pixels contain both sky and vegetation components (Macfarlane, 2011), increase with increasing vegetation, and occur mainly near the outer edges of tree crowns where current-year foliage growth and defoliation are most abundant. Numerous pixel thresholding/binarization algorithms are available for classifying mixed pixels and minimizing over- or under-correction of gap fraction estimates. All algorithms are sensitive to overexposure, so I selected the "Minimum" algorithm, which is the least affected compared to the recommended "Edge Detection" or "Minimum Histogram" algorithms (Glatthorn and Beckschäfer, 2014). By not conducting a sensitivity analysis of other algorithms in Chapter 2, we likely have not explored the full value of hemispherical imagery for detecting SBW defoliation. Chapter 2 could be a first step in developing a standardized approach using hemispherical imagery suitable for use in stand conditions (mature balsam fir-spruce dominated) most vulnerable to SBW outbreaks.

4.3.3. Satellite hyperspectral image timing in relation to defoliation

In Chapter 3, the spatial-temporal availability of satellite hyperspectral images containing low cloud cover was limited and influenced the accuracy of classifying defoliation. The challenge relates to the short 2–3 week peak defoliation detection period in combination with the orbit of the EO-1 Hyperion satellite, which follows a sun-

synchronous near-polar flight only allowing re-imaging of earth's surface every 16 days (Eigemeier et al., 2012). As a result, our change detection analysis selected images 2 and 10 days before when most defoliation occurs during the SBW sixth instar larval stage (Miller, 1977). Ideally, a conservative imaging period 2–4 weeks before peak defoliation could improve classifications. SBW outbreaks are affected by spatial-temporal environmental factors such as temperature causing host foliage growth and SBW emergence/feeding to vary, leading to spatial-temporal peak defoliation (Bouchard and Auger, 2014; Pureswaran et al., 2015). Additionally, hyperspectral images were only available 47 and 52 days after the 2–3 week detection period. These dates provided good results, but they also deserve attention in the sense that reflectance change sensitivity caused by defoliation degrades over time and other but less influential within-stand non-SBW disturbances can potentially cause further misclassifications. Therefore, maximizing reflectance changes solely caused by SBW defoliation should target image dates closer to aerial surveys when foliage damage and discoloration reaches peak spectral intensity. One option is the Harmonized Landsat Sentinel-2 (HLS) image products that offer imaging temporal resolutions of 3–5 days, which is an significant advantage over other satellite platforms (Claverie et al., 2018).

4.3.4. Hyperspectral image processing and masking non-forest pixels

Extensive processing of hyperspectral data makes it less desirable for jurisdictions to use because of the need for skilled personnel who can apply such data for informing forest management. EO-1 Hyperion imagery has inherent signal-to-noise degradation that varies across its spectral range from faulty sensor detectors requiring specific band,

geometric, and atmospheric corrections (Rasel et al., 2016). After corrections, further processing to remove non-forested/unwanted pixels by masking is common in remote sensing forests and vegetation (Alonzo et al., 2014; L. Liu et al., 2017; Tsai et al., 2007). My approach included a Normalized Difference Vegetation Index (NDVI) threshold of < 0.7 applied to all images for removing non-forested pixels; however, defoliation misclassifications were still evident adjacent to recent timber harvesting and silviculture activity. To improve defoliation classification, improved pixel masking methods are needed to identify only stands susceptible to defoliation. Pixel masking that integrates spatial forest management activity and area-based enhanced stand inventory information should be examined.

4.4. Future Research and Integration of Remote Sensing for Monitoring SBW Outbreaks

The current SBW outbreak ongoing in Québec covered a total area of 9.6 million ha in 2019 (QMFFP, 2019). For forest managers, up-to-date information, especially annual defoliation extent and severity, is essential in overall forest protection planning, identifying stands with rising SBW populations, allocating aerial spraying of bioinsecticides, and gaining more insight on tree growth response, mortality, and survival during and post-outbreak.

Using hemispherical imagery was successful in estimating canopy defoliation, but a drawback was not being able to estimate single-tree defoliation similar to ocular and branch methods. Hemispherical imagery would be adequate for monitoring annual defoliation patterns of stands or developing stand-level growth responses, but to better

understand and accurately forecast outbreak impacts, opting for single tree defoliation data for tree-list growth models makes our hemispherical image approach less applicable. Similar ground-based remote sensing technology such as terrestrial LiDAR and photogrammetry may have merit for working towards individual tree defoliation estimates. However, a common limiting factor for all of the above remote sensing technologies is the challenge of foliage occlusion by neighboring trees, branches, and foliage itself (Côté et al., 2012). Mulverhill et al. (2019) described a method of robust image collection coupled with newer camera technology such as the RICOH Theta S 360 degree handheld camera that collected terrestrial point cloud data for predicting diameter at breast height, tree taper, and volume of individual trees in boreal mixedwood forests. Terrestrial point cloud data could also potentially quantify canopy structure changes such as gap fraction caused by SBW defoliation, but again the challenge of occlusion remains.

Investigating unmanned aerial vehicles (UAVs) may be the most promising option by sensing more overall tree foliage by looking downward at individual crowns using hyperspectral, multispectral, or LiDAR sensors. UAV time-series multispectral data was able to monitor a simulated disease outbreak of single trees in (*Pinus radiata* (D. Don)) stands (Dash et al., 2017) and UAV-based photogrammetry and hyperspectral imaging was successful in mapping European bark beetle damage at the tree-level (Näsi et al., 2015). UAVs offer two options fixed- or rotary-winged aircraft designs. Fixed-winged UAVs offer longer flights but require proper takeoff and landing locations which limits their versatility. Rotary UAVs have shorter flight periods and can be challenging to control in windy conditions but can take-off and land in small clearings or on roads (Colomina and Molina, 2014). Avian safety regulations require line-of-sight between

operator and aircraft which further limits large-scale assessments across variable terrain (Hall et al., 2016). The technology continues to receive attention and could complement sampling localized areas for defoliation and validating aerial surveys or satellite imagery.

Incorporating satellite hyperspectral imagery in forest-level monitoring of SBW outbreaks could provide objective classifications at within-stand spatial scales that aerial surveys are unable to provide. Also, hyperspectral imagery has the ability to detect subtle reflectance changes caused by defoliation, which is promising for working towards more precise classifications of lower and moderate defoliation levels. Satellite remote sensing capabilities including both hyper- and multi-spectral sensors may soon consistently offer annual pixel-based defoliation monitoring. This spatio-temporal data could be integrated with area-based enhanced forestry inventories for improving forecasts of SBW impacts. This improved spatial monitoring will help forester managers better understand SBW dispersal and defoliation patterns and develop more effective SBW controls and early intervention strategies.

Current and upcoming remote sensing missions will offer more open access satellite imagery with improved temporal, spatial, and spectral capabilities that are well suited for forest health monitoring during SBW outbreaks. Although the EO-1 Hyperion satellite was decommissioned in 2017, new hyperspectral satellite missions with higher signal-to-noise ratios (signal strength) than Hyperion are operational or are preparing to be launched. The hyperspectral DESIS (DLR Earth Sensing Imaging Spectrometer) sensor which was recently installed on the International Space Station in 2018, the Italian PRIMSA (PRecursore IperSpettrale della Missione Applicativa) satellite launched in 2019, and the German EnMAP (Environment Mapping and Analysis Program) that will

be launched into orbit in 2020. The increased availability of hyperspectral images will allow continued imaging opportunities to improve detection of defoliation. Finally, the Harmonized Landsat Sentinel-2 (HLS) project is a NASA initiative that will provide moderate-resolution (10–30m pixels) multispectral multi-sensor imagery with superior temporal resolution of imaging ranges from 3–5 days (Skakun et al., 2017). This more frequent temporal resolution deserves consideration in assisting aerial surveys for monitoring the full extent of SBW outbreaks.

4.5. Conclusions

For estimating annual SBW defoliation using hemispherical photos, insecticide spraying, GFC_MO, BF_BA% were the top three variables. GLM and RF modelling estimated defoliation with similar accuracy, with RF models only marginally better. Including the insecticide spraying variable in models helped to correct some of the over- and under-estimates at light and severe defoliation levels, respectively. Hemispherical imagery is a viable, fast, and repeatable method that can assist ocular and branch defoliation methods and in permanent sample plot assessment of SBW impacts.

The top five VIs derived from change detection of reflectance from EO-1 Hyperion hyperspectral images for estimating three annual defoliation classes were PSRI, MSI, NDWI, MSR, and EVI. RF and SVM classifiers using these VIs had similar accuracy with RF marginally better. Most misclassifications resulted from confusing classes of light and moderate defoliation, which is a challenge during aerial surveys and has been found in other remote sensing studies. Hyperspectral imagery outperformed aerial surveys when compared to plot-level branch defoliation measurements, demonstrating

within-stand pixel-level classification of variation in defoliation that was not possible by aerial surveys. Hyperspectral imagery change detection results could supplement aerial survey data for detecting SBW defoliation more objectively, for use in planning spraying of bioinsecticides to minimize balsam fir-spruce forest damage.

In conclusion, results support change detection techniques rather than single image analysis and highlight the importance of model validation using accurate plot-level defoliation measurements. Within-stand defoliation mapping across forests would be an improvement over polygon-based aerial surveys, for use in both forest protection planning and impact assessment. Both hemispherical and hyperspectral imagery are objective methods that could be used in monitoring SBW outbreaks and performed as well or better than current methods of estimating defoliation.

4.6. References

Alonzo, M., Bookhagen, B., Roberts, D.A., 2014. Urban tree species mapping using hyperspectral and lidar data fusion. Remote Sens. Environ. 148, 70–83.

Bouchard, M., Auger, I., 2014. Influence of environmental factors and spatio-temporal covariates during the initial development of a spruce budworm outbreak. Landsc. Ecol. 29, 111–126.

Brusa, A., Bunker, D.E., 2014. Increasing the precision of canopy closure estimates from hemispherical photography: blue channel analysis and under-exposure. Agric. For. Meteorol. 195–196, 102–107.

Cielsa, W.M., 2000. Remote sensing in forest health protection. United States Department of Agriculture Forest Service, Forest Health Technology Enterprise Team, Salt Lake City, Utah. FHTET Report No.00–03.

Claverie, M., Ju, J., Masek, J.G., Dungan, J.L., Vermote, E.F., Roger, J-C., Skakun, S.V., Justice, C., 2018. The Harmonized Landsat and Sentinel-2 surface reflectance data set. Remote Sens. Environ. 219, 145–161.

Colomina, I., Molina, P., 2014. Unmanned aerial systems for photogrammetry and remote sensing: a review. ISPRS J. Photogramm. Remote Sens. 92, 79–97.

Côté, J.F., Fournier, R.A., Frazer, G.W., Olaf Niemann, K., 2012. A fine-scale architectural model of trees to enhance LiDAR-derived measurements of forest canopy structure. Agric. For. Meteorol. 166–167, 72–85.

Dash, J.P., Watt, M.S., Pearse, G.D., Heaphy, M., Dungey, H.S., 2017. Assessing very high resolution UAV imagery for monitoring forest health during a simulated disease outbreak. ISPRS J. Photogramm. Remote Sens. 131, 1–14.

Eigemeier, E., Heiskanen, J., Rautiainen, M., Mttus, M., Vesanto, V.-H., Majasalmi, T., Stenberg, P., 2012. Chapter 1: Narrowband vegetation indices for estimating boreal forest leaf area index. In: Escalante-Ramirez B (Ed.), Remote Sensing - Applications. Croatia. pp. 1–29.

Frazer, G.W., Fournier, R.A., Trofymow, J.A., Hall, R.J., 2001. A comparison of digital and film fisheye photography for analysis of forest canopy structure and gap light transmission. Agric. For. Meteorol. 109, 249–263.

Glatthorn, J., Beckschäfer, P., 2014. Standardizing the protocol for hemispherical photographs: accuracy assessment of binarization algorithms. PLoS One 9 (11), e111924.

Hall, R.J., Castilla, G., White, J.C., Cooke, B.J., Skakun, R.S., 2016. Remote sensing of forest pest damage: a review and lessons learned from a Canadian perspective. Can. Entomol. 148, S296–S356.

Liu, L., Coops, N.C., Aven, N.W., Pang, Y., 2017. Mapping urban tree species using integrated airborne hyperspectral and LiDAR remote sensing data. Remote Sens. Environ. 200, 170–182.

Macfarlane, C., 2011. Classification method of mixed pixels does not affect canopy metrics from digital images of forest overstorey. Agric. For. Meteorol. 151, 833–840.

Miller, C.A., 1977. The feeding impact of spruce budworm on balsam fir. Can. J. For. Res. 7, 76–84.

Mulverhill, C., Coops, N.C., Tompalski, P., Bater, C.W., Dick, A.R., 2019. The utility of terrestrial photogrammetry for assessment of tree volume and taper in boreal mixedwood forests. Ann. For. Sci. 76 (83).

Näsi, R., Honkavaara, E., Lyytikäinen-Saarenmaa, P., Blomqvist, M., Litkey, P., Hakala, T., Viljanen, N., Kantola, T., Tanhuanpää, T., Holopainen, M., 2015. Using UAV-based photogrammetry and hyperspectral imaging for mapping bark beetle damage at tree-level. Remote Sens. 7, 15467–15493.

Pureswaran, D.S., De Grandpré, L., Pare, D., Taylor, A., Barrette, M., Morin, H., Regniere, J., Kneeshaw, D.D., 2015. Climate-induced changes in host tree-insect phenology may drive ecological state-shift in boreal forests. Ecology 96 (6), 1480–1491.

Québec Ministère des Forêts de la Faune et des Parcs (QMFFP), 2019. Aires infestées par la tordeuse des bourgeons de l'épinette au Québec en 2019 - Québec Ministère des Forêts de la Faune et des Parcs, Direction de la protection des forêts, Québec. 32p.

Rahimzadeh-Bajgiran, P., Weiskittel, A., Kneeshaw, D., MacLean, D., 2018. Detection of annual spruce budworm defoliation and severity classification using Landsat imagery. Forests 9 (357).

Rasel, S.M.M., Chang, H-C., Diti, I.J., Ralph, T., Saintilan, N., 2016. Comparison of very near infrared (VNIR) wavelength from EO-1 Hyperion and WorldView 2 images for saltmarsh classification. In: ISPRS Annals of Photogrammetry, Remote Sensing and Spatial Information Sciences, Prague, Czech Republic. pp. 85–92.

Skakun, S., Vermote, E., Roger, J-C., Franch, B., 2017. Combined use of Landsat-8 and Sentinel-2A images for winter crop mapping and winter wheat yield assessment at regional scale. AIMS Geosci. 3 (2), 163–186.

Tsai, F., Lin, E.K., Yoshino, K., 2007. Spectrally segmented principal component analysis of hyperspectral imagery for mapping invasive plant species. Int. J. Remote Sens. 28 (5), 1023–1039.

Curriculum Vitae

Candidate's full name: Shawn David Donovan

Universities attended:
University of New Brunswick (2012–2015), Bachelor of Science Forestry
University of New Brunswick (2015–2020), Master of Science in Forestry

Articles published in or submitted to refereed journals:
Donovan, S.D., MacLean, D.A., Kershaw, J.A., Lavigne, M.B. 2018. Quantification of forest canopy changes caused by spruce budworm defoliation using digital hemispherical imagery. Agric. For. Meteorol. 262, 89–99.
Donovan, S.D., MacLean, D.A., Zhang, Y., Lavigne, M.B, Kershaw, J.A. Potential of satellite hyperspectral imagery for detecting annual spruce budworm defoliation. Submitted February 6, 2020 to Remote Sensing of Environment.

Non-refereed contributions:
Donovan, S.D., MacLean, D.A., Zhang, Y., Lavigne, M.B., Kershaw, J.A. 2016. Quantifying annual spruce budworm defoliation using hemispherical imagery and EO-1 Hyperion hyperspectral satellite data (Q15). Assessment of Wood Attributes from Remote sEnsing (AWARE) 1st AGM, Corner Brook, NL, Canada, May 2016.
Donovan, S.D., MacLean, D.A. 2017. Quantification of spruce budworm defoliation using hemispherical imagery and EO-1 Hyperion hyperspectral satellite data. SERG International Workshop, Fredericton, NB, Canada, Feb. 2017.
Donovan, S.D., MacLean, D.A., Zhang, Y., Lavigne, M.B., Kershaw, J.A. 2017. Quantification of spruce budworm defoliation using hemispherical imagery and EO-1 Hyperion hyperspectral satellite data (Q15). Assessment of Wood Attributes from Remote sEnsing (AWARE) 2nd AGM, Edmundston, NB, Canada, May 2017.
Donovan, S.D., MacLean, D.A., Kershaw, J.A., Lavigne, M.B. 2018. Quantification of forest canopy changes caused by spruce budworm defoliation using digital hemispherical imagery. Northeastern Forest Pest Council (NEFPC) 80th AGM, Burlington, VT, USA, Mar. 2018.
Donovan, S.D., MacLean, D.A., Zhang, Y., Lavigne, M.B., Kershaw, J.A. 2018. Quantification of spruce budworm defoliation using hemispherical imagery and EO-1 Hyperion hyperspectral satellite data (Q15). Assessment of Wood Attributes from Remote sEnsing (AWARE) 3rd AGM, Point Claire, QC, Canada, Jun. 2018.
Donovan, S.D., MacLean, D.A., Kershaw, J.A., Lavigne, M.B. 2018. Quantification of forest canopy changes caused by spruce budworm defoliation using digital hemispherical imagery. The 9th Bi-Annual Eastern Canada - USA Forest Science Conference, Fredericton, NB, Canada, Oct. 2018.
Donovan, S.D., MacLean, D.A., Zhang, Y., Lavigne, M.B., Kershaw, J.A. 2020. Potential of satellite hyperspectral imagery for detecting annual spruce budworm defoliation (Q15). Assessment of Wood Attributes from Remote sEnsing (AWARE) 4th AGM, Toronto, ON, Canada, Feb 2020.